3. Aerosols and Radiation

3.1. Aerosol Monitoring

A. McComiskey (Editor), E. Andrews, D. Jackson,
A. Jefferson, S.W. Kim, J. Ogren,
P. Sheridan, and J. Wendell

3.1.1. Scientific Background

Aerosol particles affect the radiative balance of the Earth both directly, by scattering and absorbing solar and terrestrial radiation, and indirectly, through their action as cloud condensation nuclei (CCN) with subsequent effects on the microphysical and optical properties of clouds. Evaluation of the climate forcing by aerosols, defined here as the perturbation of the Earth's radiation budget induced by the presence of airborne particles, requires knowledge of the spatial distribution of the particles, their optical and cloud-nucleating properties, and suitable models of radiative transfer and cloud physics. Obtaining a predictive relationship between the aerosol forcing and the physical and chemical sources of the particles requires knowledge of regional and global-scale chemical processes, physical transformation, and transport models for calculating the spatial distributions of the major chemical species that control the optical and cloud-nucleating properties of the particles. Developing and validating these various models calls for a diverse suite of in situ and remote observations of the aerosol particles over a wide range of spatial and temporal scales.

Aerosol measurements began at the CMDL baseline observatories in the mid-1970s as part of its predecessor, the Geophysical Monitoring for Climatic Change (GMCC) program. The objective of these baseline measurements was to detect a response, or lack of response, in atmospheric aerosols to changing conditions on a global scale. Since the inception of the program, scientific understanding of the behavior of atmospheric aerosols has improved considerably. It is now understood that residence times of tropospheric aerosols are generally less than 1 week and that human activities primarily influence aerosols on regional/continental scales rather than on global scales. In response to this increased understanding, and to more recent findings that anthropogenic aerosols create a significant perturbation in the Earth's radiative balance on regional scales [*Charlson et al.,* 1992; *NRC*, 1996], CMDL expanded its aerosol research program to include regional aerosol monitoring stations. The goals of this regional-scale monitoring program are: (1) to characterize means, variabilities, and trends in climate-forcing properties of different types of aerosols, and (2) to understand the factors that control these properties.

No single approach to observing the atmospheric aerosol can provide the necessary data for monitoring all the relevant dimensions and spatial/temporal scales required to evaluate climate forcing by anthropogenic aerosols. In situ observations from fixed surface sites, ships, balloons, and aircraft provide very detailed characterizations of the atmospheric aerosol on limited spatial scales. Remote sensing methods from satellites, aircraft, or the surface can determine a limited set of aerosol properties on local to global spatial scales, but they cannot provide the chemical information needed for linkage with global chemical models. Fixed ground stations are suitable for continuous observations over extended time periods but lack vertical resolution. Aircraft and balloons provide the vertical dimension, but measurements are not continuous. Only when systematically combined do these various types of observations produce a data set where point measurements are extrapolated by models into large geographical scales that enable their results to be compared to satellite measurements and where process studies have a context for drawing general conclusions from experiments conducted under specific conditions.

Measurements of atmospheric aerosols are used in three fundamentally different ways for aerosol/climate research: algorithm development for models and remote-sensing retrievals, parameter characterization, and model validation. Laboratory and field studies guide the development of parameterization schemes, and the choice of parameter values for chemical transport models that describe the relationship between emissions and the concentration fields of aerosol species. Systematic surveys and monitoring programs provide characteristic values of the aerosol properties used in radiative transfer models for calculating the radiative effects of the aerosols and for retrieving aerosol properties from satellites and other remote sensing platforms. Finally, monitoring programs provide spatial and temporal distributions of aerosol properties that are compared to model results to validate the models. Each of these three modes of interaction between applications and measurements requires different types of data and entails different measurement strategies. *Ogren* [1995] applied the thermodynamic concept of “intensive” and “extensive” properties of a system to emphasize the relationship between measurement approach and applications of aerosol observations.

Intensive properties do not depend on the amount of aerosol present and are used as parameters in chemical transport and radiative transfer models (e.g., atmospheric residence time, single-scattering albedo). Extensive properties vary strongly in response to mixing and removal processes and are most commonly used for model validation (e.g., mass concentration, optical depth). Intensive properties are more difficult and expensive to measure than extensive properties because they generally are defined as the ratio of two extensive properties. As a result, different measurement strategies are needed for meeting the data needs of the various applications. Measurements of a few carefully chosen extensive properties, of which aerosol optical depth and species mass concentrations are prime candidates, are needed in many locations to test the ability of the models to predict spatial and temporal variations on regional-to-global scales and to detect changes in aerosol concentrations resulting from changes in aerosol sources. The higher cost of determining intensive properties suggests a strategy of using a limited number of highly instrumented sites to characterize the means and variabilities of intensive properties for different regions or aerosol types that are supplemented with surveys by aircraft and ships to characterize the spatial variability of these parameters. CMDL's regional aerosol monitoring program is primarily focused on characterizing intensive properties.

CMDL measurements provide ground truth for satellite observations and global models as well as key aerosol parameters for global-scale models (e.g., scattering efficiency of sulfate particles and hemispheric backscattering fraction). An important aspect of this strategy is that the chemical measurements are linked to the physical measurements through simultaneous, size-selective sampling that allows the observed aerosol properties to be connected to the atmospheric cycles of specific chemical species [e.g., *Quinn et al.*, 2002].

3.1.2. EXPERIMENTAL METHODS

Extensive aerosol properties monitored by CMDL include condensation nucleus (CN) concentration, aerosol optical depth (δ), and components of the aerosol extinction coefficient at one or more wavelengths (total scattering (σ_{sp}), backward hemispheric scattering (σ_{bsp}), and absorption (σ_{ap})). At the regional sites, size-resolved impactor and filter samples (submicrometer and supermicrometer size fractions) are obtained for gravimetric and chemical (ion chromatograph) analyses. All size-selective sampling, as well as the measurements of the components of the aerosol extinction coefficient at the regional stations, is performed at a low, controlled relative humidity (<40%) to eliminate the confounding effects that are due to changes in ambient relative humidity. Data from the continuous sensors are screened to eliminate contamination from local pollution sources. At the regional stations, the screening algorithms use measured wind speed, direction, and total particle number concentration in real-time to prevent contamination of the chemical samples. Algorithms for the baseline stations use measured wind speed and direction to exclude data that are likely to have been locally contaminated.

Prior to 1995 data from the baseline stations were manually edited to remove spikes from local contamination. Since 1995 an automatic editing algorithm is applied to the baseline data in addition to the manual editing of local contamination spikes. For the baseline stations (Barrow, Alaska (BRW), Mauna Loa, Hawaii (MLO), American Samoa (SMO), and the South Pole, Antarctica (SPO)), as well as the Sable Island, Canada (WSA) regional station, data are automatically removed when the wind direction is from local sources of pollution (such as generators and buildings) as well as when the wind speed is less than a threshold value (0.5-1 m s^{-1}). Also at MLO, data for upslope conditions (1800-1000 UTC) are excluded since the air masses do not represent "background" free tropospheric air. A summary of the data-editing criteria for each station is presented in Table 3.1.

Integrating nephelometers are used to determine the light scattering coefficient of the aerosol. These instruments illumine a fixed sample volume from the side and observe the amount of light scattered by particles and gas molecules in the direction of a photomultiplier tube. The instrument integrates over scattering angles of 7°-170°. Depending on the station, measurements are performed at three or four wavelengths in the visible and near-infrared. Newer instruments allow determination of the hemispheric backscattering coefficient by use of a shutter to prevent illumination of the portion of the instrument that yields scattering angles less than 90°. A particle filter is inserted periodically into the sample stream to measure the light scattered by gas molecules and is subtracted from the total scattered signal to determine the contribution from the particles alone. The instruments are calibrated by filling the sample volume with CO_2 gas, which has a known scattering coefficient.

Table 3.1. Data-Editing Summary for NOAA Baseline and Regional Stations

Station	Editing	Clean Sector
Barrow	a,b,c	0° < WD < 130°
Mauna Loa	a,b,c,d	90° < WD < 270°
Samoa	a,b,c	0° < WD < 165°, 285°<WD < 360°
South Pole	a,b,c	0° < WD < 110°, 330°<WD < 360°
Sable Island	a,b,c	0° < WD < 35°, 85° < WD < 360°
Bondville	a	
Southern Great Plains	a	
Trinidad Head	b,c	56^o < WD < 186^o

a: Manual removal of local contamination spikes
b: Automatic removal of data not in clean sector
c: Automatic removal of data for low wind speeds
d: Removal of data for upslope wind conditions
WD: Wind direction

The aerosol light absorption coefficient is determined by a continuous light absorption photometer. This instrument continuously measures the amount of light transmitted through a quartz filter while particles are deposited on the filter. The rate of decrease of transmissivity, divided by the sample flow rate, is directly proportional to the light absorption coefficient of the particles. Newer instruments (Particle Soot Absorption Photometers (PSAP), Radiance Research, Seattle, Washington) are calibrated in terms of the difference of light extinction and scattering in a long-path extinction cell for laboratory test aerosols. Older instruments at the baseline stations (aethalometers, Magee Scientific, Berkeley, California) were calibrated by the manufacturer in terms of the equivalent amount of black carbon from which the light absorption coefficient is calculated, assuming a mass absorption efficiency of the calibration aerosols of 10 m^2 g^{-1}.

Particle number concentration is determined with a CN counter that exposes the particles to a high supersaturation of butanol vapor. This causes the particles to grow to a size where they can be optically detected and counted. The instruments in use have lower particle-size detection limits of 10-20 nm diameter.

Summaries of the extensive measurements obtained at each site are given in Tables 3.2 and 3.3. Table 3.4 lists the intensive aerosol properties determined from the directly measured extensive properties. These properties are used in chemical transport models to determine the radiative effects of the aerosol concentrations calculated by the models. Inversely, these properties are used in algorithms for interpreting satellite remote-sensing data in order to determine aerosol amounts based on the measurements of the radiative effects of the aerosol.

3.1.3. ANNUAL CYCLES

The annual cycles of aerosol optical properties for the four baseline and four regional stations are illustrated in Figures 3.1 and 3.2, respectively. The data are presented in the form of box and whisker plots that summarize the distribution of values. Each box ranges from the lower to upper quartiles with a central bar at

Table 3.2. CMDL Baseline Aerosol Monitoring Stations (Status as of December 2003)

Category	Baseline Arctic	Baseline Free Troposphere	Baseline Marine	Baseline Antarctic
Location	Point Barrow	Mauna Loa	American Samoa	South Pole
Designator	BRW	MLO	SMO	SPO
Latitude	71.323ºN	19.539ºN	14.232ºS	89.997ºS
Longitude	156.609ºW	155.578ºW	170.563ºW	102.0ºE
Elevation (m)	8	3397	77	2838
Responsible Institute	CMDL	CMDL	CMDL	CMDL
Status	Operational, 1976 major upgrade, 1997	Operational, 1974 major upgrade, 2000	Operational, 1977	Operational, 1974 major upgrade, 2002
Sample RH	RH <40%	RH <40%	Uncontrolled	Uncontrolled
Sample Size Fractions	D<1 µm D<10 µm	D<1 µm D<10 µm	Uncontrolled	Uncontrolled
Optical measurements	$\sigma sp(3\lambda)$, $\sigma bsp(3\lambda)$, $\sigma ap(1\lambda)$	$\sigma sp(3\lambda)$, $\sigma bsp(3\lambda)$, $\sigma ap(1\lambda)$, $\delta(6\lambda)$	None	$\sigma sp(4\lambda)$
Microphysical measurements	CN concentration	CN concentration	CN concentration	CN concentration
Chemical measurements	Major ions, mass	None	None	None

Table 3.3. CMDL Regional Aerosol Monitoring Sites (Status as of December 2003)

Category	Perturbed Marine	Perturbed Continental	Perturbed Continental	Continental Marine
Location	Sable Island, Nova Scotia, Canada	Bondville, Illinois	Lamont, Oklahoma	Trinidad Head, California
Designator	WSA	BND	SGP	THD
Latitude	43.933ºN	40.053ºN	36.605ºN	41.054ºN
Longitude	60.007ºW	88.372ºW	97.489ºW	124.151ºW
Elevation (m)	5	230	315	107
Responsible institute	CMDL	CMDL	CMDL	CMDL
Collaborating institute(s)	AES Canada, NOAA/ PMEL	University of Illinois, Illinois State Water Survey	DOE/ARM	Humbolt State University, PMEL, NOAA Aeronomy
Status	Operational, August 1992 Inactive, April 2000	Operational, July 1994	Operational, July 1996 Chemistry, February 2000	Operational, April 2002
Sample RH	RH <40%	RH <40%	RH <40% 40% < RH < 85% scan	RH <40% 40% < RH < 85% scan
Sample size fractions	D<1 µm, D<10 µm	D<1 µm, D<10 µm	D<1 µm, D<10 µm	D<1 µm, D<10 µm
Optical measurements	$\sigma sp(3\lambda)$, $\sigma bsp(3\lambda)$ $\sigma ap(1\lambda)$	$\sigma sp(3\lambda)$, $\sigma bsp(3\lambda)$, $\sigma ap(1\lambda)$	$\sigma sp(3\lambda)$,$\sigma bsp(3\lambda)$, $\sigma ap(1\lambda)$, $\delta(7\lambda)$	$\sigma sp(3\lambda)$,$\sigma bsp(3\lambda)$, $\sigma ap(1\lambda)$
Microphysical measurements	CN concentration	CN concentration	CN, n(D) concentration	CN
Chemical measurements	Major ions, mass	Major ions, mass	Major ions, mass	Major ions, mass

AES, Atmospheric Environment Service; PMEL, Pacific Marine Environment Laboratory, DOE/ARM, Department of Energy/Atmospheric Radiation Measurement.

Table 3.4. Intensive Aerosol Properties Derived From CMDL Network

Properties	Description
å	The Ångström exponent, defined by the power-law $\sigma sp \propto \lambda^{-\mathring{a}}$, describes the wavelength-dependence of scattered light. In the figures below, *å* is calculated from measurements at 550 and 700 nm wavelengths. Situations where the scattering is dominated by submicrometer particles typically have values around 2, while values close to 0 occur when the scattering is dominated by particles larger than a few microns in diameter.
ω_o	The aerosol single-scattering albedo, defined as $\sigma sp/(\sigma ap + \sigma sp)$, describes the relative contributions of scattering and absorption to the total light extinction. Purely scattering aerosols (e.g., sulfuric acid) have values of 1, while very strong absorbers (e.g., elemental carbon) have values around 0.3.
g, *b*	Radiative transfer models commonly require one of two integral properties of the angular distribution of scattered light (phase function): the asymmetry factor *g* or the hemispheric backscatter fraction *b*. The asymmetry factor is the cosine-weighted average of the phase function, ranging from a value of -1 for entirely backscattered light to +1 for entirely forward-scattered light. The hemispheric backscatter fraction *b* is defined as $\sigma bsp/\sigma sp$.
f(RH)	The hygroscopic growth factor, defined as $\sigma sp(RH=85)/\sigma sp(RH=40)$, describes the humidity dependence of scattering on relative humidity (RH).
α_i	The mass scattering efficiency for species *i*, defined as the slope of the linear regression line relating σ_{sp} and the mass concentration of the chemical species, is used in chemical transport models to evaluate the radiative effects of each chemical species predicted by the model. This parameter has typical units of $m^2\ g^{-1}$.

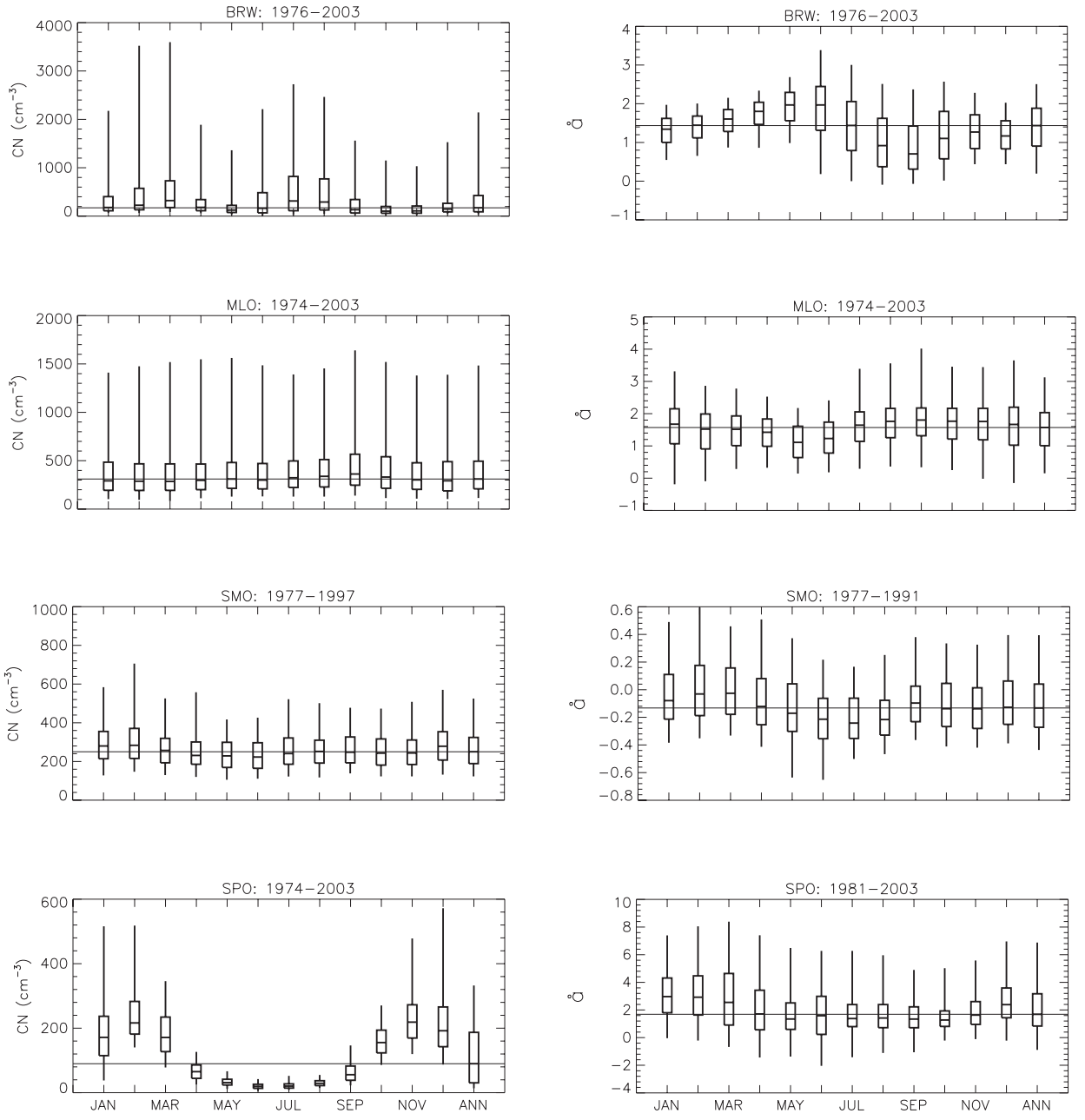

Figure 3.1. Annual cycles for baseline stations at BRW, MLO, SMO, and SPO showing statistics for condensation nuclei (CN) concentration, total scattering coefficient (σ_{sp}), Ångström exponent (å), absorption coefficient (σ_{ap}) and single scattering albedo (ω_0). Statistics representing the entire period are given in the last column (ANN), with the horizontal line representing the median value.

the median value, while the whiskers extend to the 5th and 95th percentiles. The statistics are based on the hourly averages of each parameter for each month of the year; also shown are the annual statistics for the entire period of record. The horizontal line represents the annual median, therefore, measurements above and below the median can easily be discerned. The annual cycles for the baseline stations are based on data through the end of 2003 except at SMO where scattering measurements were made from 1977 to 1991, and CN measurements were made from 1977 to 1997. In general, changes in long-range transport patterns dominate the annual cycles of the baseline stations.

Figure 3.1 shows that, for BRW, the high values of CN, σ_{sp}, and σ_{ap} are observed during the Arctic haze period when anti-cyclonic activity transports pollution from the lower latitudes of Central Europe and Russia. A more stable polar front characterizes the summertime meteorology. High cloud coverage and precipitation scavenging of accumulation mode (0.1-1.0-μm diameter) aerosols account for the annual minima in σ_{sp} and σ_{ap}

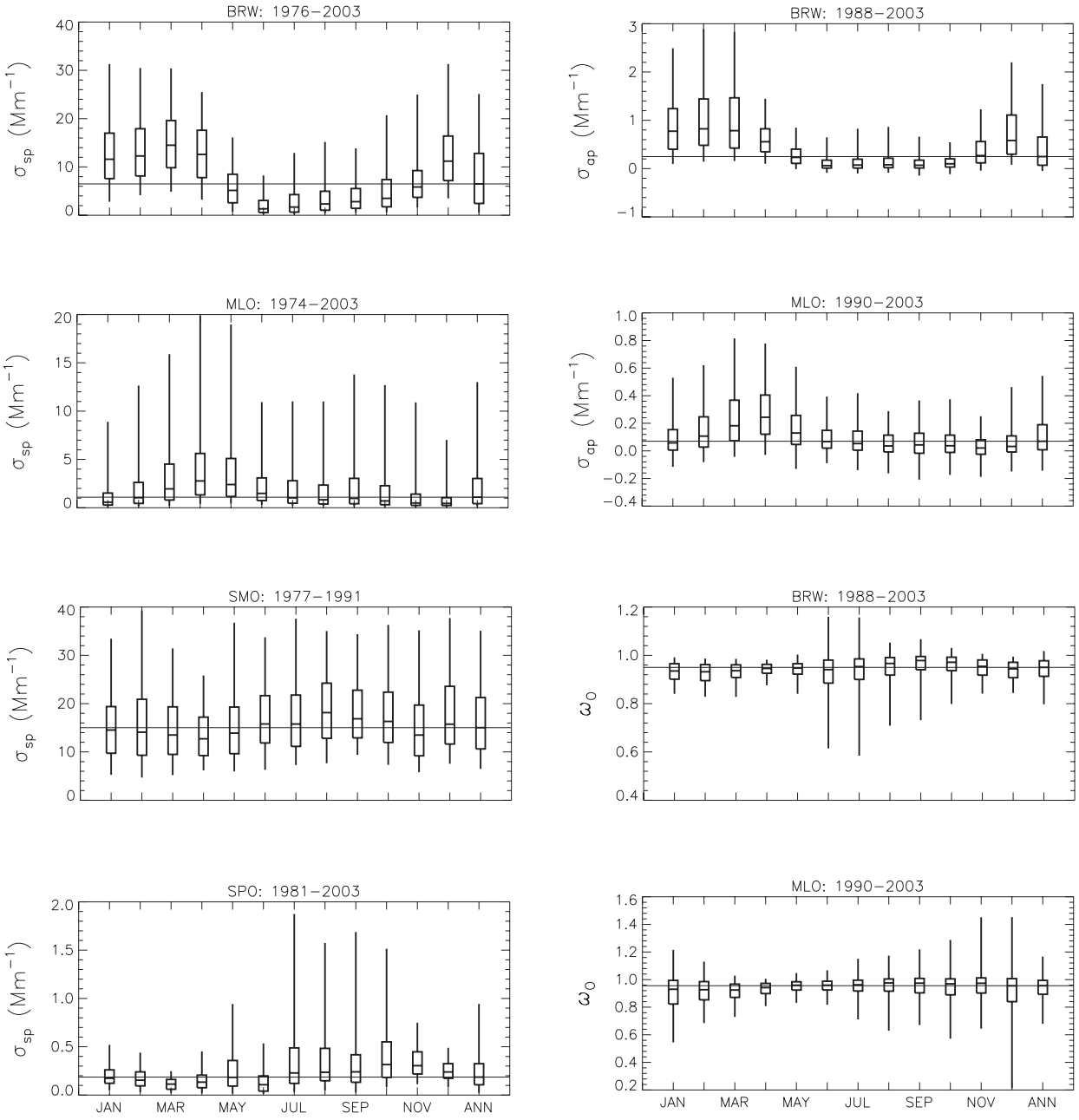

Figure 3.1. (continued) Annual cycles for baseline stations at BRW, MLO, SMO, and SPO showing statistics for condensation nuclei (CN) concentration, total scattering coefficient (σ_{sp}), Ångström exponent (å), absorption coefficient (σ_{ap}) and single scattering albedo (ω_0). Statistics representing the entire period are given in the last column (ANN), with the horizontal line representing the median value.

from June to September. In contrast, CN values have a secondary maximum in the summer that is thought to be the result of sulfate aerosol production from gas-to-particle conversion of dimethyl sulfide (DMS) oxidation products by local oceanic emissions [*Radke et al*., 1990]. The aerosol single-scattering albedo displays little annual variability and is indicative of highly scattering sulfate and sea salt aerosol. A September minimum is observed in å when σ_{sp} and accumulation mode aerosols are also low, but when primary production of coarse mode sea salt aerosols from open water is high [*Quinn et al.*, 2002; *Delene and Ogren*, 2002]. The work of *Quinn et al.* [2002] has also shown, based on their chemical analysis of the sub-micrometer aerosol particles at BRW, that sea salt has a dominant role in controlling scattering in the winter, non-sea salt sulfate is the dominant scatterer in the spring, and both components contribute to scattering in the summer.

For MLO the highest σ_{sp} and σ_{ap} values occur in the springtime and result from the long-range transport of pollution

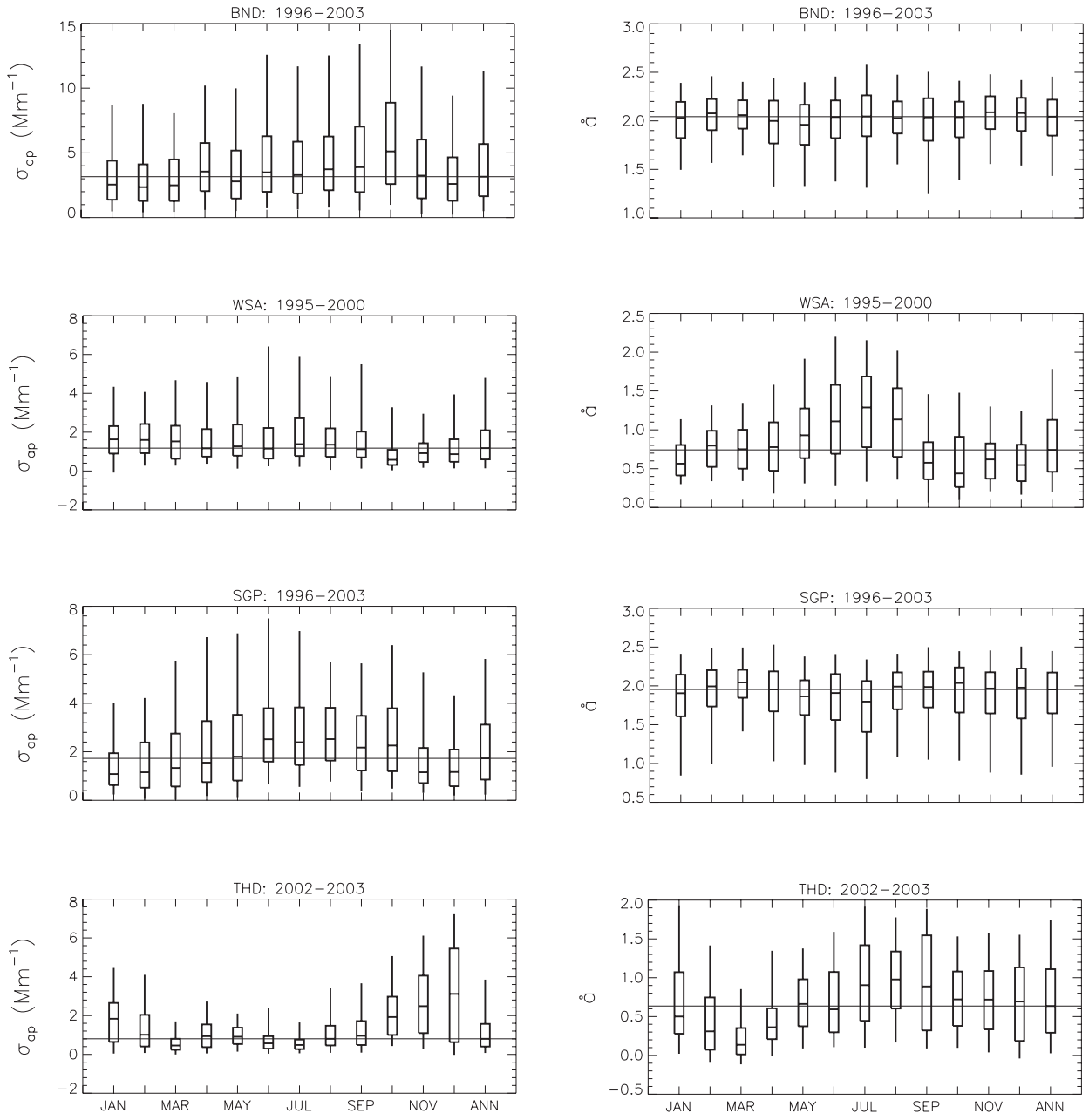

Figure 3.2. Annual cycles for regional stations at BND, WSA, and SGP showing statistics the annual absorption coefficient (σ_{ap}), total scattering coefficient (σ_{sp}), Ångström exponent (å), and single-scattering albedo (ω_0). Statistics representing the entire period are given in the last column (ANN), with the horizontal line representing the median value.

and mineral dust from Asia. However, little seasonality is seen in CN concentrations at MLO, indicating that the smallest particles (<0.1-μm diameter), which usually dominate CN concentration, are not enriched during these long-range transport events. Both the aerosol σ_{sp} and Ångström exponent display seasonal cycles at SPO with a σ_{sp} maximum and an å minimum in austral winter associated with the transport of coarse mode sea salt from the Antarctic coast to the interior of the continent. The summertime peaks in CN and å are associated with fine mode sulfate aerosol and correlate with a seasonal sulfate peak found in the ice core, presumably from coastal biogenic sources [*Bergin et al*., 1998]. The aerosol extensive properties at SMO display no distinct seasonal variation. Albedo values above 1.0 that are evident at BRW and MLO are due to instrument noise at low aerosol concentration. These high albedo values are not present in daily averaged data. Furthermore, the high albedo values are not present if data are excluded where σ_{sp} is below 1 Mm^{-1}. Hence, the high albedo values are a result of a detection limitation in the instrument.

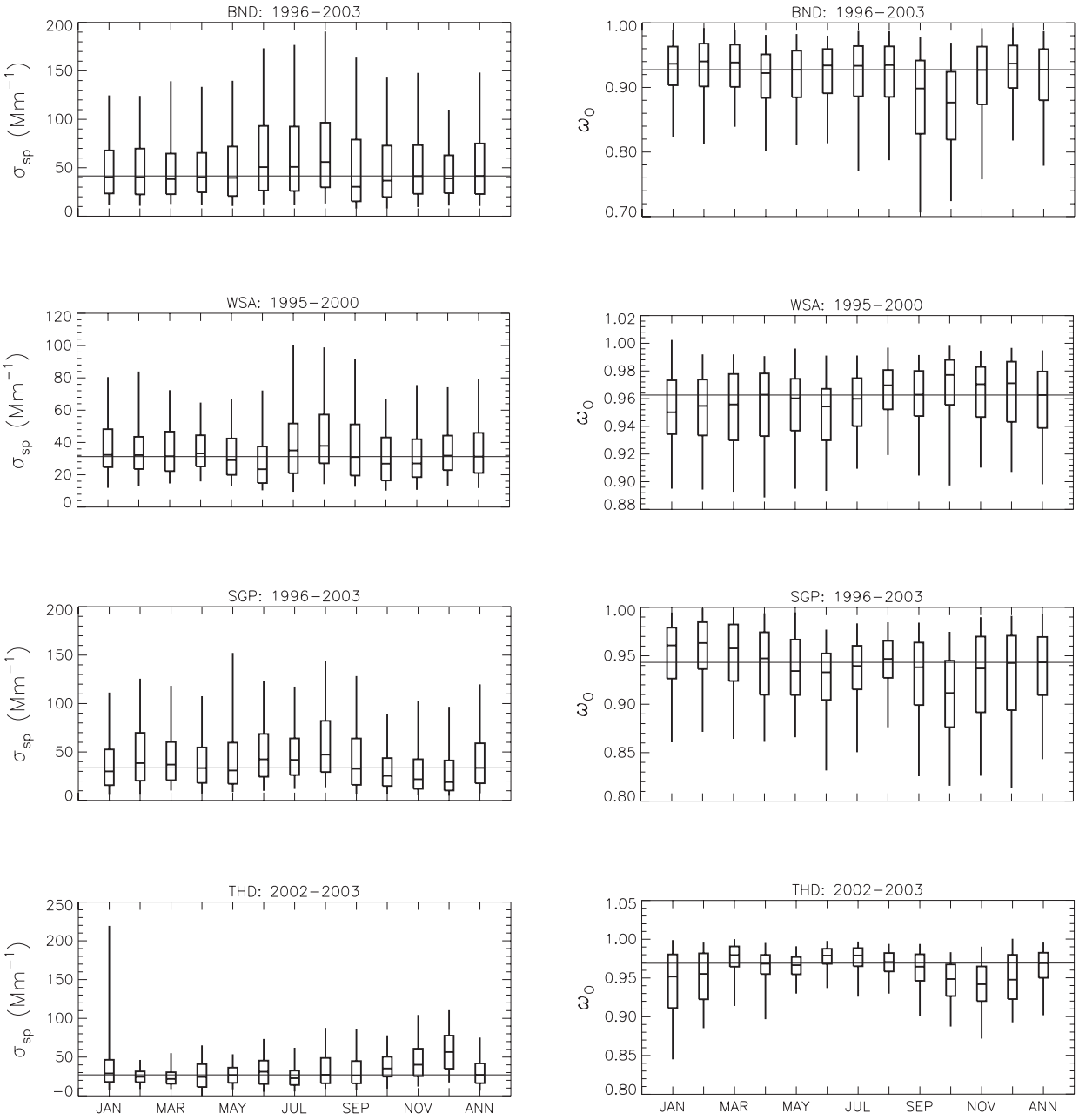

Figure 3.2. (continued) Annual cycles for regional stations at BND, WSA, and SGP showing statistics the annual absorption coefficient (σ_{ap}), total scattering coefficient (σ_{sp}), Ångström exponent (å), and single-scattering albedo (ω_0). Statistics representing the entire period are given in the last column (ANN), with the horizontal line representing the median value.

Based on only 4-7 years of measurements, the annual cycles for the regional stations are less certain than those of the baseline stations. The proximity of the regional sites to North American pollution sources is apparent in the results with monthly median values of σ_{sp} that are up to two orders of magnitude higher than the values from the baseline stations. The Bondville, Illinois, site (BND), situated in a rural agricultural region, displays an autumn high in σ_{ap} and a low in ω_0 that coincides with anthropogenic and dust aerosols emitted during the harvest [*Delene and Ogren*, 2002]. As evident in the lower σ_{sp} and σ_{ap} values, the Southern Great Plains, Lamont, Oklahoma site (SGP) is more remote than BND. SGP has a similar, but less pronounced annual cycle with late summer highs in σ_{sp} and σ_{ap}, and a corresponding minimum in ω_0 [*Delene and Ogren*, 2001; *Sheridan et al.*, 2001]. Little seasonal variability is observed in aerosol properties at WSA. Values of å tend to be higher in the summer and most likely result

from the transport of fine mode sulfate aerosol from the continent and the lower coarse-mode production of particles associated with lower summer wind speeds [*Delene and Ogren*, 2002].

3.1.4. LONG-TERM TRENDS

Figure 3.3 shows long-term trends in CN concentration and σ_{sp} for the baseline observatories, and Figure 3.4 shows long-term trends in å for the baseline observatories and σ_{ap} and ω_0 for BRW and MLO. The monthly means are plotted along with a linear trend line fitted to the data. Since 1980 the aerosol properties at BRW have exhibited an annual decrease in σ_{sp} of about 2% yr^{-1}. This reduction in aerosol scattering was attributed to decreased anthropogenic emissions from Europe and Russia [*Bodhaine*, 1989] and is most apparent during March when the Arctic haze effect is largest. The corresponding decrease in the Ångström exponent over the same time period points to a shift in the aerosol size distribution to a larger fraction of coarse mode sea salt aerosol. *Stone* [1997] noted a long-term increase in both surface temperatures and cloud coverage at BRW from 1965-1995 that derives from the changing circulation patterns and may account for the reduction in σ_{sp} by enhanced scavenging of accumulation mode aerosols.

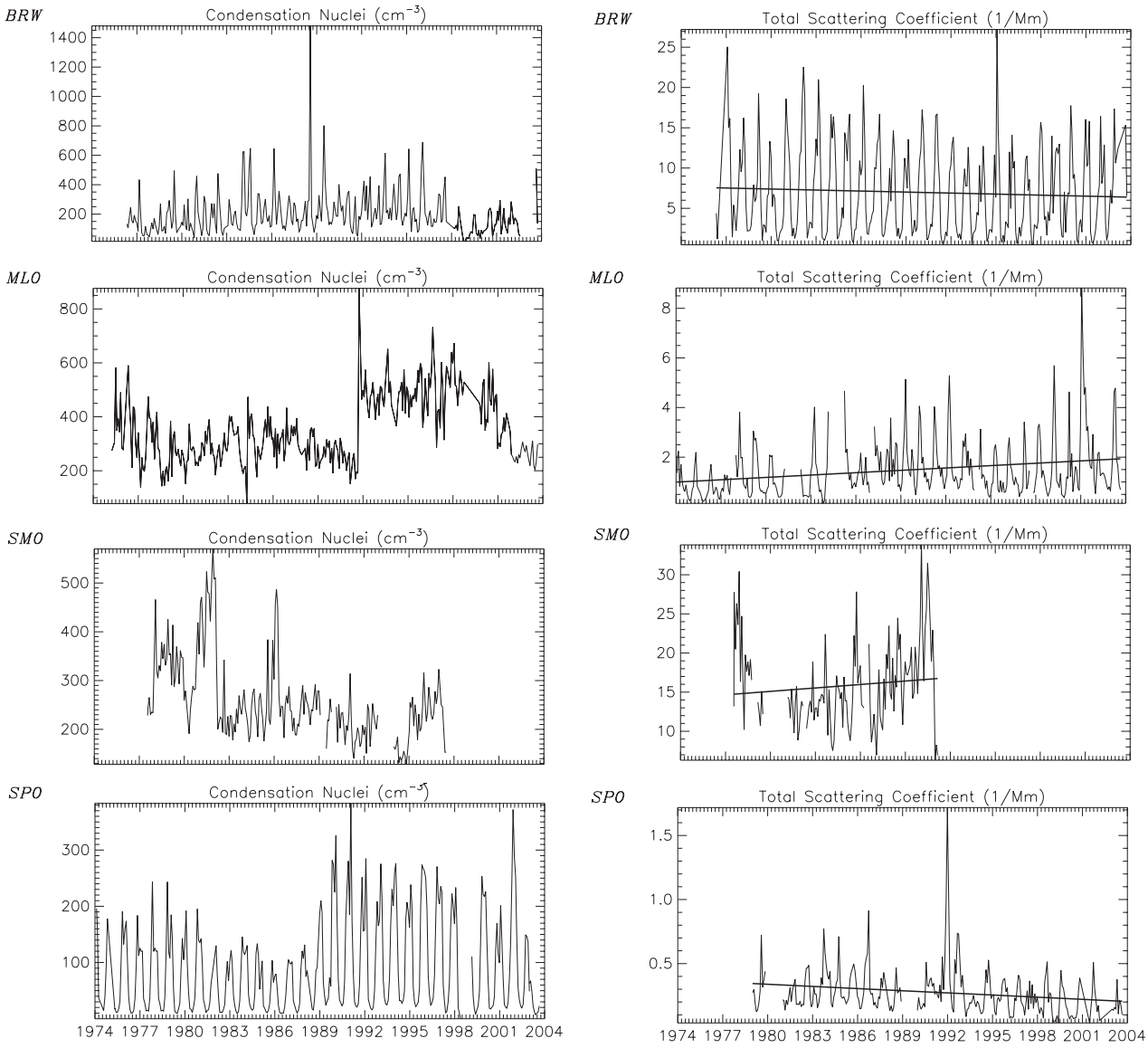

Figure 3.3. Long-term trends for the baseline stations showing the monthly averaged condensation nuclei concentration and total scattering coefficient at 550 nm. A simple linear fit is given for the scattering coefficient but is omitted for the condensation nuclei since instrument changes make a trend line inappropriate.

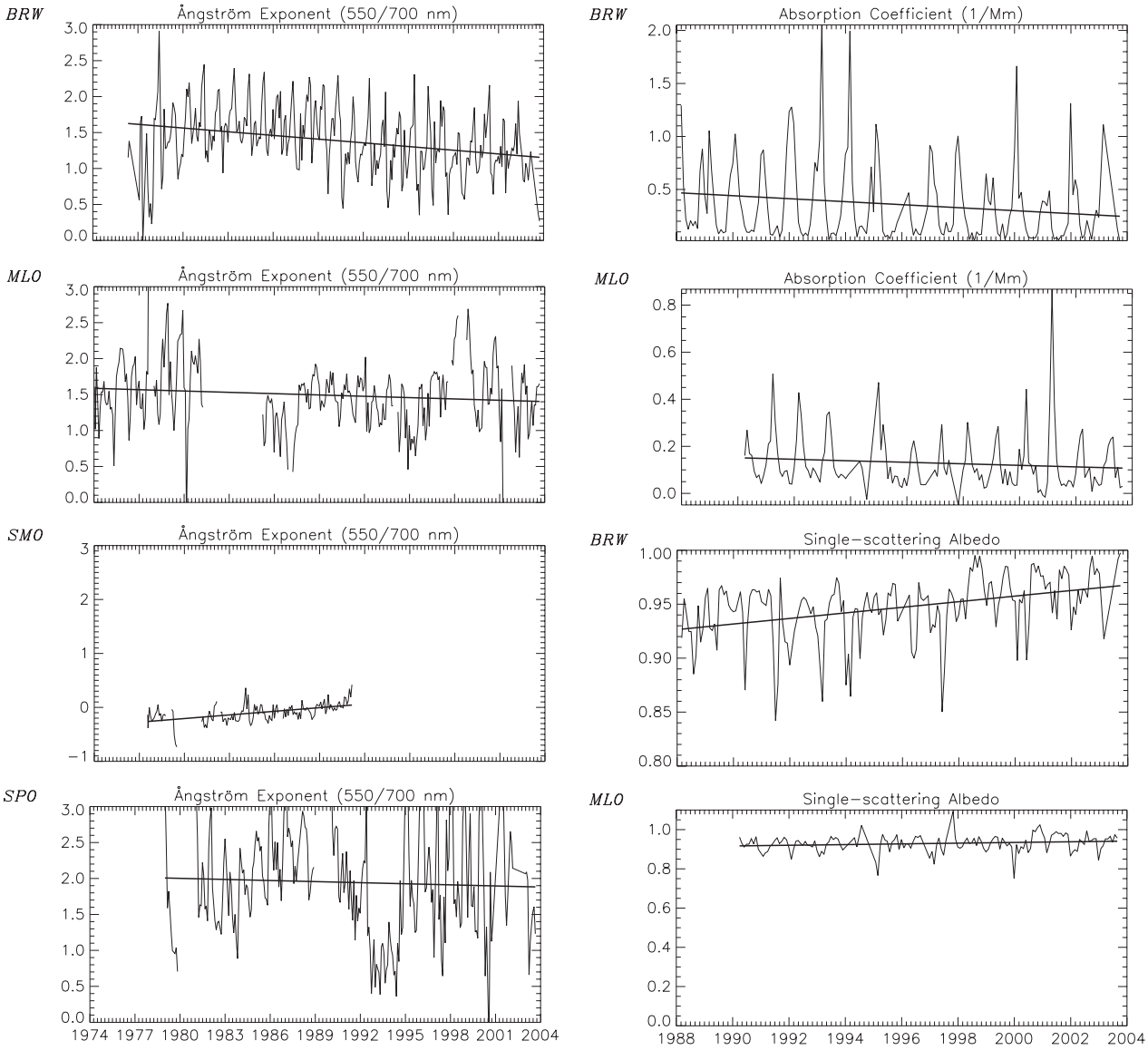

Figure 3.4. Long-term trends for the baseline stations showing the monthly averaged Angström exponent (550/700 nm), absorption coefficient, and single scattering albedo. A simple linear fit to the data is shown.

In contrast to the reduction in σ_{sp} at BRW, CN concentrations, which are most sensitive to particles with diameters <0.1 μm, have increased since 1976. There is an offset in CN concentration starting in 1998 that corresponds to a change involving a new CN sampling inlet. Similarly, the step increases in CN concentration in late 1991 at MLO and 1989 at SPO are due to the replacement of the CN counter by a butanol-based instrument with a lower size detection limit. The reason for the decrease in CN and increase in å at SMO is not readily apparent, but it could stem from changes in long-term circulation patterns.

Previous reports describing the aerosol data sets include: BRW: *Bodhaine* [1989, 1995]; *Quakenbush and Bodhaine* [1986]; *Bodhaine and Dutton* [1993]; *Barrie* [1996]; *Delene and Ogren* [2002]; MLO: *Bodhaine* [1995]; *Delene and Ogren* [2002]; SGP: *Delene and Ogren* [2002]; *Sheridan et al*. [2001]; *Bergin et al.* [2000]; SMO: *Bodhaine and DeLuisi* [1985]; SPO: *Bodhaine et al.* [1986, 1987, 1992]; *Bergin et al*. [1998]; WSA: *McInnes et al.* [1998]; *Delene and Ogren* [2002].

3.1.5. Special Studies

In Situ Aerosol Profiles Over the Southern Great Plains CART Site

Aerosol optical properties are measured over the SGP Cloud and Radiation Testbed (CART) site using a light aircraft (Cessna C-172N). The aircraft has been flying level legs at altitudes between 500 m and 3500 m several times per week since March 2000 to obtain a statistically representative data set of in situ

aerosol vertical profiles. Instrumentation on the aircraft is similar to the instrumentation at the surface SGP site so that measurements at the surface and aloft can be easily compared. Measured parameters include total light scattering, backscattering, and absorption. Calculated parameters include single-scattering albedo, backscatter fraction, and Ångström exponent.

In June 2003 the final version of a controlled humidity system was installed on the airplane. This system consists of a humidity conditioner and a second nephelometer (Radiance Research, model 903) downstream of the existing nephelometer (TSI, Incorporated, model 3563). The humidity conditioner exposes the aerosol exiting the low humidity TSI nephelometer to a relative humidity of ~80%. The second nephelometer measures the total light scattering of this humidified aerosol at a wavelength of 535 nm. This measurement provides guidance for correcting the measured dry scattering profile to ambient relative humidity conditions. Prior to the installation of this new humidity system, the surface aerosol response to relative humidity was used to make this correction. Using the surface aerosol f(RH) required the assumption that the aerosol at the surface and aloft respond identically to changes in relative humidity.

Between March 2000 and November 2003, 401 flights were flown with 370 of those flights complete for all nine profile flight levels. Consistent with the first year of measurements [*King et al*., 2001], statistical plots (Figure 3.5) show that while extensive properties decrease with altitude, the median value of the intensive properties is fairly invariant with altitude.

In addition to examining the variability for a long-term time series, the data are studied on different temporal scales (e.g., hourly and seasonally) to determine whether observed cyclic patterns occurring at the surface [*Sheridan et al*., 2001; *Delene and Ogren*, 2002] also occur aloft. Profiling flights are made during daylight hours and most flights occur in the vicinity of 800, 1200, and 1600 hours. If the median values of the lowest level leg are compared with the median values for the surface over the following categories: morning (700-1100), midday (1100-1400), and afternoon (1400-1800), similar patterns emerge. Typically higher scattering (~2x) is observed in the morning both aloft (150 m above the surface and at the surface) than in the midmorning or afternoon. This is consistent with dilution occurring as the mixing layer rises throughout the day [*Della Monache et al.,* 2004].

Figure 3.6 shows seasonal variations with height for σ_{ext} and ω_0. On a seasonal time scale the median value for σ_{ext} is highest in the summer, lower in the spring and fall, and lowest in the winter. The observed differences are due to both seasonal changes in atmospheric properties (e.g., mixing height, transport paths) as well as changes in sources. The higher σ_{ext} in the summer is consistent with lidar measurements of aerosol optical depth that

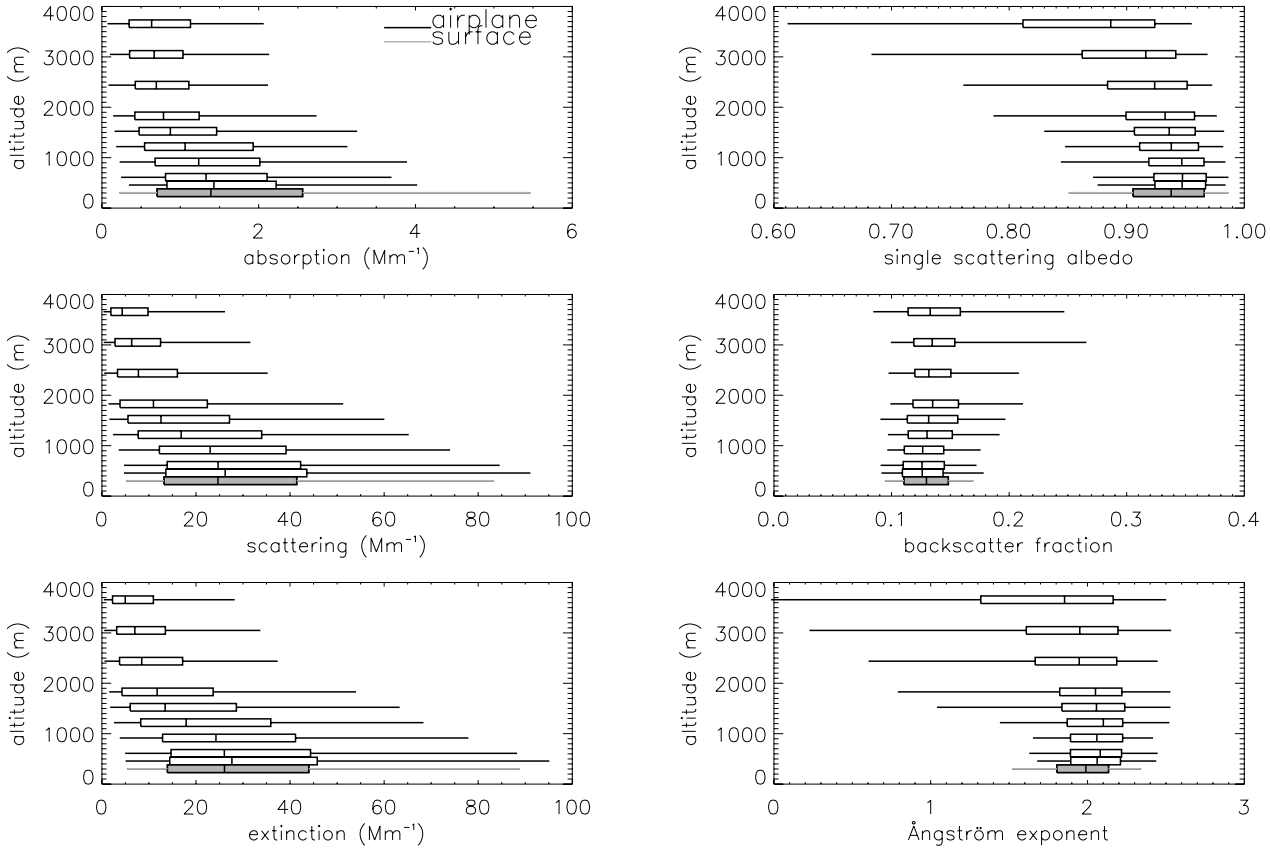

Figure 3.5. Box-whisker plots of flight profile data for whole period of study (March 2000-November 2003).

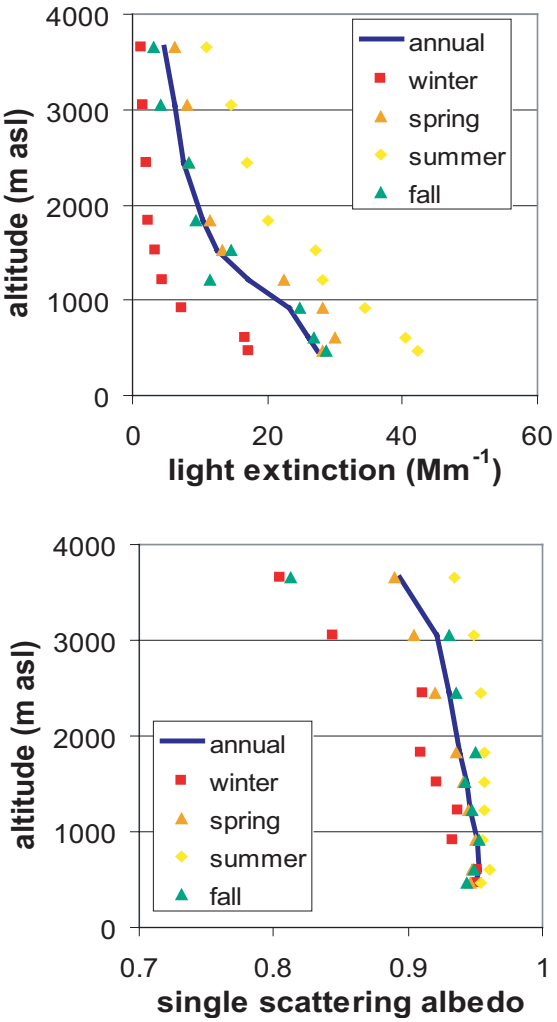

Figure 3.6. Seasonal medians of aerosol light extinction and single scattering albedo.

show the highest extinction at SGP is observed during the summer [*Ferrare et al.*, 2000]. The two components of σ_{sp} and σ_{ap} also follow this trend. Seasonal differences are also observed in the vertical profiles of ω_0. Winter tends to have significantly lower ω_0 than the other seasons, particularly aloft. Whether this is due to increased emissions of absorbing material (e.g., emissions related to heating or fireplace use) or to preferential scavenging of soluble scattering particles is a current topic of study.

Aerosol Optical Properties from Gosan, South Korea

The CMDL aerosol and radiation groups conducted in situ measurements of aerosol optical properties and column measurements of solar radiation for 10 months in 2001-2002 from Gosan, South Korea. The measurements were part of a larger intensive field campaign known as ACE-Asia (Aerosol Characterization Experiment). The goal of this campaign was to characterize the aerosol from East Asia with the intent to better estimate aerosol radiative forcing from this region.

East Asia is a region with high aerosol emissions from diverse sources that include biomass/biofuel burning, fossil fuel combustion, dust and sea salt. The Gosan site, situated on Jeju Island, is located in the East China Sea about 100 km south of the Korean Peninsula. The site receives air masses from the neighboring regions of China, Japan, the Korean Peninsula, the Pacific Ocean, and the Sea of Japan. Because an air mass may pass over several of these source regions before arriving at the island, the measured aerosol properties usually represent an aerosol of mixed composition.

The meteorology from this region, as well as the air mass source regions calculated from 5-day back trajectories, exhibit a strong seasonal dependence. Figures 3.7 and 3.8 show this seasonal variation. During the winter months and the early spring, a strong continental outflow dominates the region. This outflow, from frontal systems moving across China and high-pressure systems on the continent, is accompanied by dry air masses with high wind speeds. During the summer a high pressure system in the Pacific brings marine air to the site as well as low wind speeds, low pressure, and high relative humidity conditions. Precipitation is highest during the summer months. Fall and spring are transition periods with mixed source regions and variable weather conditions.

In order to identify the variance of aerosol optical properties with air mass, the properties were categorized by source region based on isentropic 5-day back trajectory calculations arriving at the site at an elevation of 500 m above the surface. Because the source regions exhibit a strong seasonal variation, the aerosol optical properties depend not only on the source emissions, but also on the meteorology that affects the aerosol aging process, transport time, and deposition rate.

Table 3.5 shows the highest aerosol loadings observed from the surface extinction coefficient and from the column aerosol optical depth (AOD) were from continental outflow from China and the Korean Peninsula. In addition to the high emissions from these regions, the higher-than-average wind speeds and the relatively low-cloud coverage during transport from these regions enhanced aerosol loading from sea spray and reduced loss from cloud scavenging and wet deposition. The lower aerosol loading from marine, Japan, and Sea of Japan (SOJ) sectors results from low emissions combined with high cloud coverage and high rainfall.

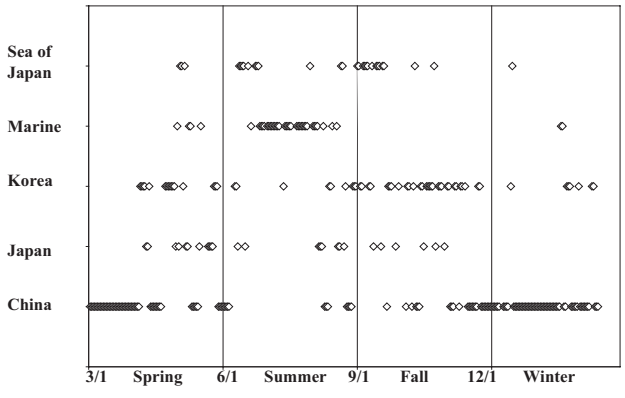

Figure 3.7. Seasonal dependence of air mass source regions arriving at Gosan, South Korea, for 2001.

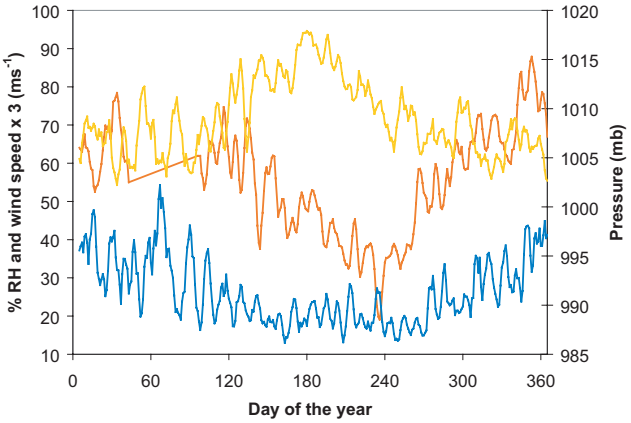

Figure 3.8. Time series of ambient surface pressure (orange), wind speed ×3 (blue) and percent relative humidity (yellow) for Gosan, South Korea, in 2001.

Aerosol size measured at Gosan was large compared to other polluted regions of the world with Ångström exponents from all the source regions below 2.0. The low Ångström exponent reflects the ubiquitous presence of sea salt aerosol even during times of low wind speed. Despite these low values, variance between the regions in aerosol size is apparent. The marine sector with the highest fraction of sea salt also had the lowest Ångström exponent of 1.17. Next lowest were the air masses from China that had high dust loading, particularly in the spring, and high sea salt associated with high wind-speed conditions. The smallest aerosols or highest Ångstrom exponent was observed from both local air masses and Japan. Delineation of the aerosol differences between these two air masses is difficult since the Japan air masses also passed over Jeju Island and most likely include local pollution.

The aerosol single scattering albedo, ω_0, exhibited little variance between the regions. The values, all below 0.9, are lower than those measured from polluted continental sites in the United States. On average, 82% of the aerosol absorption occurred in the aerosol submicron fraction. The relatively high submicron aerosol absorption that contributes to the low ω_0 is likely from soot associated with fossil fuel combustion as well as biomass burning. Biomass and biofuel burning are common both in Korea and China. Soot aerosol is also less susceptible to wet deposition or cloud scavenging and, therefore, can be transported longer distances than other more water-soluble aerosols. This may explain the low single-scattering albedo values even during clean marine air masses. These air masses with soot aerosol, from either Taiwan or Southern China, are not apparent in the 5-day back trajectories but are present in longer back trajectories and may have contributed to the low marine ω_0 values. Surprisingly, even with much local burning, the single scattering albedo from the local island air was relatively high at 0.89.

Unlike the surface in situ measurements, the aerosol column properties of AOD and surface forcing efficiency (SFE) represent the full column of aerosol and are biased toward clear sky conditions that favor measurements during seasons with high-pressure conditions and low cloud coverage. The percent of days during which radiometer measurements were collected is listed in Table 3.5. Figure 3.9 shows the variance of the column Ångström exponent measured with the sunphotometer at 412 and 862 nm wavelength channels with AOD for the different source regions. The measurements from marine, Japan, and SOJ sectors showed little dependence of the Ångström exponent with AOD. However, the air masses from China and the Korean Peninsula show a decrease in the Ångström parameter with increasing AOD. Days with high column aerosol loading from continental outflow coincided with large particles, most likely dust and/or sea salt aerosol. A similar, but weaker, decline of the Ångström parameter with extinction was observed for the surface data. During April 2001 a micropulse lidar located at Gosan observed several instances of elevated dust layers that may explain the stronger covariance of the AOD and Ångström exponent for the column than in the surface data.

The SFE was calculated from the 500-nm AOD and the downwelling broadband radiation at a zenith angle of 60°. The data were corrected for the Sun-to-Earth distance and given an assumed surface albedo of 0.06, which is consistent with an ocean surface. Figure 3.10 shows a plot of the downwelling broadband solar radiation versus AOD for the entire 10-month observation period. The slope of this data is the SFE. Deviations from this line arise from variations in the aerosol intensive properties such as the single-scattering

Table 3.5. Aerosol Properties Measured at Gosan, South Korea From April 2001 to February 2002

Region	Extinction	Albedo	Ångström Surface	f(RH)	AOD	Ångström Column	SFE	Number of Days	Percent of Days
Korea	100.8	0.88	1.45	1.89	0.25	1.14	-67.8	61	59
China	112.6	0.89	1.26	2.10	0.24	0.97	-80.0	111	38
Japan	69.7	0.89	1.55	2.32	0.23	1.16	-74.0	25	24
Marine	44.9	0.88	1.17	2.49	0.17	1.01	-50.7	40	42
SOJ	69.5	0.86	1.38	2.03	0.22	1.09	-65.9	29	31
Local	73.1	0.89	1.57	2.40	0.28	0.85	-103.9	20	30
Total	87.5	0.88	1.37	2.10	0.24	1.05	-73.9	310	41

Extinction at 550 nm in units of Mm^{-1}. Ångström at the surface is for the 450 and 700 nm wavelength pair.
Ångstrom for the column measurements is for the 412 and 862 nm wavelength pair. AOD is for 500 nm.
SFE is the surface forcing efficiency calculated from the downwelling broadband radiation from 0.285 to 4.0 µm and the 500 nm AOD.
Percent of days is the percent of column radiation data compared to the total number of days the instrument was operational.

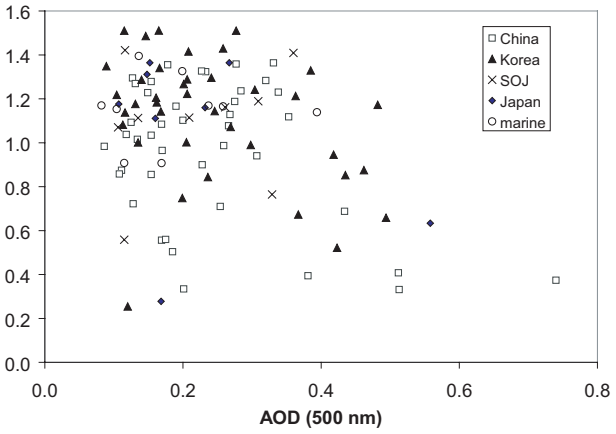

Figure 3.9. Column Ångstrom exponent (412/862 nm) versus AOD (500 nm) for various source regions at Gosan.

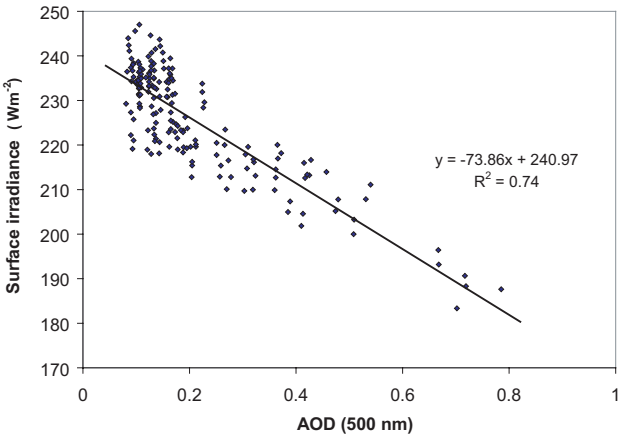

Figure 3.10. The surface forcing efficiency from April 2001 to February 2002 for Gosan, South Korea.

albedo and upscatter fraction as well as the column water vapor. Similar plots were done for data from each source region and the resulting SFE given in Table 3.5. The standard error of the slopes for these plots varied from 4.1 for China to 14.31 for the sector including Japan. The variance in the SFE between source regions is large, ranging from –50.7 to –103.9 W m^{-2}, with the strongest forcing efficiencies from aerosols in air masses from China, Japan, and local sectors. The SFE was also found to have a strong seasonal dependence with the lowest magnitude in summer of –56.8 W m^{-2} and the highest magnitude in fall of –99.7 W m^{-2}. The relationship between the SFE and aerosol size and single scattering albedo is unclear in the present data and needs further study.

Trinidad Head Regional Monitoring Station: The First 20 Months

Over the past 10 years an increasing body of research has pointed to the global nature of atmospheric aerosol. Long-range transport of natural and anthropogenic pollutants impact both remote and continentally influenced locations. In April 2002, a new observatory was established at Trinidad Head, California (THD) (41.054°N, 124.151°W, 107 m), to study the properties of atmospheric constituents entering the United States by way of the Pacific Ocean prior to influence by North American sources. The start of aerosol measurements at THD coincided with a month-long field program for the Intercontinental Transport and Chemical Transformations (ITCT) program aimed at understanding how relatively short-lived species, such as aerosol particles, are transported and detected far from their source and how these species change during transport.

Although Trinidad Head is a fairly remote coastal site (~320 km north of the San Francisco Bay area and ~320 km miles south of Eugene, Oregon), it is not as remote as the CMDL baseline stations. THD is, however, further from anthropogenic sources than any of the other CMDL regional stations. A comparison of the aerosol optical properties from the first 20 months of measurements at THD with the long-term aerosol records at other stations (Figure 3.11) shows the aerosol at THD has properties that lie somewhere between clean remote sites and regional sites. The aerosol at THD has properties most similar to those measured at WSA, also a remote coastal site. Both WSA and THD are dominated by a strong marine aerosol signal indicated by low Ångström exponents and high single-scattering albedo.

The first 18 months of measurements at THD show the influence of a variety of nonmarine aerosol sources. During the ITCT program in April and May 2002, several incursions of Asian dust were observed at the site. In August 2002 smoke from the forest fires in southern Oregon was detected at THD. Also, air mass back trajectories show occasional transport to the site from urban Northern California. The dust events (22, 24, and 26 April) both increased scattering up to a factor of 2.5 over typical background levels (~29 Mm^{-1}) and decreased absorption by a factor of 2.5 over the typical background level of ~1 Mm^{-1}. The intense smoke events at the site resulted in both scattering and absorption values on an order of magnitude higher than the background values.

Sea salt is the dominant regional aerosol present at THD, but aerosol single scattering albedo measurements indicate the presence of other types of aerosol. Sea salt-dominated aerosol tends to have a single scattering albedo of ~0.97, while lower albedos of ~0.92 are observed during smoke events that influence the site. Another indicator of the presence of nonmarine aerosol is a change in aerosol hygroscopicity (indicated by f(RH)). Marine aerosol is relatively hygroscopic while dust and smoke aerosols are likely to be more hygrophobic. Figure 3.12 shows a 2-day time period during which aerosol transitioned from predominantly a marine aerosol to a smoke aerosol and then back to a clean marine aerosol. Both the scattering and the absorption increased during the smoke episode, while single scattering albedo and f(RH) decreased.

While the THD regional station is ideally located for investigating a variety of aerosol types, the surface-based measurements have also demonstrated the importance of measuring the vertical profiles of aerosol properties. For example, during one dust event the dust resided in a layer aloft detected by column optical-depth measurements made at the site

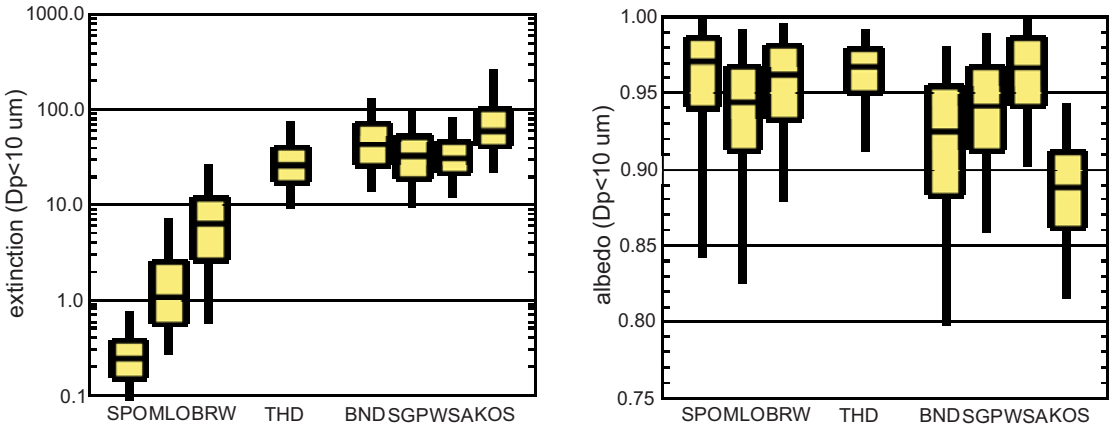

Figure 3.11. Comparison of extinction and single scattering albedo at CMDL baseline and regional stations.

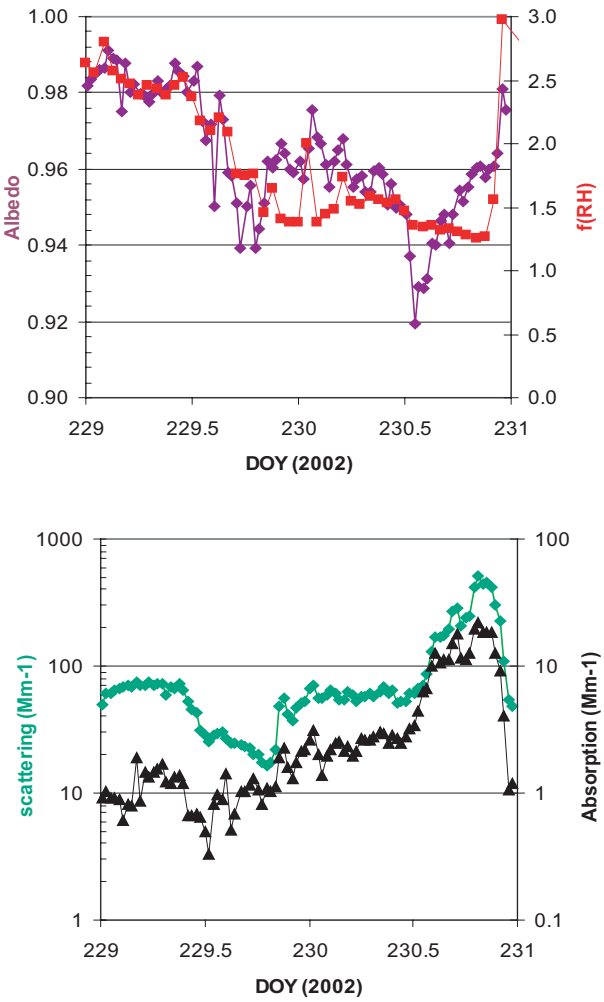

Figure 3.12. The transition from clean marine aerosol on DOY 229 to transition aerosol at DOY 229.5 to smoke-dominated aerosol between DOYs 229.75 to 230.9 and finally the return to marine aerosol at DOY 230.9. (DOY 229 = 17 August 2003).

but not by the in situ aerosol monitoring instruments at the surface. During a different dust event both in situ and column measurements indicated the presence of dust. Both events were consistent with the predictions from an aerosol forecasting model (Navy Aerosol Analysis and Prediction System). Long-term aerosol measurements at THD, in conjunction with radiation and chemistry measurements, will contribute to understanding the role of inter- and intra-continental transport of aerosol particles in climate forcing and air quality.

The 2002 Reno Aerosol Optics Study

The Reno Aerosol Optics Study (RAOS) was conducted at the Desert Research Institute in Reno, Nevada, 3-28 June 2002. The primary focus of RAOS was to evaluate the accuracy and precision of current methods for measuring the light absorption coefficient (σ_{ap}) of atmospheric aerosols by characterizing, under controlled conditions, both existing and new instruments designed to measure in situ aerosol light extinction, absorption, and scattering. Included in this experiment were three cavity ring-down extinction instruments, one classic folded-path optical extinction cell (OEC), three integrating nephelometers, two photoacoustic absorption instruments, and five filter-based absorption instruments. The operating wavelengths of the various instruments provided good coverage of the visible spectrum with limited measurements made in the near ultraviolet (UV) and near infrared (IR).

A stirred mixing chamber (~76-L volume) delivered varying amounts of white aerosols, black aerosols, ambient aerosols, and filtered air to all the instruments. The white aerosols were submicrometer ammonium sulfate, while several submicrometer black aerosols, including kerosene soot and diesel emission particles, were generated. Individual tests were run with aerosol extinction levels varying between a low value of ~50 Mm^{-1} and a high value of ~500 Mm^{-1}. Aerosol single-scattering albedos (ω_0) ranged from ~0.3 (pure black aerosol) to ~1.0 (pure ammonium sulfate). Generated aerosols were measured under low relative humidity conditions (typically <25%) and were predominantly external mixtures of the black and white particles.

Prior to any instrument intercomparison tests, aerosol generation, characterization, and delivery issues were

investigated and optimized. Tests were run on ammonium sulfate aerosols using multiple TSI 3010 condensation particle counters (CPC) and TSI 3563 integrating nephelometers to ensure that the same aerosol was transferred to each instrument. Differences in the aerosol numbers between all instruments were small, typically <1% and never above 2%. Scattering coefficients measured at the inlets of the different instruments were typically within 2% of one another. Several other methods, including scanning mobility particle sizer, tapered element oscillating microscale, and aerosol filters (for elemental and organic carbon, and electron microscopy analyses) were used throughout the duration of the RAOS to continuously characterize and monitor the type and amount of aerosols in the system.

Aerosols were generated with widely varying extinction levels and covered a large range of ω_0 in the midvisible range. The first priority was to provide mixtures of $(NH_4)_2SO_4$ and kerosene soot over all targeted ranges of extinction and ω_0. The next priority was to generate mixtures with different black aerosols (e.g., either graphite particles or diesel soot), and measure their optical properties to see how they differed from the kerosene soot tests.

For nonabsorbing aerosols, scattering should equal extinction. As a first instrument test, we compared the scattering measurement from a TSI Model 3563 integrating nephelometer to the extinction measurement from the folded-path OEC for pure $(NH_4)_2SO_4$ aerosols. Figure 3.13 shows this comparison for the green wavelength. Results from these two instruments show that independent extinction and scattering measurements at 530 nm on white aerosols agree to better than 1%. Our two primary methods for the measurement of aerosol light absorption were photoacoustic spectroscopy and the difference between light extinction and scattering. A comparison of these two methods for mixed $(NH_4)_2SO_4$ and kerosene soot aerosols is shown in Figure 3.14. The two independent standards for σ_{ap} were found to agree well within 10% over a wide absorption range at a wavelength of 530 nm. These standards provide the basis to derive calibration curves for filter-based instruments.

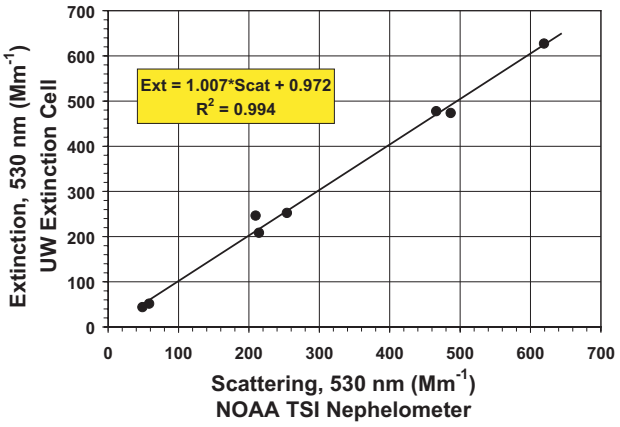

Figure 3.13. Comparison of extinction versus scattering for white aerosols. The scattering measurements from the TSI nephelometer were corrected for angular nonidealities and adjusted to the OEC wavelength through log interpolation.

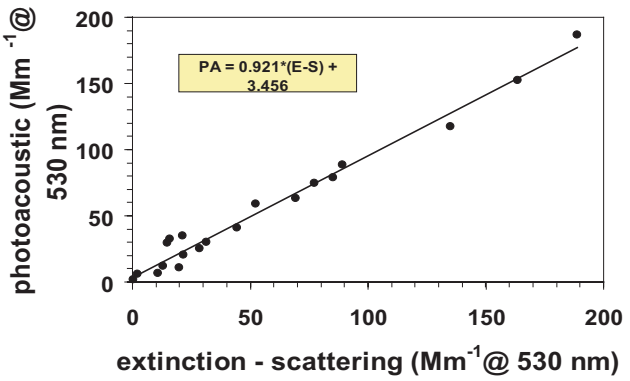

Figure 3.14. Comparison of aerosol light absorption coefficient measured by a photoacoustic instrument versus the difference of extinction and scattering.

DOE Atmospheric Radiation Measurement Program Aerosol Intensive Observation Period, May 2003

To gain an improved understanding and model-based representation of aerosol radiative influence, an Intensive Observational Period (IOP) was conducted at the Department of Energy's Atmospheric Radiation Measurement (ARM) Southern Great Plains (SGP) Cloud and Radiation Testbed (CART) site in north central Oklahoma, 5-31 May 2003. CMDL aerosol scientists participated in this experiment using ground and airborne measurements of aerosol absorption, scattering, and extinction over the SGP site to characterize the routine ARM aerosol measurements and to help resolve differences between measurements and models of diffuse irradiance at the surface. The assessments of aerosol optical thickness and aerosol absorption were carried out in conjunction with measurements of downwelling, direct, and diffuse irradiance as a function of wavelength and altitude. Data from the IOP will be used to conduct a variety of closure experiments on aerosol optical properties and their radiative influence. Measurements of the aerosol chemical composition and size distribution will allow testing of the ability to reconstruct optical properties from these measurements. Additional effort was directed toward the measurement of CCN concentration as a function of supersaturation and relating CCN concentration to aerosol composition and size distribution. This relationship is central to characterizing the aerosol indirect effect.

IOP Scientific Questions

- How well do routine CART Raman lidar and In Situ Aerosol Profiling (IAP) measurements portray aerosol scattering, extinction profiles, and aerosol optical thickness (AOT)?
- How well can the surface measurements of the aerosol scattering humidification factor be used for aerosols aloft?
- Can closure between measurements and models of diffuse radiation be achieved under low AOT conditions with accurate measurements of the aerosol single scattering albedo?
- How well can the cloud nucleating properties of particles just below cloud base be represented using surface measurements of particles with profiles of relative humidity and aerosol extinction?

- What is the relationship between the cloud base CCN number concentrations and size distributions, cloud base turbulence, and cloud droplet number concentrations and size distributions?
- To what extent are remotely sensed parameters adequate for detecting the indirect effect (e.g., what is the response of cloud drop effective radius to changes in aerosol extinction for clouds of similar liquid water path)?

The aerosol IOP was conducted 5-31 May 2003 over the ARM SGP Central Facility near Lamont, Oklahoma. There were 16 science flights for a total of 60.6 flight hours conducted by the CIRPAS Twin Otter aircraft on 15 days during this period. Most of the Twin Otter flights were conducted under clear or partly cloudy skies to assess aerosol impacts on solar radiation. Additional flights were utilized to target mostly cloudy skies to assess aerosol/cloud interactions, to test our understanding and model representation of aerosol activation, and to test how well surface remote sensing of the indirect effect works. An additional series of flights was conducted during this IOP by a specially instrumented Cessna C-172 aircraft leased by the Department of Energy (Figure 3.15). CMDL outfitted this airplane with instruments for the in situ measurement of aerosol optical properties in the lower troposphere.

The field deployment phase of the aerosol IOP was successful in a number of ways. The instruments deployed on the aircraft and on the surface acquired the requisite data to address the IOP objectives. These instruments included both well established and newly developed airborne instruments to measure aerosol optical properties (scattering, absorption, and extinction), aerosol size distribution, and CCN, as well as surface-based instruments to measure aerosol composition, mass, size distributions, aerosol optical properties, and CCN. Airborne and surface-based instruments were also used to acquire the necessary solar direct and diffuse measurements.

During the IOP several different data sets that will be used to address the IOP objectives were successfully acquired. One objective of the IOP was to measure aerosol optical properties (scattering, absorption, and extinction) using a number of different instruments simultaneously with measurements of direct and diffuse solar radiation in order to better understand and model the impact of aerosols on direct and diffuse radiation. Particular emphasis was placed on the role of aerosol absorption. Data to examine this issue and to accurately characterize aerosol absorption were obtained during a number of flights. Another objective was to examine the ability of routine Raman lidar and IAP measurements to characterize ambient aerosol extinction. Four coordinated flights were conducted so that these measurements could be evaluated using the more extensive instrumentation on the CIRPAS Twin Otter. This IOP represented the first time the ARM program acquired airborne CCN measurements over the SGP site. These data will be used to assess how aerosols impact cloud properties and to help develop algorithms using routine ARM surface and remote sensing data to model cloud properties and their impact on radiation.

Figure 3.15. The Department of Energy's Cessna C-172 aircraft. This aircraft provided a platform for CMDL aerosol instrumentation during the May 2003 Aerosol IOP.

A number of new and/or upgraded instruments were deployed over the CART site for the first time during this mission. For example, two new instruments, a cavity ring-down instrument (National Aeronautics and Space Administration (NASA), Ames) that measured both aerosol extinction and scattering, and a photoacoustic sampler (Desert Research Institute, (DRI)) that measured aerosol absorption, were deployed. A newly developed stabilized platform for zenith viewing radiometric instruments was also deployed on the CIRPAS Twin Otter aircraft and worked well for most of the mission, including the flights designed to assess direct and diffuse radiation. New surface and airborne instruments (California Institute of Technology and DRI) to measure CCN were also deployed.

Several times during the IOP, elevated aerosol layers were observed over the CART site. These layers, which were present 2-5 km above the surface, are often the result of the transport of smoke, dust, or pollution from long distances away. Observations of these layers during the IOP indicate these layers may be more common than originally thought and can have a substantial impact on the atmospheric radiation budget. Figure 3.16 shows CMDL aerosol data from a C-172 vertical profile flight over the CART site on a day where these layers were present.

CIRPAS Twin Otter flights were also conducted in coordination with overpasses of NASA Terra and Aqua satellites. These aircraft and satellite measurements will be used to evaluate how the satellite, airborne, and surface network measurements can be used to study the horizontal variability of aerosols and clouds.

The IOP participants are beginning the process of examining the individual instrument data to assess data quality and to initiate other data analyses. Mission reports can be found at the mission status site at http://dq.arm.gov/~dbond/cgi-bin/aer2003/status.pl. Authorized participants can read the reports of planning and debriefing meetings, scientific observer reports, and more at http://iop.archive.arm.gov/a03ftp/incoming/MeetingNotes ObserverLogs/. By agreement, preliminary quality-assessed guest instrument data will be delivered to the ARM IOP archive for access by the IOP participants. The ftp site for this is http://iop.archive.arm.gov/a03ftp/incoming/. These data are meant for early analyses and should not be used without first consulting the appropriate Principal Investigator. These data are publicly available.

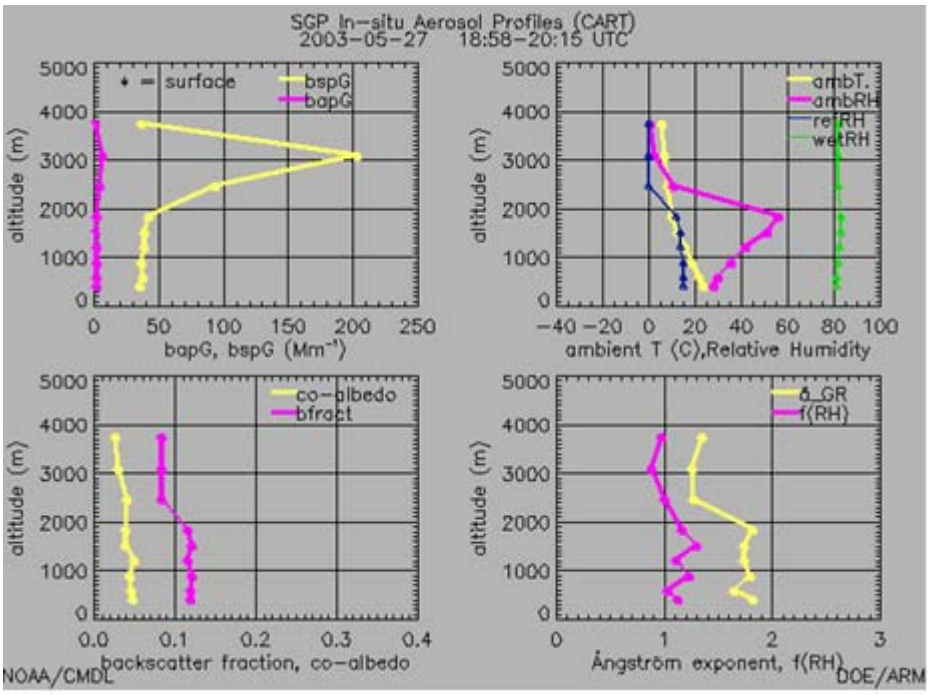

Figure 3.16. Aerosol data from a C-172 flight where elevated aerosol layers were observed. Data points represent the average of level flight segments at different altitudes. The layer was heaviest at ~3000 m above sea level, as shown by the scattering coefficient (yellow trace) in the upper left panel.

Mountaintop Cloud Study, Åre, Sweden

A month-long field campaign was conducted on the Swedish peak Åreskutan (63°N 13°E, 1250 m) in July 2003 to study the interactions between aerosol particles and clouds. At a field laboratory near the top of the mountain, researchers from the University of Stockholm (Sweden); Max-Planck Institute for Chemistry (Mainz, Germany); University of Washington (Seattle); Scripps Institution of Oceanography (La Jolla, California); and CMDL (Boulder, Colorado) measured the chemical composition, size distribution, and radiative properties of aerosol particles within cloud droplets, in the interstitial air between cloud droplets, and in cloud-free air. The primary questions addressed during the project were:

- How does chemical composition influence which particles are scavenged by clouds?
- How are the radiative properties of aerosol particles changed by clouds?
- What are the sources for individual particles on which cloud droplets form?
- How do anthropogenically produced particles influence cloud properties?

CMDL operated duplicate sampling systems for determining the light scattering and absorption of two classes of particles: cloud droplet nuclei (the particles that remain when cloud droplets evaporate) and the unscavenged particles in interstitial air. Together, these two classes represent the total population of particles present, and the fractional scavenging of scattering and absorbing particles can be derived continuously during a cloud event. Interstitial particles were sampled through an inlet that removed particles and droplets smaller than about 5-µm diameter, which is considered to be the dividing line between aerosol particles and cloud droplets. A counterflow virtual impactor (CVI), [*Ogren et al*., 1985] extracted droplets larger than about 5-µm diameter from cloudy air and transferred them to a carrier flow of warm, dry, filtered air. In both inlets the light scattering and absorption measurements were made at low relative humidity and, therefore, the two classes of particles could be directly compared.

In addition to the standard suite of aerosol measurements, CMDL scientists also set up a simple digital-camera system to measure visibility within clouds on the mountaintop. Images were collected every minute and analyzed digitally to determine changes in contrast from black-and-white targets over the course of the study. The Koschmeider equation was used to calculate the visibility based on the contrast measurements. Figure 3.17a, taken under cloud-free conditions, shows the five black-and-white targets mounted at distances ranging from 10 to 90 m from the camera. Only two of the targets are visible in Figure 3.17b, taken 1 minute later after the site was quickly enveloped in a dense cloud. The visibility, calculated from the contrast between the black and white areas in the two visible targets in the second photo is 40 m, consistent with the fact that the third target 55-m away is not visible. This simple, automated target imaging system provided a measurement of incloud visibility 24 hours a day under the special lighting conditions in the summer in northern Sweden. These measurements will prove useful in identifying cloudy periods at times when the CVI system was not running and, therefore, the effects of cloud scavenging on aerosol scattering and absorption can be evaluated even when the instruments were running unattended.

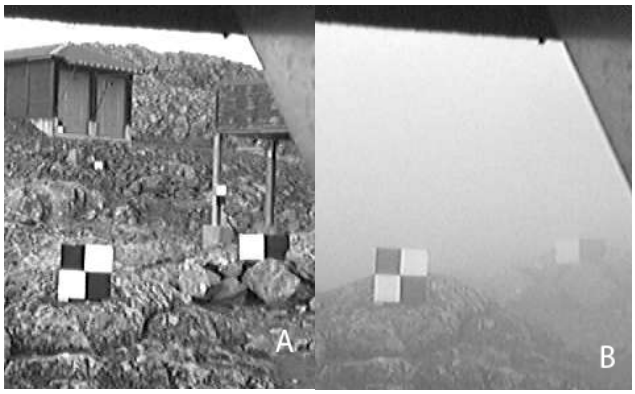

Figure 3.17. Digital camera images of black-and-white targets used to determine visibility at the *Åre* site before (A) and during a cloud event (B).

Development of Aerosol Models for Radiative Flux Calculations

Highly generalized standard aerosol models are used in radiative transfer computations to represent aerosol types and to characterize their radiative impact in the atmosphere. When measurements and models are compared, disagreements may be due to assumptions made in the development of these generalized models. CMDL's long-term measurements of aerosol optical, microphysical, and chemical properties are used to derive a new set of aerosol models based on observational data. These models aim to provide an internally consistent specification of aerosol optical and microphysical properties compatible with the requirements of standard radiative transfer codes. These specifications will allow us to estimate the aerosol-induced uncertainty in radiative flux calculations based on specification of aerosol type rather than on coincident aerosol measurements.

Long-term data sets from both midlatitude continental (SGP, 6 years) and Arctic marine environments (BRW, 5 years) are used to produce a set of aerosol models. The trajectory cluster approach described in the work of *Harris and Kahl* [1994] was used to identify aerosol source regions and segregate the aerosol optical data based on the trajectory clusters (Figure 3.18). The input data includes aerosol light extinction, single-scattering albedo, Ångström exponent, back scattering fraction, sub-micron scattering, and absorption fractions. Other aerosol data available for a shorter time period (e.g., aerosol chemistry, hygroscopic growth, and aerosol optical depth) are also used to examine the clusters for consistency. Significant differences are evident in some, but not all, long-term aerosol optical properties for the trajectory clusters at the two sites suggesting that air mass origin determined by trajectory analysis is a weak indicator of aerosol type. Figure 3.19 shows the aerosol extinction (σ_{ext}) and single scattering albedo (ω_0) for each of the trajectory clusters at SGP (top) and BRW (bottom).

At SGP two trajectory clusters originating over urban and industrial areas (T1 and T2) have the highest aerosol loading but can be distinguished from each other based on disparate chemistry and particle size measurements. The T2 cluster, which extends past the Gulf of Mexico and into the Caribbean Sea, has larger particles and its chemistry is indicative of a marine aerosol. The T1 cluster, which originates closer to the coast, has the highest SO_4 and NH_4 mass fractions of all the trajectory clusters. Three clusters originating northwest of the SGP site (T4, T5, and T6) have very low aerosol loadings. T6, which originates south and west of the Aleutian Islands, has the lowest ω_0 of any of the trajectory clusters and the highest Ca^+ mass fraction. This suggests intercontinental transport of aerosol from Asia, but may also be caused by local dust during high winds.

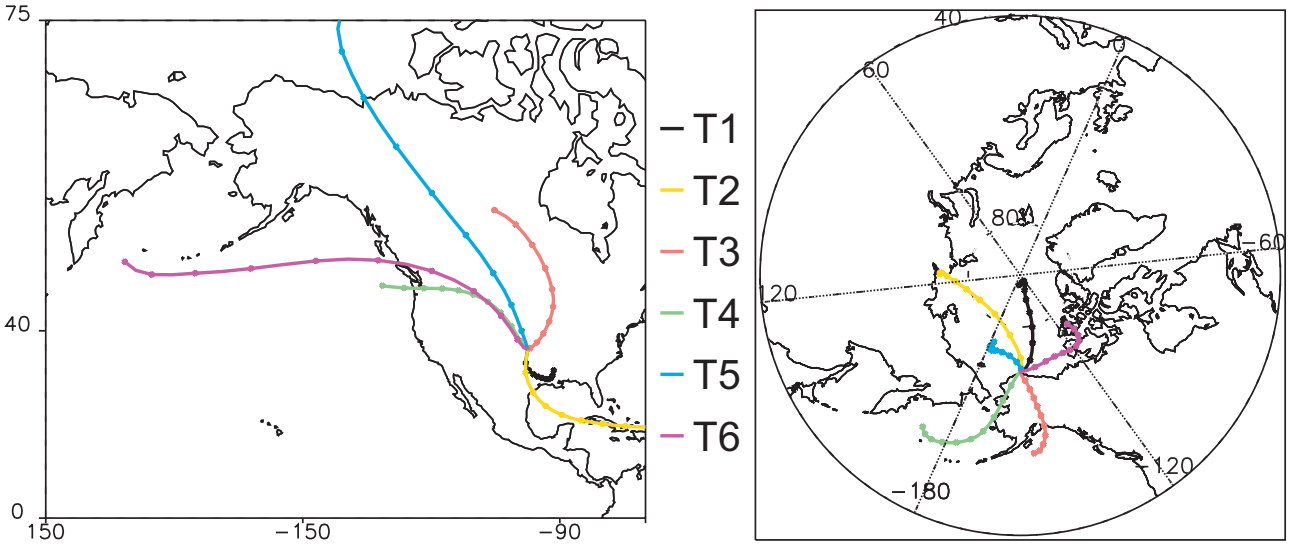

Figure 3.18. Clusters of 10-day 500-m back trajectories arriving at (a) SGP and (b) BRW.

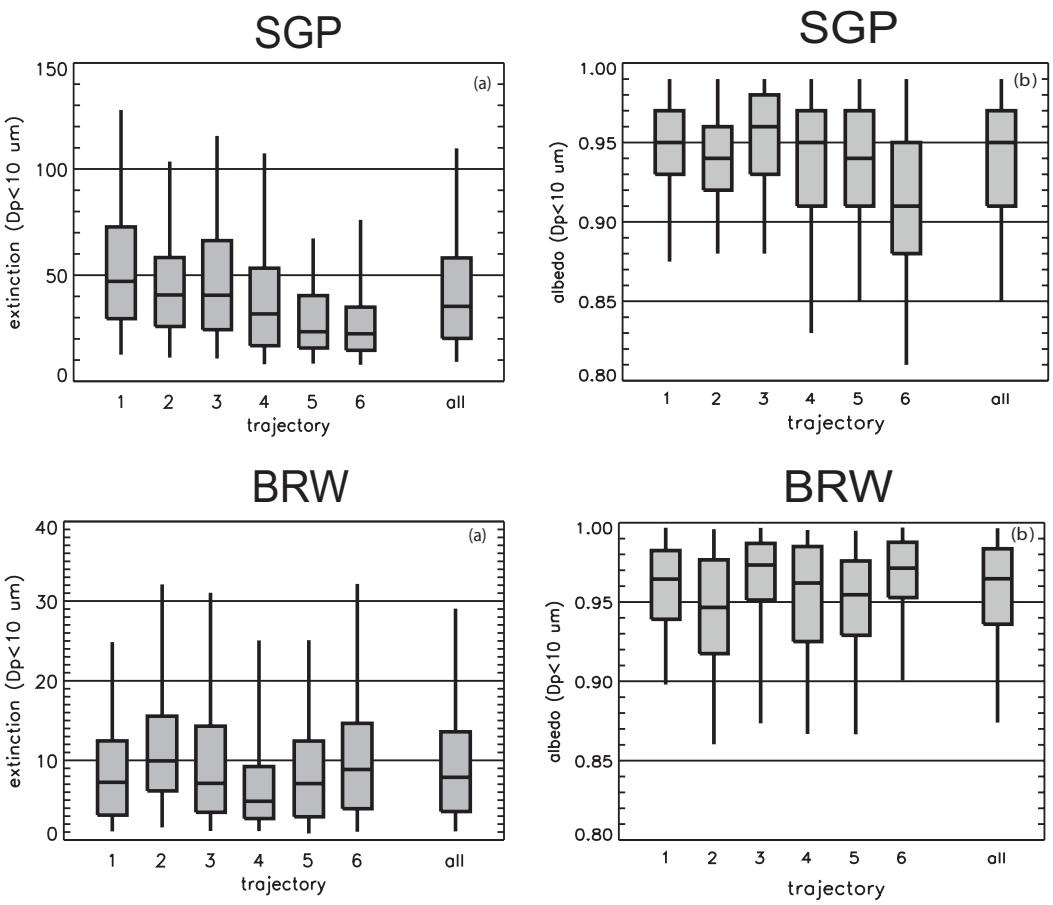

Figure 3.19. Box whisker plots of: top (a) aerosol extinction and (b) single-scattering albedo as a function of trajectory cluster for SGP and bottom (a) aerosol extinction and (b) single-scattering albedo as a function of trajectory cluster for BRW.

Trajectories arriving at Barrow, Alaska, from Siberia (T2) have higher aerosol loading and more absorbing particles. The Siberian air masses are temporally consistent with the springtime Arctic haze phenomenon. In contrast, the summertime trajectories originating in the Bering Sea (T4) have the lowest aerosol loading of any of the six trajectory clusters. The chemistry data for the Bering Sea trajectory cluster are of a clean marine aerosol type, with high mass fractions of Na^+ and methane sulfonate (MSA). Both the Arctic haze and clean marine aerosol observations are consistent with the results reported in the work of *Quinn et al.* [2002] at Barrow.

Statistical analyses, including principal components and discriminant analysis, will provide a more distinct categorization of aerosol types and their radiative properties. Inputs include aerosol scattering, absorption chemistry, local meteorology, and trajectory cluster. Preliminary analyses suggest that distinct aerosol types do not exist at any one point in time; rather, the measured aerosol at any time is a mixture of two or more general types. Classification of individual observations into these groups and calculation of relevant radiative properties (e.g., optical depth and single scattering albedo) within these groups will provide increased accuracy in the computation of aerosol radiative effects at regional and global scales.

3.2. Solar and Thermal Atmospheric Radiation

E. Dutton (Editor), G. Anderson, G. Carbaugh, D. Jackson, D. Longenecker, D. Nelson, M. O'Neill, R. Stone, J. Treadwell, and J. Wendell

3.2.1. Radiation Measurements

Introduction

The CMDL Solar and Thermal Atmospheric Radiation (STAR) group conducts surface irradiance and optical depth observations that provide supporting information for baseline climate monitoring activities. The group also investigates causes and consequences of trends and variations in components of the observed surface radiation budget. Energy associated with the Earth's radiation budget is not only responsible for maintaining the thermal state of the planet's atmosphere and oceans but also affects their motions and related processes. Expected trends in surface radiation quantities at globally remote sites, directly caused by anthropogenic activities, are near or below the level of detectability on the decadal time scale. However, there are gaps in the knowledge of basic climatological variability in the global surface radiation budget; therefore, STAR measurements can

contribute to a fundamental understanding of atmospheric and climatological processes. These contributions include definition of diurnal and annual cycles and effects of cloudiness, actual variation on daily to decadal time scales, major volcanic eruptions, unexpectedly high concentrations of anthropogenic pollution in the Arctic, constituent variations on narrowband irradiance (e.g., ozone and ultraviolet (UV) changes), and possible anthropogenic modification to cloudiness. The STAR group makes remote sensing measurements of various atmospheric constituents potentially responsible for variations in surface radiation quantities, particularly aerosol optical depth. In addition to the research conducted by CMDL and the locally and internationally maintained data archives, STAR measurements contribute to several global databases needed to evaluate radiation and energy budgets in diagnoses of the climate. STAR observations also contribute to satellite-based projects by helping to verify point estimates that allow intervening features of the atmosphere to be deduced.

A major goal of the monitoring program is to obtain a record of surface radiation parameters that is as long and as complete as possible and can be examined for all scales of natural and modified variability. Of particular interest is the determination of the magnitude, representativeness, and possible consequences of any observed changes. To this end, the STAR group maintains continuous surface radiation budget observations at several globally diverse sites along with various ancillary observations. The following sections summarize those projects while highlighting the changes and new results that have occurred since the previous CMDL Summary Report [*King et al.*, 2002].

Field Sites

Surface radiation measurements were made at the four principal CMDL baseline observatories BRW, MLO, SMO, and SPO since the mid-1970s with some measurement series going back to 1957. The different environments and observing conditions at the sites resulted in somewhat different measurement programs evolving at each site. Three additional sites (Bermuda, BRM; Kwajalein, KWJ; and Boulder Atmospheric Observatory, BAO) were added in the late 1980s and early 1990s; another site, THD, was added in 2002. Details on the earlier sites are given in previous CMDL Summary Reports. Table 3.6 shows the current observations made at each of the field sites. The records acquired at the four main CMDL sites constitute some of the longest known series available by the United States for solar radiation research. The raw data from the field are transmitted from the field sites over telephone lines or the Internet to the central data processing facility in Boulder where data editing, final calibrations, graphical inspection, and archiving are performed as discussed in section 3.2.4.

Basic Measurements

Broadband irradiance. Basic broadband measurements at each of the four baseline observatories include normal direct and downward broadband solar irradiance and downward solar irradiance in the 0.28-µm to 2.8-µm band. Downward broadband thermal irradiance measurements were added at all sites in recent years as well as upwelling irradiance measurements at SPO and BRW. The current suite of measurements at all sites is shown in Table 3.6. Data are sampled at 1 Hz with 1-minute averages recorded on computer media. Preliminary data from all CMDL radiation sites are generally available graphically within a couple of days of acquisition in the radiation section of the CMDL Web site (section 3.2.4). Example applications and results from this program are described in section 3.2.6. STAR has also been involved in the ongoing development of improvements to broadband radiometry that has led to considerable improvement in measurement uncertainties as described in the works of *Ohmura et al.* [1998]; *Dutton et al.* [2001]; *Philipona et al.* [1998, 2001]; *Marty et al.* [2003]; and *Michalsky et al.* [1999, 2003].

Filter wheel NIP. The wideband spectral direct solar irradiance measurements are made with a filter wheel normal incidence pyrheliometer (FWNIP). Data can be compared to a

Table 3.6. Measurement Types Made at Each Station, 2002-2003

	BRW	Bermuda	BAO	MLO	Kwajalein	SMO	SPO	THD
Broadband Irradiance (until otherwise noted)								
Direct solar beam	X	X	X	X	X	X	X	X
Diffuse solar	X	X	X	X	X	X	X	X
Total downward solar	X	X	X	X	X	X	X	X
Reflected solar	X		X				X	
Downward IR	X	X	X	X	X	X	X	X
Upward IR	X		X				X	
Other Measurements								
Spectral optical depth	X	X	X	X	X		X	X
All-sky digital imagery	X	X	X					
UV-B	X	X	X	X	X			
High-resolution spectral UV			X*	X				
Wideband direct solar irradiance (FWNIP)	X			X		X	X	

BRW, Barrow, Alaska; BAO, Boulder Atmospheric Observatory (Erie, Colorado); MLO, Mauna Loa, Hawaii; SMO, American Samoa; SPO, South Pole, Antarctica.

*Instrument located in Boulder about 16 km west of BAO.

high-spectral-resolution radiative transfer model [*Bird and Riordan*, 1986] based on Beer's law and is intended for use at the surface only. The aerosol optical depth and precipitable water are adjusted within the model to obtain the best match with the FWNIP observations. This provides a low-precision but relatively stable estimate of mean visible aerosol optical depth and water vapor at the four baseline observatories. The accuracy of the method for obtaining aerosol optical depth and water vapor is limited by the dependence on the absolute values of the extra-terrestrial solar spectrum and instrument calibration, unlike other typical applications in sunphotometry. The updated data records from these observations are shown in Figure 3.20 through near the end of 2001. The accuracy of the data is on the order of 0.03 optical depth units, or about 2 to 3 times poorer than sunphotometer-derived values and should only be used when sunphotometer-derived data are not available.

Spectral aerosol optical depth. Another major observational effort within STAR is the determination of spectral aerosol optical depth using sunphotometry. Sunphotometer methods are more recent than those developed for the FWNIP and are more accurate and capable of producing much greater spectral resolution. These data are used for interpretation of the extent of aerosol influence on surface irradiance observations. Information on the physical and optical nature of aerosols can be deduced from these measurements. CMDL has been involved in making AOD measurements for many years, but only recently have these measurements been maintained and processed as an operational network activity within CMDL.

Continuous sunphotometer measurements at MLO began in 1983 using the Physikalisch-Meteorologisches Observatorium Davos (PMOD) sunphotometer [*Dutton et al.,* 1991]. Network operations began in 1996 with the installation of Multi-filter Rotating Shadowband Radiometer (MFRSR) instruments at several sites. A precision-filter radiometer (PFR) from PMOD was installed at MLO in 1999. A Carter Scott SP01 sunphotometer was installed at BRW and SPO in 2000. Beginning in 2001 the MFRSRs were replaced with Carter Scott SP02 sunphotometers. Additional sites and instruments were added in the following years (Table 3.7).

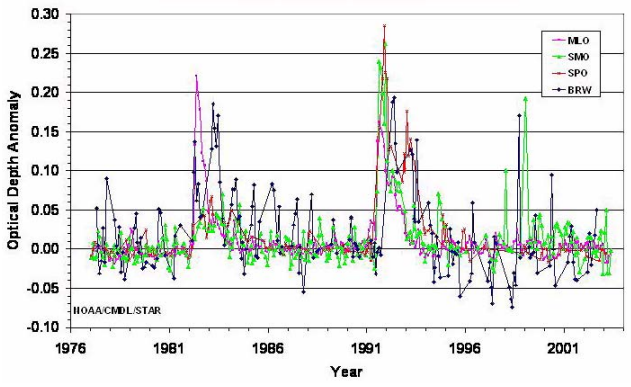

Figure 3.20. Aerosol optical depth monthly mean anomalies (filter wheel NIP estimated).

Table 3.7. Station Instrument History for AOD Measurements

Station	Instrument	Dates
BRW	SP01	14 March 2000 to 19 Nov. 2003
BRW	SP02	8 March 2001 to 14 June 2002
THD	SP02 (two instruments)	10 April 2002 to date
BAO	SP02	26 April 2001 to date
BAO	MFRSR	6 Aug. 1996 to 5 Feb. 2001
BLD	MFRSR	9 July 1999 to date
BRM	SP02	23 July 2003 to date
BRM	MFRSR	20 Feb. 1996 to 18 Sept. 2002
MLO	PFR	2 Nov. 1999 to date
KWJ	SP02	25 July 2001 to date
KWJ	MFRSR	9 Oct. 1996 to 19 Aug. 2000
SPO	SP01	6 Nov. 2000 to 27 Oct. 2001
SPO	SP02	5 Nov. 2001 to 18 Sept. 2003

BAO, Erie, Colorado; BLD, Boulder, Colorado; BRM, Bermuda; BRW, Barrow, Alaska; KWJ, Kwajalein, Marshall Islands; MLO, Mauna Loa, Hawaii; THD, Trinidad Head, California; SPO, South Pole, Antarctica

Table 3.8. Station Names and Geographical Locations

Station	Location
Barrow Observatory (BRW)	Barrow, Alaska (Lat. 71.32°N, Long. 156.60°W)
Trinidad Head (THD)	Trinidad Head, California (Lat. 41.05°N, Long. 124.15°W)
Boulder Atmospheric Observatory (BAO)	Erie, Colorado (Lat. 40.05°N, Long 105.08°W)
CMDL (BLD)	Boulder, Colorado (Lat. 39.99°N, Long. 105.26°W)
Prospect Hill (BRM)	Hamilton, Bermuda (Lat. 32.31°N, Long 64.76°W)
Mauna Loa Observatory (MLO)	Mauna Loa, Hawaii (Lat. 19.52°N, Long. 155.60°W)
Kwajalein(KWJ)	Kwajalein, Marshall Islands (Lat. 8.72°N, Long. 167.72°W)
South Pole (SPO)	South Pole, Antarctica (Lat. 90.00°S, Long. 102°W)

Table 3.9. Instruments in Use at CMDL Field Sites and Their Wavelengths

Station	Instrument	Wavelengths (nm)
BRW	Carter-Scott SP01	367.0, 413.0, 499.0, 675.0, 865.0
THD	Carter-Scott SP02	412.5, 500.2, 675.7, 862.6, 368.8, 501.1, 610.0, 778.8
BAO	Carter-Scott SP02	411.8, 500.6, 675.5, 862.3
BLD	MFRSR	415.0, 500.0, 615.0, 673.0, 870.0, 940.0
BRM	Carter-Scott SP02	411.8, 500.3, 675.1, 861.7
MLO	Precision filter radiometer	367.6, 412.0, 501.2, 862.4
KWJ	Carter-Scott SP02	411.5 500.4 675.4 861.8
SPO	Carter-Scott SP02	411.5 499.7 675.1 861.8

BAO, Erie, Colorado; BLD, Boulder, Colorado; BRM, Bermuda; BRW, Barrow, Alaska; KWJ, Kwajalein, Marshall Islands; MLO, Mauna Loa, Hawaii; THD, Trinidad Head, California; SPO, South Pole, Antarctica

The STAR group is currently making aerosol optical depth measurements at eight sites. Tables 3.8 and 3.9 show the exact location of the sites used for determining solar position angles, the instruments used, and the wavelengths observed. Data for all instruments are obtained with 1-minute resolution. Values between air mass 5 and air mass 2 are used to determine instrument calibrations, V_0, derived from a Langley plot application of Beer's law. At least 30 observations within 100 minutes of air mass 5 must be available or the Langley plot is not attempted. Raw voltages are automatically downloaded, screened, archived, and processed on a daily basis. Routine optical depth data analysis for all stations is performed on mornings and afternoons that produce acceptable Langley plots for near continual on-site instrument calibrations.

To produce the Langley plot, the data are filtered using subjective criteria and the residuals produced by an initial least-squares linear fit. Outliers suspected to be caused by gross errors are removed. The data is fit a second time and then filtered with a stricter set of criteria intended to screen minor cloud and other inhomogeneous conditions. The data is then fit a third and final time. If fewer than 30 points remain at this time, the Langley fit is abandoned and processing skips to the next possible Langley period. Surviving Langley plots are examined for unexpected results that can appear in the automated processing.

The resulting V_0 time series is then smoothed three times with a moving 41-point smoother. After the first two smoothers have been applied, outlying points are removed and the data are then fit a final time. The most recent data are not smoothed beyond a given time until at least 20 succeeding acceptable V_0s are available. Figure 3.21 shows an example time series of sunphotometer Langley calibration results.

Optical depth is computed for every minute using Beer's law and the ten smoothed V_0s closest in time to the data point are used to calculate a mean V_0. Finally, a residual optical depth is calculated by subtracting other known components of optical depth, such as those due to Rayleigh scattering, ozone absorption, and absorption by other gases. In the absence of clouds, these residual optical depths are assumed to be due to aerosols and are typically identified as aerosol optical depth (Figures 3.22 and 3.23).

A cloud-screening algorithm will improve the usefulness of the results by removing obviously cloud-influenced data before the initial processing. Currently, station average pressure and temperatures are used to compute air masses. Using actual measurements will improve the air-mass values. Also, the actual pressure measurements will improve the Rayleigh optical depth values, and using ozone measurements instead of climatological averages will improve the ozone optical depth.

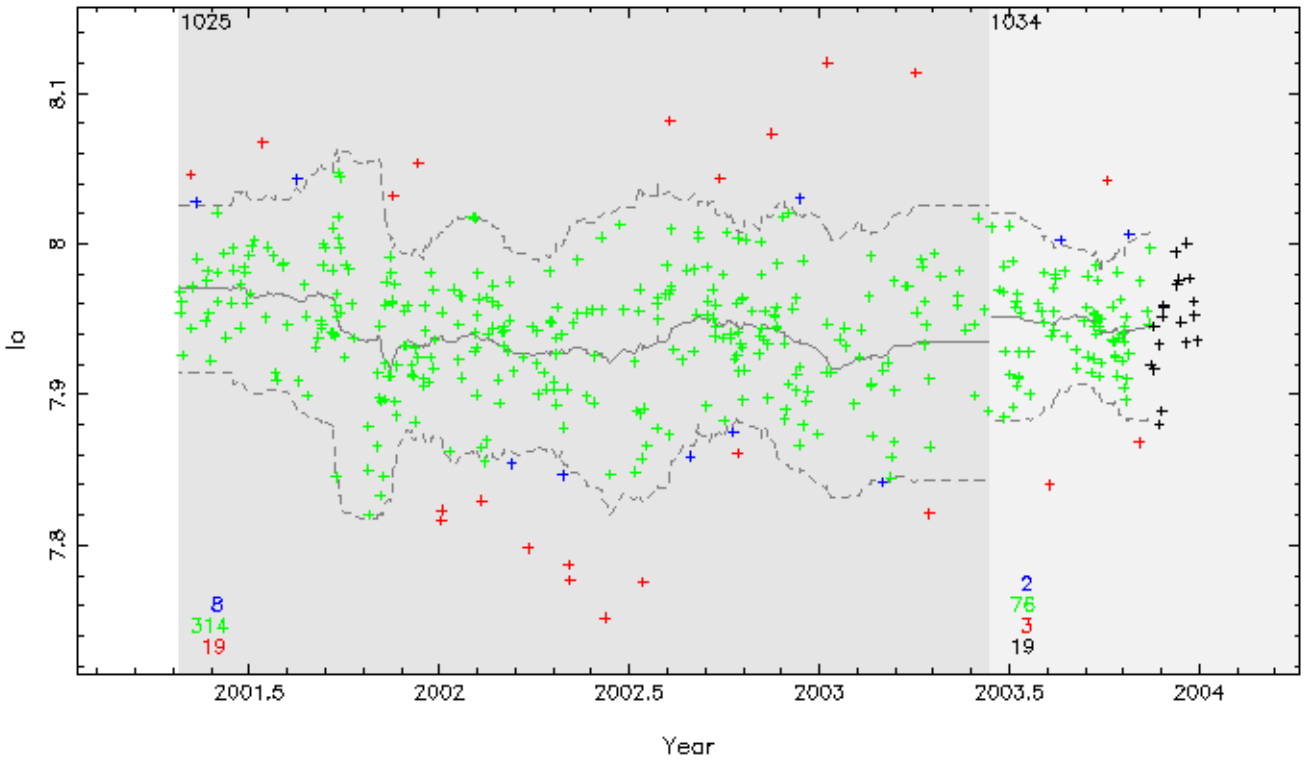

Figure 3.21. Ln(V_0) time series corrected for the Earth-Sun distance for the BAO SP02. The green-colored points represent Ln(V_0) from accepted Langley plots. The red-colored points were removed after the first smoothing and the blue-colored points were removed after the second smoothing. The black-colored points are the most recent and have not been smoothed. An instrument change is indicated by the vertical line at about Year 2003.43

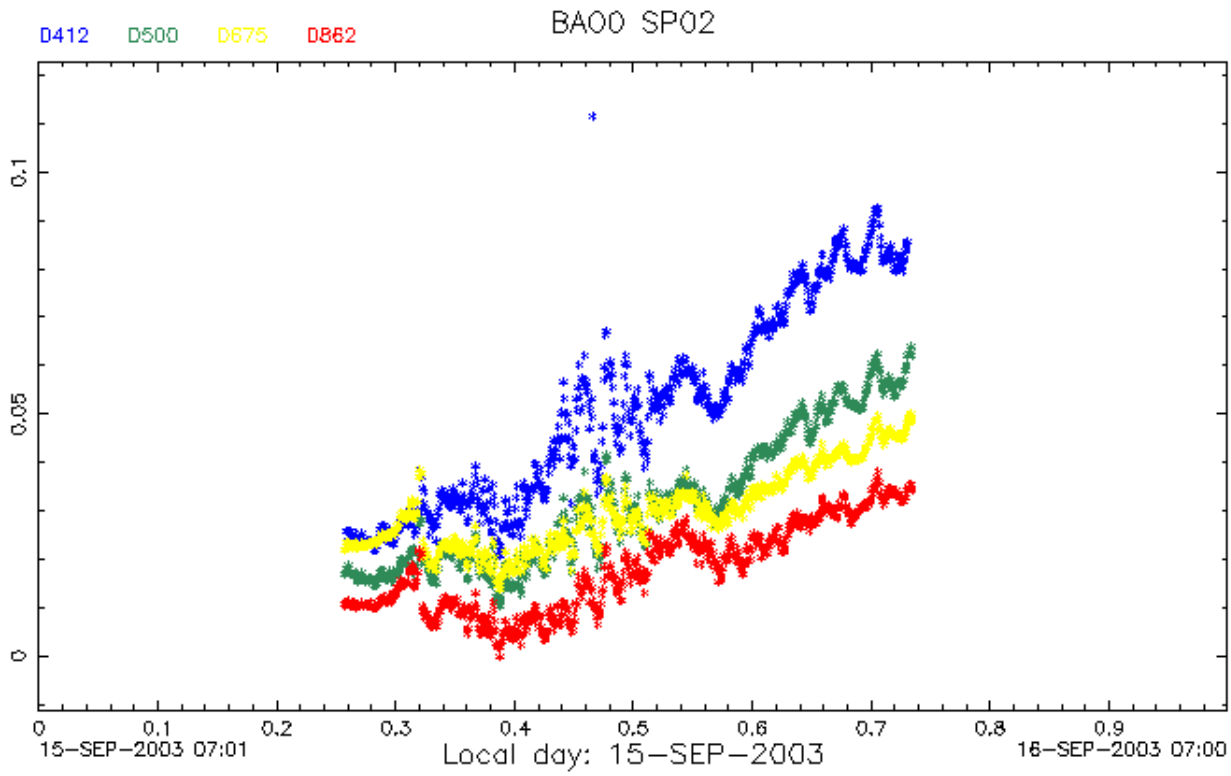

Figure 3.22. Aerosol optical depths for four wavelengths on a clear day at Boulder, Colorado (15 September 2003).

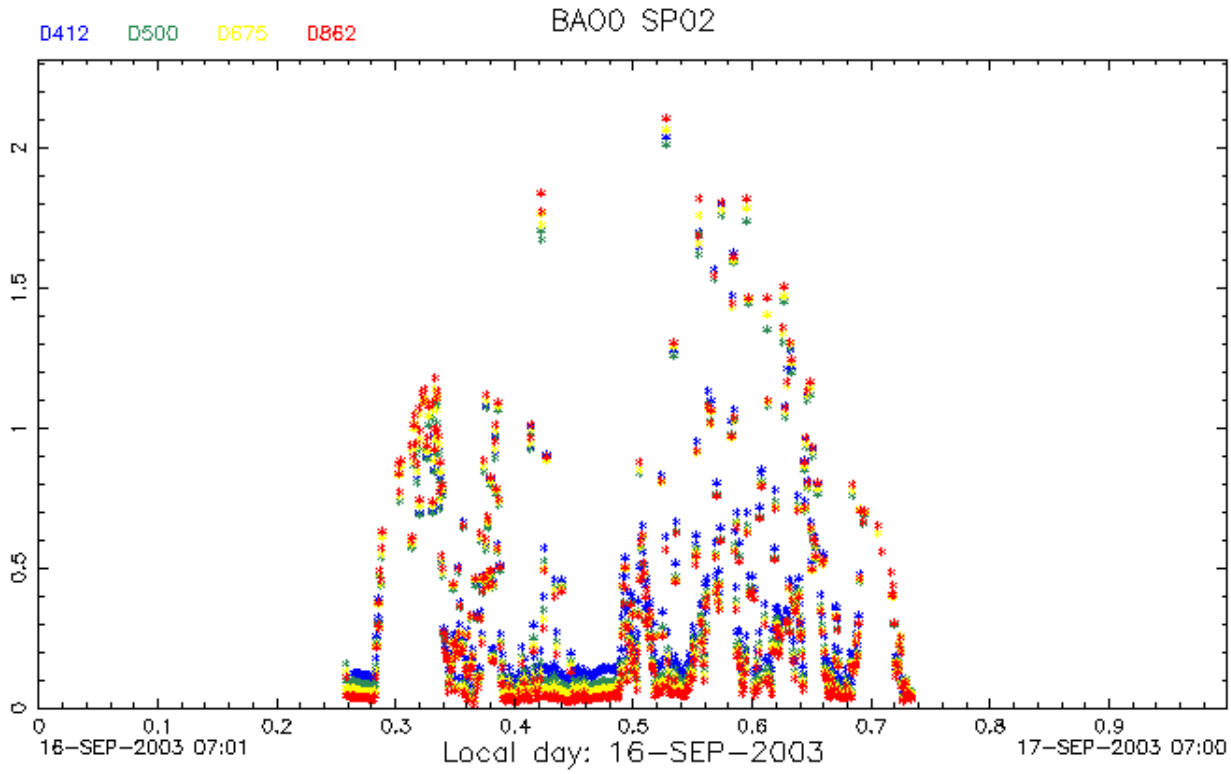

Figure 3.23. Residual optical depths for four wavelengths on a cloudy day at Boulder, Colorado (16 September 2003).

3.2.2. SOLAR RADIATION FACILITY

The Solar Radiation Facility (SRF) was active in its role as a source of field-site support, instrument calibration, and improvement in site monitoring operations during 2002 and 2003. Participation in international organizations such as Baseline Surface Radiation Network (BSRN) and Global Atmospheric Watch (GAW) was ongoing. At the 2002 BSRN meeting in Regina, Canada, some results of pyrheliometer measurements using Eppley Normal Incidence Pyrheliometers (NIPs) constructed with a 5° field-of-view and calcium-fluoride window were presented. SRF experience, to date, suggests that measurements of solar direct beam with these modified NIPs can generate irradiance readings that can achieve World Radiation Reference (WRR) accuracy when referenced to the absolute scale. The potential for this accuracy, however, is highly dependent on individual site operational practice, particularly regarding cleanliness of the NIP window.

The SRF deployed NIPs with five degree field-of-view and calcium-fluoride windows at the MLO, KWJ, BAO, BRM, and THD sites. These sensors are operated side by side with conventional NIPs to create redundancy and improve quality assurance and control of direct beam irradiance data. Redundant diffuse sky irradiance measurements are also performed at selected CMDL monitoring sites. Black and white detector-equipped pyranometers (Eppley model 848) were deployed at BAO, KWJ, SPO, and MLO.

All irradiance values reported by CMDL are traceable to WRR and SRF reference radiometers and annually compared with similar instruments at the National Renewable Energy Laboratory to maintain performance. Table 3.10 summarizes the most recent New River Intercomparison of Pyrehliometers (NRIP) results.

The tropical maritime environment at the Kwajalein BSRN presents a challenge for quality measurements. All sensors must operate at essentially sea level and are continuously subject to sea-salt spray. Direct-beam sensors are especially vulnerable; in 2002 a system to periodically rinse the sensor windows with fresh water and reduce salt-spray-droplet effects was implemented. The preliminary attempt used a simple timer along with locally available tap water and proved encouraging. Therefore, in 2003 the system was augmented with a water pump and reservoir. Also a blower system was added to continuously flush the direct beam sensors with filtered interior building air that is relatively free of salt-spray particles. The curtain of clean air reduces the accumulation of salt spray droplets on the sensor windows and contributes to data quality.

Table 3.10. Recent Historical Solar Radiation Facility Standards (SRF) Comparison Results

Pyrheliometer Comparison	TMI 67502 WRR Factor	AHF 28553 WRR Factor	AWX 32448 WRR Factor
IPC VIII (1995)	0.99869	0.99756	
NPC 1998		0.99783	
NPC 1999		0.99741	1.00086
IPC IX (2000)	0.99966	0.99733	1.00038
NPC 2001		0.99704	1.00073
NPC 2002			
NPC 2003	1.00076	0.99713	

The calibration of sensors and methods to transfer the WRR to various types of sensors continues to be an area of interest at SRF. Incorporation of these response features in operational sensor data analysis, together with operational sensor cleanliness, offers the greatest potential for the improvement of broadband irradiance data. The SRF continues to work with pyrheliometer field-of-view and window-material effects, temperature response, diffuse sensor calibration, and pyranometer zero offset. The publication of some of the long-term results of these investigations is planned for 2004 and 2005.

3.2.3. BASELINE SURFACE RADIATION NETWORK

The STAR group has the primary management role in BSRN and has carried out the duties of International Project Manager for the past 9 years. BSRN is intended not only to supply the international climate research community with the best possible surface irradiance data from a globally and climatologically diverse long-term network, but also to keep advancing the state of the art in improvements of those measurements so that research uses of the data can continue to be expanded. The BSRN program is part of World Climate Research Program (WCRP) and the Global Energy and Water Cycle Experiment (GEWEX). Support of the U.S. BSRN program comes from several agencies: NOAA National Weather Service, NWS; NOAA Oceanic and Atmospheric Research, OAR; National Aeronautics and Space Administration, NASA; and the U.S. Department of Energy, Atmospheric Radiation Measurement, DOE ARM. The network is funded internationally by more than 18 participating countries who operate more than 40 surface BSRN stations and contribute technical experts to the group's efforts. CMDL contributes five sites to the BSRN with more information on the project and data availability at http://bsrn.ethz.ch/. The BSRN data are being utilized in major satellite and Global Circulation Model (GCM) research programs. The program was conceived in 1988, began field operations in 1992, and is intended to operate indefinitely until there are no further extensive research needs for such data.

BSRN was invited to join the Global Climate Observing System (GCOS) global surface radiation monitoring network, thereby demonstrating the importance and success of this project. GCOS is an international effort designated by the United Nations Framework Convention on Climatic Change (FCCC) to coordinate and promote international observations of climate analysis and research. CMDL has the lead management responsibility for transitioning BSRN into a GCOS-qualified activity.

3.2.4. DATA PROCESSING

Solar and thermal radiation data, meteorological data, and spectral optical-depth data are downloaded from three of the baseline stations (BRW, MLO, and SMO), from the three BSRN sites (BAO, BRM, and KWJ), and from the new site at THD using Campbell data logging software and standard telephone lines. The same data are transmitted from the South Pole over the Internet. The frequency of the telephone downloads varies from station to station but is typically about six times per day. The Internet transfer occurs once per day and is scheduled to take place when the satellites are in communication with the South Pole.

All-sky cameras are currently deployed at BRW, BAO, and BRM, however, the BRM camera is not operating due to the aftermath of hurricane Fabian. Pictures from the BAO camera are downloaded to a server at the laboratory over a telephone connection at 1-hour intervals and posted to a Web page. A daily download of the cloud amounts is done each morning for the preceding day. The BRM camera will operate in the same fashion once repairs are complete. An Internet connection to the camera in BRW is used to collect its data.

Two all-weather cavity radiometers are operating. One is at the BAO site and the other is at CMDL SRF. Both of these use in-house developed software for operations and communications.

There is a three-site UV network in Alaska at St. Paul Island, Nome, and BRW. Telephone connections are used to download data files produced by the instruments at St. Paul and Nome; the BRW files are obtained via the Internet.

There are three other spectral instruments currently in operation. A MFRSR is run at the Boulder laboratory. This instrument creates its own data files that are downloaded via telephone. At MLO a Precision Filter Radiometer (PFR) operates in conjunction with PMOD. Its data are collected by a Campbell data logging system and transferred to the Boulder laboratory via the Internet. And lastly, there is an enhanced version of the spectral optical depth instruments operating in BRW. This instrument has its own computer that controls its operation with daily data transmissions to the Boulder laboratory.

The data are initially collected on two small computer systems. In the morning all data files are transferred to a server that screens the files and removes any bad records. The data are then archived according to station and project. Table 3.11 shows the station and projects in operation for 2002 and 2003. The archive files are organized in the same manner. Each record contains data for one time period. The number of fields in each record depends on the number of data channels for the project. A complete record of channel assignments is maintained for each site and project. This is used to match a particular measurement with its data value in the archive's records.

After the data are archived, daily plots are made. Some projects, radiation and meteorology for example, are displayed in engineering units, whereas other projects such as spectral optical depth are plotted in raw form. If the data archiving process fails for any reason, most of the data can be viewed directly from the unscreened data files. This procedure was implemented recently to allow access to raw voltages and resistances only. Verification of continuing operations can be made by this method.

For the radiation project, daily averages are made for all instruments. Plots and lists of these averages are then monitored to help detect trends and to view long-term performance. Also, nighttime averages are computed and graphed to view the instrument's performance during the night.

Where appropriate, data comparisons are made. One example is the comparison of the all-weather cavity with the NIPs at Boulder. Another example is the comparison of temperature measurements at BRW. Also, the albedo rack in BRW was recently replaced with a new one that is higher off the ground and farther away from the building. Both the old and the new albedo racks were in operation for approximately 2 years and their performance was compared to determine what effect, if any, the change to the new rack would have on the long-term data record. A new program is under development to merge and compare data.

The spectral optical depth data are analyzed daily and a Langley plot is produced if sufficient data are available. Aerosol optical depths are then calculated. See the Aerosol Optical Depth section (3.2.1) for further details.

A graphical editing program is used to edit radiation and meteorological data using both qualitative and quantitative methods developed in the laboratory. After the radiation and meteorological data are edited, monthly and annual averages are made. Data from BRW, BAO, BRM, KWJ, and SPO are archived at the BSRN headquarters in Zurich, Switzerland.

Table 3.11. STAR Field Measurements 2002 and 2003

Project Type	Abbreviation	Station
Radiation	RAD	BRW, THD, BAO, BRM, KWJ, SMO, SPO
Meteorology	MET	BAO, THD, BRM, KWJ
Spectral optical depth	SP02	BRW, THD, BAO, BRM, MLO, KWJ, SPO
All-sky camera	SKY	BRW, BAO, BRM
Arctic UV	BSI	BRW, NOME, STPL
All-weather cavity radiometers	CAV	BAO, BLD, BAO

BAO, Erie, Colorado; BLD, Boulder, Colorado; BRM, Bermuda; BRW, Barrow, Alaska; KWJ, Kwajalein, Marshall Islands; MLO, Mauna Loa, Hawaii; NOME, Nome, Alaska; STPL, St. Paul Island, Alaska; SMO, American Samoa; SPO, South Pole, Antarctica; THD, Trinidad Head, California

3.2.5. Spectral UV Measurements

The STAR spectral UV project was presented in some detail in the previous CMDL Summary Report [*King et al*., 2002] and is summarized here with additional results of some new work.

Solar radiation measured at the Earth's surface depends on the absorption and scattering of the atmosphere, the Earth-Sun distance, and the irradiance of the Sun. The UV portion of the spectrum is controlled primarily by Rayleigh scattering by air molecules, scattering by clouds, and absorption by ozone. Under clear-sky conditions, at a given site and for a given solar zenith angle (SZA), variations in UV are strongly correlated (inversely) with variations in total ozone. In July 1995, a UV spectroradiometer was installed at MLO (19.533°N, 155.578°W, 3.4 km) as part of the Network for the Detection of Stratospheric Change (NDSC). This spectroradiometer (labeled UVL) was in use from July 1995 until June 1997. The second instrument (UV3) was installed in November 1997 and continues in operation at MLO to the present.

To provide an additional site for these studies, a UV spectroradiometer (UVL, the same instrument initially installed at MLO) was installed at the Boulder laboratory (39.99°N, 105.261°W, 1.62 km) in June 1998. This instrument was replaced with a new instrument (UV4) in September 1999. Finally, the UV4 instrument was replaced with another new instrument (UV5) in August 2001 and continues in operation at Boulder to the present. All of these instruments (UVL, UV3, UV4, UV5) were constructed by the National Institute of Water and Atmosphere (NIWA) group at Lauder, New Zealand, under a

cooperative program agreement with CMDL. The various spectroradiometers used at MLO and Boulder are summarized in Table 3.12. The goal of this program is to study the relationship between UV and ozone and to determine long-term trends, if any, in UV. MLO and Boulder are both excellent sites for this study because of the prevalence of clear skies and the collocation of Dobson ozone spectrophotometers.

In August 2001, CMDL obtained the UV spectrometer UV5 that replaced an earlier spectrometer system (UV4) built by NIWA. During side-by-side observations with the world standard Dobson ozone spectrophotometer D083, a difference in retrieved total column ozone of ~5% was discovered. After investigating the cause of this difference, it was discovered that the ozone lookup table used to determine the total column ozone was generalized for use anywhere in the world. A new lookup table was produced using the Kylling-Mayer UV model LibRadTran version 0.99 to create parameters specifically for the Boulder location. The data set was then reprocessed with the new table to evaluate it.

Figure 3.24 shows the 18-month data set used in this evaluation. The Dobson ozone values are from the Boulder station instrument D061's AD direct sun observations only. The corresponding UV observation was chosen by being ±5 minutes of the Dobson observation.

The data in Figure 3.25 represents all of the data used in this investigation. It has not been filtered for sky conditions or for time of year. The line in the graph is the one-to-one correlation line. When the data was filtered by the sky conditions (clear, hazy, and very hazy), as reported by the Dobson observers, the corresponding subsets show very little difference between the clear and hazy conditions. The very hazy conditions did show a trend toward larger differences between the retrieved ozone values of the two instruments as was expected.

In Figure 3.26 the graph of the full data set shows the ratio of the two ozone values versus Mu, where Mu is approximated by $\cos(sza)^{-1}$. This graph shows a trend toward higher ratios as Mu decreases. When the data set is filtered for the differing sky conditions, as reported by the Dobson observers, each condition showed an ~1% increase in the slope of the trend line from the previous sky condition with the very hazy condition showing the largest slope. The standard deviation of the ratio data was calculated to be ~2.2%.

One difference between the two types of instruments is that the Dobson uses only the direct component of the solar radiation while the UV system uses the global (the direct plus the diffuse). Another difference is how the two instruments measure ozone.

Table 3.12. UV Spectroradiometers at MLO and Boulder

Instrument	Date
MLO	
UVL	July 1995–June 1997
UV3	November 1997–present
Boulder	
UVL	June 1998–September 1999
UV4	September 1999–August 2001
UV5	August 2001–present

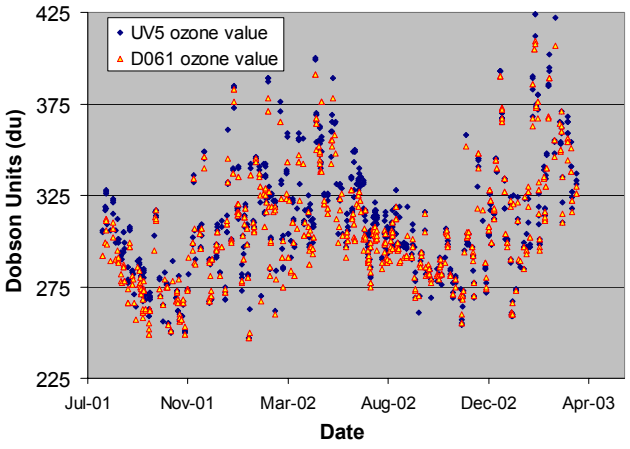

Figure 3.24. Total column ozone at Boulder, Colorado.

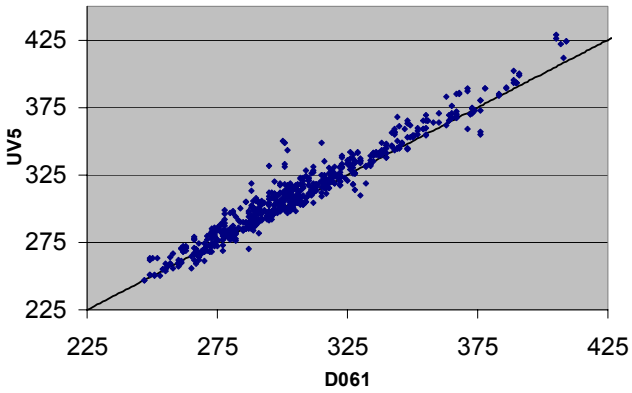

Figure 3.25. Correlation Plot of UV5 and Dobson spectrophotometer D061data sets.

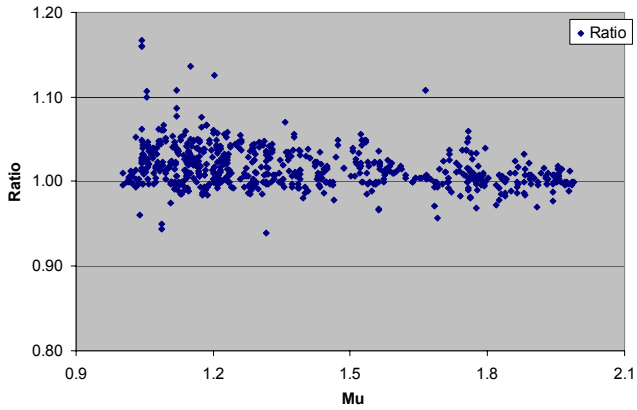

Figure 3.26. Dobson spectrophotometer D061/UV5 ratio versus Mu.

The UV system measures ozone by the Stamnes method [*Stamnes et al.,* 1991] that uses two independently and nonsimultaneously measured irradiances from which the synthetic 340/305 irradiance ratio is derived. The Dobson (R. Grass, *Observers' Manual Dobson Ozone Spectrophotometer*, 1987, CMDL internal publication) uses a double pair of wavelengths (for the AD double pair, it is the 325/305 and 340/311, respectively) that are directly compared inside the instrument to allow the scattering caused by the atmosphere and aerosols to be almost canceled out.

Figure 3.27 shows the UV5/D061 ratio along with the 415-nm optical depth measured by a Carter-Scott SP02 multi-channel sunphotometer at the David Skaggs Research Center (DSRC) Boulder, Colorado. The plot shows a strong correlation between the two data sets. When the optical depth is above ~0.2, the ratio shows an increase in the difference between the Dobson and UV system.

After reprocessing the UV5 data set from the DSRC and comparing it to the station Dobson D061, the total column ozone retrieved was found to be within the uncertainties of the Dobson ozone spectrophotometer when the optical depth is below ~0.2. It is apparent that use of optical depth measurements will help in determining the accuracy of the retrieved ozone from the UV5 instrument. It is recommended that, if possible, an instrument capable of measuring optical depth be colocated alongside any of the NIWA instruments to aid in determining the effects of aerosols and clouds on the UV measurements.

3.2.6. Applications and Results from STAR Research

MLO Apparent Transmission

The transmission for direct broadband solar irradiance through the atmosphere above MLO is monitored as a quantity known as the apparent transmission. This quantity is computed as the average of three successive ratios of direct solar irradiance, where each ratio is the quotient of the irradiance at an integer air mass divided by the irradiance at the next smaller integer air mass, as first defined in the work of *Ellis and Pueschel* [1971]. The apparent transmission measurement is inherently stable over time because it is independent of a radiometer calibration value and is, therefore, also quite sensitive to small changes in transmission that can be due to aerosols, ozone, or water vapor.

Studies by *Bodhaine et al.* [1981] and *Dutton et al.* [1985] have shown that aerosols tend to dominate observed changes in the monthly averages of apparent transmission such that the major observed excursions in the record, shown in Figure 3.28, are due to aerosols. The major observable features in Figure 3.28 are the effects of several volcanoes, particularly Agung in 1963, El Chichón in 1982, and Pinatubo in 1991, and an annual oscillation caused primarily by the springtime transport of Asian dust aerosol over the site [*Bodhaine et al.*, 1981]. Figure 3.28 is complete through 2001 and shows that the recovery from the eruption of Mt. Pinatubo required several years. The fact that the Mauna Loa apparent transmission record took several years to recover from Pinatubo is evidence of the sensitivity of the measurement, because it is known from other measurements by CMDL and others that the optical depth of Pinatubo in 1995 was already very low, on the order of 0.005 at 500 nm. *Dutton and Bodhaine* [2001] used the MLO transmission record to deduce the maximum possible change in certain solar radiation budget quantities that could have occurred over the length of the record. The long-term atmospheric transmission was converted to net solar irradiance at MLO by comparison to more recent accurate measurements of surface irradiance and assumptions about the constancy of underlying reflectivity and extraterrestrial solar irradiance. The time series of the deduced net solar irradiance at the level of MLO suggested that the maximum sustained solar radiative forcing from varying atmospheric transmission over Mauna Loa, determined from deduced net solar irradiance changes at 3.4 km above sea level (ASL), was less than –0.3 W m^{-2} over the previous record. In other words, the only linear trend that could have existed in net solar irradiance at the level of Mauna Loa, but would not have been detected, would be between 0 W m^{-2} and –0.075 W m^{-2} per decade, thereby eliminating the possibility of any positive trend. This work provides a longer history and a more accurate determination of actual observed variations in radiative forcing, as related to potential climate change, than any other known directly observed radiation record. With the updated data through the end of 2003, it now appears that the transmission record is stabilizing at a lower level than previously seen or expected suggesting a significantly less clear

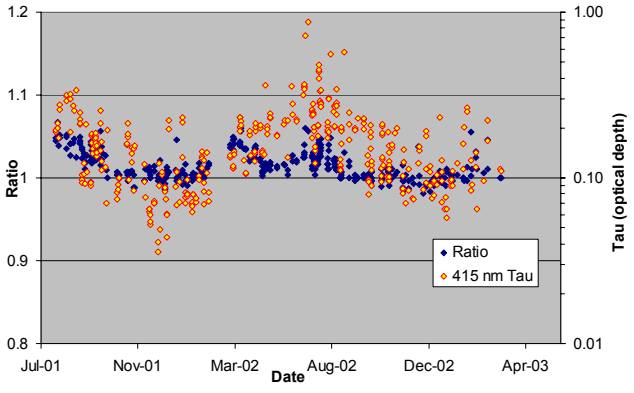

Figure 3.27. Dobson 61/UV5 ratio versus Tau.

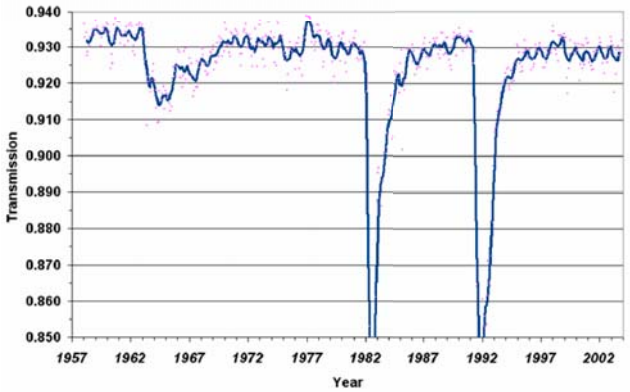

Figure 3.28. Apparent solar transmission observed at Mauna Loa. Monthly averages are shown as points and the solid blue line is running average.

sky transmission than at the beginning of the record. Using the sensitivities determined in the work of *Dutton and Bodhaine* [2001] this results in a solar irradiance decrease of nearly 1 W m^{-2} since the last time such stable conditions existed over the preceding 40 years, but the sustained decrease was not evident until the most recent years because of preceding volcanic anomalies.

Long-Term Cloud Variations Derived From Solar Irradiances

Total solar irradiance observations have been made at the four CMDL observatories since 1976 using single pyranometers that measure the combined direct and diffuse downwelling solar irradiance. Solar irradiance varies with several factors, several of which are components of the atmosphere, such as clouds, aerosols, and various absorbing gases. While the calibration of the pyranometers has been maintained by the best available and internationally recommended methods, sufficient uncertainty exists in the results that make the direct detection of small but potentially climatic significant variations in the atmosphere difficult to impossible. The potential for detection of atmospheric variations can be enhanced by isolating the contributions of single atmospheric components and then comparing pyranometer observations with and without that component included. This permits relative observations of the effect of that single component by ratioing the observed irradiances with and without the presence of that component and, thereby, avoiding the problems associated with the absolute calibration of the pyranometer. In work described by *Dutton et al.* [2004] this approach was used to investigate the long-term variations of the relative contribution of clouds to variations in solar irradiance by determining the relative solar transmission of clouds as the ratio of solar radiances in the presence of clouds to the observed irradiances in clear skies. The CMDL data series was particularly well suited for this study because of its high-time resolution of 1 to 3 minutes. No other data sets with this temporal resolution and length of record are known to exist. The analysis detailed in the work of *Dutton et al*. [2004] gives a time series of both effective cloud transmission and frequency of cloud occurrence where cloud occurrence is defined as when cloudiness is detected in the solar irradiance signal of a pyranometer. The pyranometer signal is sensitive to clouds around and near the sun and in about the upper 80% of the upward viewing hemisphere. The time series of annual cloud transmission and frequency for the four primary CMDL baseline observatories are given in Figures 3.29 and 3.30, respectively. An oscillation in the cloud transmission and occurrence is seen at SPO and an upward trend in cloudiness frequency is seen at BRW.

Polar Aerosol Characterizations

During 2002 and 2003, programs initiated during 2000 to monitor AOD at BRW and SPO continued. An overview of these programs is given in the previous Summary Report [*King et al*., 2002] with details contained in the work of *Stone* [2002]. Using time series of spectral AOD from these and other polar sites, values of Ångström exponent å were derived. This parameter relates qualitatively to the size of aerosol particles. Quantitatively, it is derived from the slope of spectral AOD when plotted on a log-log scale. Steep, negative slopes are indicative of smaller particles. Here, values of å are evaluated for wavelength pairs (λ_1, λ_2) using the relationship:

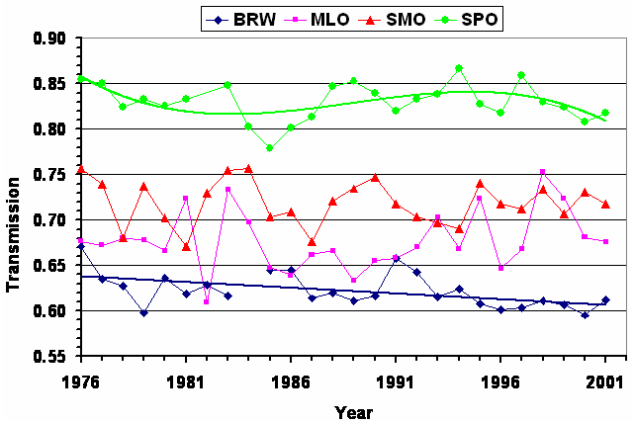

Figure 3.29. Annual average cloud transmission at the four CMDL observatories as described by *Dutton et al*. [2004].

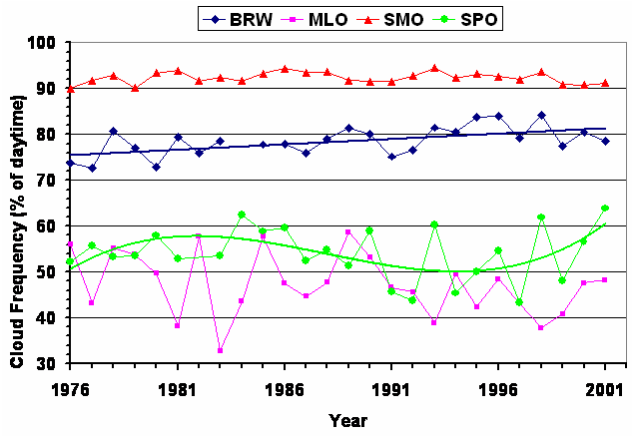

Figure 3.30. Annual average frequency of cloud occurrence at the four CMDL observatories derived as described by *Dutton et al*. [2004].

$$å(\lambda_1, \lambda_2) = -\log10(\tau(\lambda_1)/\tau(\lambda_2))/\log10(\lambda_1/\lambda_2) \qquad (1)$$

where $\lambda_1 < \lambda_2$ and $\tau(\lambda_1)$ and $\tau(\lambda_2)$ are the AODs at the respective wavelengths.

In general, the values of $å(\lambda_1, \lambda_2)$ for different wavelength pairs are approximately equal for a given aerosol type. That is, size spectra can be described by a power law relationship. Figure 3.31 shows how spectral signatures tend to be linear on a log-log plot of AOD versus wavelength. The figure shows spectral AOD plotted for several aerosol types. These are referenced to an analysis made for a thin cirrus cloud observed over BRW. Values vary by an order of magnitude and certain types show spectral behavior that deviates from the assumed Ångström power law. Note also that the slopes of the respective curves (from the bottom to the top) tend to decrease in magnitude as AOD increases, suggesting that the presence of larger particles leads to enhanced extinction. Caution must be used in interpreting derived values of $å(\lambda_1, \lambda_2)$; however, because some size distributions do not follow an Ångström size distribution and even may be

multimodal. For example, aged volcanic aerosols are typically bimodal, having a large-particle mode and a small-particle mode of higher concentration [*Stone et al*., 1993]. Values of å should be derived by a single fit over the entire spectral range of observation only when the size distribution is believed to be very similar to the Ångström distribution. On the other hand, using equation (1) to determine å is also prone to error because one or both of the AOD values used in the calculation may be in error. This is particularly true when optical depths are very small and corrections for gaseous absorption and/or Rayleigh scattering are not made accurately. Nevertheless, when used appropriately Ångström exponents indicate particle size and something can be learned about polar aerosol characterizations.

The large differences observed in polar records of AOD highlight the importance of assimilating similar data from other sites to better characterize aerosols spatially and temporally. Figure 3.31 and Figure 3.32 illustrate the potential value of assimilating data from various sites to gain a perspective of how aerosols differ from pole to pole and, in the case of Antarctica, from the coast to the high plateau. Using ancillary data, primarily trajectory analyses [*Harris and Kahl*, 1994], source regions of different aerosols can be identified and different species can be classified according to their spectral signatures. Figure 3.32 shows this clearly.

An attempt was made to classify the aerosol types presented in Figure 3.31 by plotting values of Ångström exponent for the channel pair 412/675 nm as a function of the 500 nm AOD, AOD(500). The visible range is selected as the most important in terms of direct radiative forcing. Interestingly, there is a nonlinear relationship between relative size and the magnitude of the optical depth, noting again that $å(\lambda_1, \lambda_2)$ is inversely proportional to particle size. Also, aerosol types tend to cluster along a best fit of the data indicated by the dashed regression curve in Figure 3.32.

The reference cirrus cloud is composed of large ice crystals and thus has small values of å. Cirrus clouds vary optically, however, so the cluster is drawn out over a range of optical depths. In this example, Asian dust appears to be thicker optically than Arctic haze and is composed of larger particles. Both show nonlinear behavior with greater optical depths being associated with larger particle sizes. This functionality may be related to hygroscopic particle growth that varies with relative humidity. There is observational evidence that Ångström exponents decrease in value as particles grow hygroscopically [*Carrico et al.,* 1998].

Under pristine conditions, represented by the SPO January cluster (Spole) and the summertime background for BRW (SumBG), size spectra appear highly variable but have a very narrow range of optical depths. It is possible that this feature is an artifact of measurement because the analyses are based on data collected near the lower limit of the photometers' sensitivity. Also, because NO_2 and O_3 absorb radiation at 412 nm and 675 nm, respectively, and depending on their concentrations, estimates of å(412/675) are subject to greater uncertainty when values of AOD are small. The column amounts of these gases are not always measured accurately. The cluster means are probably valid, however, and show that clean polar air contains a mix of very small particles. Average summer conditions at Terra Nova Bay, Antarctica, and during spring at Ny-Ålesund, Norway, are similar to those during spring at BRW (SprBG) as might be

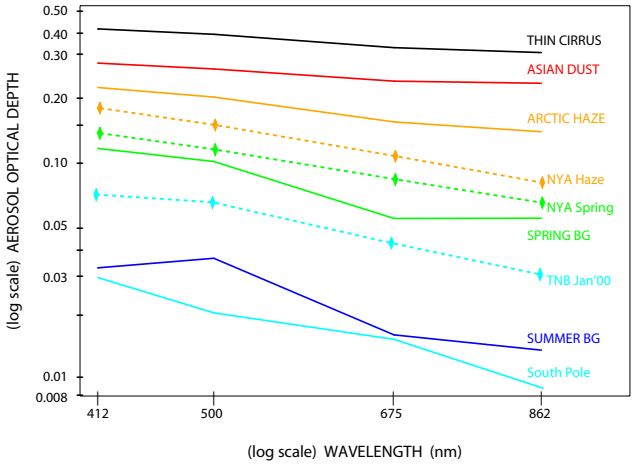

Figure 3.31. Mean aerosol optical depth as a function of wavelength for different aerosol types compared with that of a thin cirrus cloud. Data were collected at BRW, with the exception of those curves labeled South Pole, TNB, and NYA, which represent conditions at the South Pole and Terra Nova Bay, Antarctica, during January and typical spring and hazy conditions at Ny Ålesund, Norway.

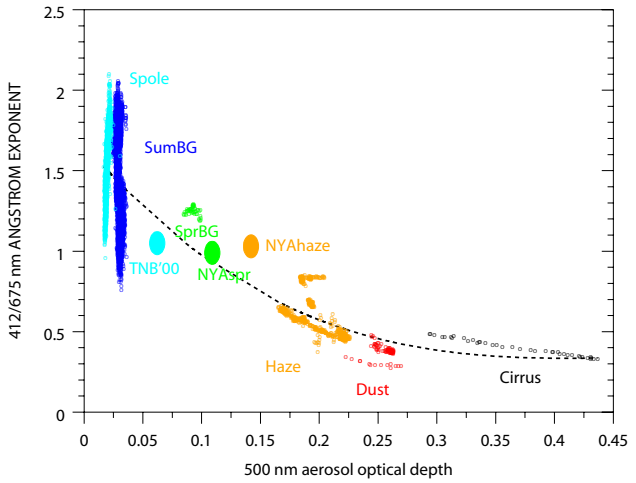

Figure 3.32. Plot of Ångström exponents, å(412/675) as a function of 500 nm aerosol optical depth, AOD(500). Clusters of points correspond to 1-minute data used to determine the mean spectral AODs shown in Figure 3.31 with the exception of points labeled TNB'00, NYAspr, and NYAhaze for which high-resolution data were not available. The dashed curve is a best fit of all the data showing that AOD(500) increases for decreasing values of å(412/675) or as particle size increases.

expected. All three sites are at sea level, are at similar latitudes, and are influenced by marine aerosols. In contrast, SPO during the summer is an extremely clean site because it is high on a plateau and far from sources of (larger) sea-salt aerosols. Occasionally during summer the BRW atmosphere is nearly as clear optically as at SPO, but in general, the Arctic is not as pristine a region as is often thought. Turbid conditions often perturb the radiation balance of the region as evidenced by the

signatures of "haze" and "dust" shown in Figure 3.31. A case study of how an Asian dust event impacts the surface radiation balance at an Arctic site is presented in the next section.

The analysis summarized in Figure 3.32 is intriguing and suggests that with a much larger statistical ensemble of observations a bipolar characterization of aerosols (and possibly thin clouds) could be synthesized. Taking this a step further, utilizing coincident in situ data to determine chemical and physical properties of the particles should provide a basis for parameterizing aerosols (and thin clouds) in regional climate models. Alternatively, using an inversion scheme [*King et al.,* 1978] to infer size spectra and Mie theory to calculate optical properties of these spectra, it may be possible to develop representative microphysical models defined by the key radiative properties needed to estimate radiative forcing. The work of *Ogren* [1995] lists the properties of aerosols that are required for climate studies.

Current Status of Polar Aerosol Studies

The analysis presented in Figures 3.31 and 3.32, though based on a limited data set, demonstrates the value of using spectral AOD data for characterizing diverse species of aerosols that impact polar radiation budgets. Ultimately, it is the radiative forcing by aerosols that is of primary concern to climatologists. Theoretical calculations suggest that polar regions are peculiar in this regard. The work of *Cacciari et al.* [2000], for instance, shows aerosol radiative forcing can change sign depending on chemical species, surface properties, and solar geometry. Particle size is another critical property that varies hygroscopically with relative humidity. Unfortunately, surface measurements may be inadequate for high-latitude aerosol studies because polar atmospheres are highly stratified, mixing is suppressed, and aerosols often reside in layers above the surface-based temperature inversion. Only by combining (columnar) AOD data with in situ surface and airborne observations can advancements in our understanding of aerosol radiative forcing be made. As the following sections reveal, the quantification of the radiative impacts of aerosols in the Arctic using empirical data is only beginning. In the future, such investigations must be correlated with dynamical analyses and cloud observations as well if the indirect effects of aerosols are to be determined. Even slight changes in cloud microphysical or physical properties resulting from interactions with aerosols are likely to perturb the climate of the high-latitude regions because clouds profoundly impact the radiation balance there [*Stone*, 1993, 1997; *Stone and Kahl*, 1991]. It is in recognition of these uncertainties that the Scientific Committee in Antarctic Research and the Intergovernmental Panel on Climate Change (IPCC) recommend upgrading observational networks to include sustained measurements of aerosol optical properties in polar regions. The Aerosol Robotics Network (AERONET) [*Holben et al.,* 2001] is only beginning to deploy its standard photometers to polar sites, and satellite data are not yet useful at high latitudes for deriving aerosol properties. Therefore, additional steps are recommended to meet the scientific goal of producing a global aerosol climatology. Clearly, a sustained effort to obtain continuous measurements of spectral AOD at a number of high-latitude sites is warranted.

Proposed International Polar AOD Network and Archive

In October 2003 a workshop was convened in Bologna, Italy, to establish closer ties among countries having AOD monitoring programs in the Arctic and in the Antarctic. The Italian Program for Antarctic Research is coordinating this effort and will establish a Web-based archive of all available polar AOD data (historical and ongoing). The polar network is essentially in place, although enhancements are needed in the Arctic where few monitoring sites are presently active. These enhancements may be possible under the NOAA Arctic Research Office sponsored program "A Study of Environmental Change in the Arctic" (SEARCH) (http://psc.apl.washington.edu/search/). Through SEARCH, CMDL will deploy an eight-channel sunphotometer system to Alert, in the Canadian Arctic (82.5^{o}N), in the summer of 2004. Also, initial plans were laid for a similar deployment to a coastal Siberian site in collaboration with the Arctic and Antarctic Research Institute, St. Petersburg, Russian Federation. In conjunction with these systems there will be a full complement of surface radiation monitoring instrumentation to meet BSRN standards [*Ohmura et al.,* 1998]. Once established, these and existing programs will provide the means to monitor and access the radiative impacts of aerosols over spatial scales suitable for meaningful climate studies on a pan-Arctic basis with similar capability in Antarctica.

Incursions and Impact of Asian Dust Over Northern Alaska

Atmospheric aerosols affect the Earth's radiation budget both directly through interactions with solar and terrestrial radiation and indirectly as cloud condensation and ice nuclei. Because polar atmospheres are generally very clean, even small increases in aerosol concentrations can perturb the radiometric structure of the atmosphere and thus the surface energy balance. It is, therefore, important to investigate the natural and possible anthropogenic effects of aerosols that are frequently transported into the Arctic Basin, particularly during late winter and spring.

April 2002 Dust Event at Barrow

During spring 2002 dust storms occurring in the Gobi Desert region of Mongolia lofted huge amounts of dust into the atmosphere and was subsequently transported eastward in a broad plume that reached the continental United States. Some of this dust was carried aloft by upper level winds with a trajectory that passed over BRW. Like Arctic haze [*Barrie et al.,* 1981; *Dutton et al*., 1984, 1989; *Bodhaine and Dutton*, 1993; *Harris and Kahl*, 1994], incursions of Asian dust have occurred in the Arctic for many years [*Shaw*, 1983; *Griffin et al*., 2002; *Van Curen and Cahill*, 2002; *Bory et al*., 2003], and, yet, few investigations have focused on quantifying their radiative effect [*Blanchet*, 1989; *Hegg et al*., 1996]. With the current complement of instrumentation at BRW, it is now possible to track these events, monitor their physical properties, and derive or infer something about their optical and microphysical characteristics. For instance, the addition of a tracking sunphotometer system in 2000 (*Stone* [2002] and the previous section of this report) has enabled quantification of turbidity and determination of spectral signatures in AOD. In situ aerosol sampling at the surface can be used to investigate light scattering by aerosol particles from

which fundamental optical properties can be derived [*Ogren,* 1995]. Particle analyses are used to determine chemical composition to fingerprint source regions. On this basis, the work of *Quinn et al.,* (see "Results from Simultaneously Measured Aerosol Chemical and Optical Properties at Barrow, Alaska" on page 161 of this report) suggests that the frequency and intensity of Asian dust events have increased in recent years contributing to an observed increase in spring dust concentrations at Barrow. When not cloudy, these dust layers are clearly visible in lidar profiles provided by the DOE ARM program from a facility near BRW. Also, using back trajectory analyses [*Harris and Kahl*, 1994] pathways from distinct source regions are identified with some confidence. Finally, the suite of radiometers at the station yield an accurate time series of flux measurements from which the radiative forcing by aerosols are estimated.

An assimilation of measurements and model results are employed to characterize the radiative properties associated with intrusions of Asian dust observed at BRW during April 2002. As discussed in the previous section, Ångström exponents derived from spectral measurements were used to estimate relative size of the particles. The in situ (surface) measurements of scattering properties during early April show several episodes when Ångström exponents dip below 1.0 compared with a 25-year median value of ~1.8. This indicates the presence of large particles in the mix. Distinct layering of turbid layers in the lidar profiles, and corresponding trajectory analyses, all provide corroborating evidence that Asian dust emanating from the Gobi Desert had reached the western Arctic. The transport time was about 6-8 days on average, with the most pronounced layering observed between about 2000 and 6000-m altitude. Obviously, some of this material either fell or was mixed to the surface during the course of the events as evidenced in Figure 3.33.

In Figure 3.33 the time series of AOD shows scattering and derived Ångström exponents for the period of interest. The decrease in Ångström exponents are correlated with the enhanced AOD. Note that AOD is only measured during day time and when there are no clouds present, thus there are gaps in the time series.

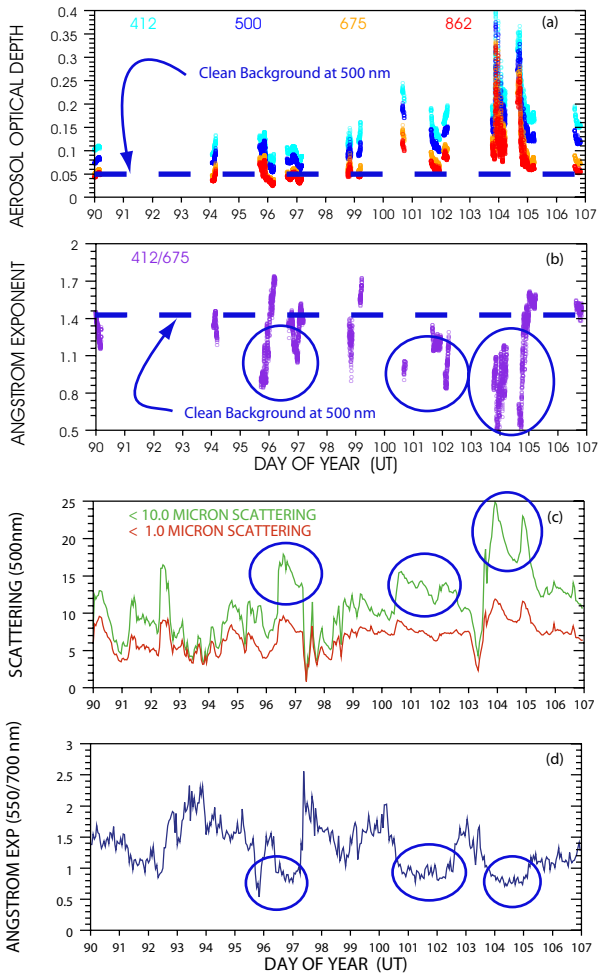

Figure 3.33. Time series for early April 2002 at BRW showing at top (a) spectral AOD derived from the four-channel sunphotometer, (b) corresponding Ångström exponents for the 412/675 nm pair of wavelengths, (c) light scattering coefficients for particle diameters <10 micron (solid) and submicron (dashed), and (d) the derived Ångström exponents for the 550/700 pair of nephelometer wavelengths. Circles indicate periods when Ångström exponents dropped significantly below long-term median values. During the period of peak aerosol loading (days 104-105), a large pulse of supermicron-sized particles reached the surface and filled a deep layer of the atmosphere.

Direct Radiative Forcing by Asian Dust: Measured and Simulated

Extinction by aerosols in the atmosphere is greatest in the visible portion of the solar spectrum (Figure 3.33). Therefore, the broadband direct beam irradiance reaching the surface diminishes significantly with increasing turbidity. In turn, the total flux at the surface decreases despite some additional diffuse light from forward scattering by the particles. At BRW each of these components is measured along with the reflected (upwelling) shortwave irradiance (SW). It is straightforward to calculate the net SW flux (netSW = SWdown – SWup) at the surface and evaluate changes as a function of optical depth. When turbid conditions are compared with pristine periods, a measure of the direct radiative forcing by the intervening aerosol layers can be estimated. This quantity will be referred to as Direct Aerosol Radiative Forcing (DARF) as pertaining to the surface netSW radiation.

Similarly, radiative transfer theory can be used to calculate DARF if a suitable model is selected and the input variables are known with sufficient accuracy. Through our collaboration with the Air Force Research Laboratory (AFRL)/Space Vehicles Directorate, MODTRAN 4, Version 3 [*Anderson et al.,* 2000] was used to simulate the effects of aerosol layers having similar optical properties to those observed. This was done over a range of optical depths to allow a comparison of model and empirical results. The analysis presented is a first attempt at such a "closure experiment" for an Arctic location characterized by high surface albedo (82-84%) and low solar angles.

Closure Experiment

An outline of the procedure follows:

- Measure columnar spectral aerosol optical depth (AOD).
- Using the *King et al.* [1978] inversion scheme, initialize for observed spectral AOD and, assuming an index of refraction for (desert) dust, infer the aerosol size distribution.

- Using Mie theory, initialize a code for the inferred size distribution to calculate optical properties of the aerosol for the relevant spectrum (0.28 - 3.0 microns).
- Initialize MODTRAN, simulating the aerosol layer as a cloud at the observed (from lidar) altitude; run for a range of optical depths and solar zenith angles to arrive at the following quantities:
  - (calculated) spectral distribution of solar energy from the surface to 100-km altitude using the DISORT- 4-stream multiple scattering mode with 17 spectral bands
  - (derived) upward and downward component fluxes at each of 69 layers
  - (derived) heating rate profiles for surface to top of the atmosphere
  - (derived) DARF as a function of solar zenith angle for comparison with empirical results

From the spectral AOD time series (Figure 3.33a) mean values corresponding to dust events (Figure 3.33) were computed and used to infer a size distribution. The index of refraction, m = 1.51 - i0.009, was estimated on the basis of empirically determined properties of dust [*Sokilik et al.,* 1993]. The inferred distribution is shown in Figure 3.34 compared with ones representing Arctic haze and typical clean background conditions.

Note that both the haze and dust spectra are bimodal with the dust distribution revealing a larger total number of supermicron sized particles than the haze. This is consistent with the relationship shown in Figure 3.34, denoted as "dust" and "haze".

Once all calculations were made, a tabulation and graphical displays of the results were produced. Figure 3.35 compares the empirical and model results for three distinct solar zenith angles. These results illustrate the significant variation in DARF over a typical diurnal cycle for April at BRW. Direct Aerosol Radiative Forcing (DARF) is defined simply as the change in netSW radiation per unit optical depth, i.e., the slope of each regression. Negative slopes indicate that the surface tends to cool when dust is present in the atmosphere above BRW during the spring. Table 3.13 compares DARF-derived measurements (observed) to model estimates for three zenith angles.

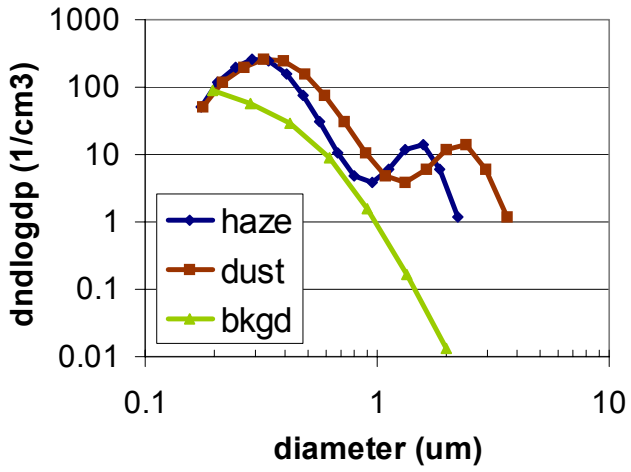

Figure 3.34. Size spectra inferred using the *King et al.* [1978] inversion algorithm initialized for observed background, hazy, and dusty atmospheres at BRW.

Results and Conclusions

There is a tendency toward less cooling as the sun gets close to the horizon (large zenith angles). This is probably due to enhanced multiple reflections that permit greater absorption by the surface and within the intervening atmosphere. Unfortunately, the data are very limited both in terms of quantity and in range of optical depth. Without having a larger statistical ensemble to analyze, little can be said about the differences and bias between modeled and empirical results indicated in Table 3.13. There are sufficient data, however, to conclude that MODTRAN simulates the observations reasonably well overall, matching observed features in both magnitude and sensitivity to zenith angle. In turn, the theory tends to corroborate the empirical results giving credence to the use of surface radiation measurements for evaluating the climatic impact of aerosols in polar regions. In this particular case, by scaling the results to account for changing zenith angles for a given AOD, it is possible to estimate the net direct radiative forcing by aerosols on a 24-hour basis. For a modest AOD(500) of 0.15 this amounts to about 5 W m^{-2}, a cooling effect that is greater than the warming estimated from

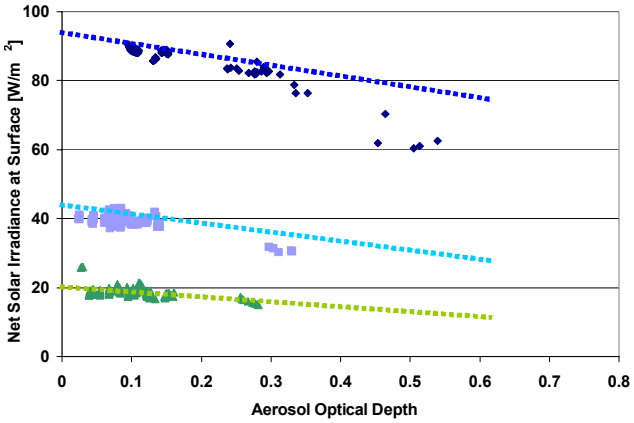

Figure 3.35. Comparison of measured and simulated surface net solar (shortwave) irradiance as a function of visible (500 nm) aerosol optical depth during an Asian Dust event at BRW, April 2002. Symbols represent measurements and dashed lines the results from MODTRAN 4 fitted using linear regression for selected zenith angles as indicated. The enclosed (suspect) points were not used in the 62° analysis for purposes of computing DARF empirically. Results are summarized in Table 3.13.

Table 3.13. Direct Aerosol Radiative Forcing (DARF) at the Surface for the April 2002 Dust Episode at Barrow, Alaska, as a Function of Solar Zenith Angle and for Observed and Modeled Results

	81°	75°	62°
Observed	-16.1	-30.2	-37.8
Modeled	-14.4	-25.4	-30.9

Units are W m^{-2} unit AOD^{-1}

doubling CO_2. Even though these are episodic events that occur mainly in late winter through spring, this is not an insignificant effect. Should the Arctic atmosphere become more turbid [*Quinn et al*., 2002; also see "Results from Simultaneously Measured Aerosol Chemical and Optical Properties at Barrow, Alaska" on page 161 of this report), projections of enhanced warming in the Arctic [*IPCC,* 2001] may be overestimated. Until more data are assimilated, however, this is mere conjecture.

In the future, extensive work must be done to analyze data for a variety of aerosol types, surface conditions, and solar geometries. More absorbing aerosols will lead to less cooling and possibly even heating over bright snow or sea ice, while increasing the areal coverage of low albedo surfaces such as open water or tundra might promote greater cooling than indicated from this analysis. Repeating such closure experiments as the data become available will give us greater confidence in the model as well. The use of MODTRAN to further assess sensitivities to changing surface albedo and to calculate top-of-the-atmosphere forcing by aerosols is promising. These investigations will lead to meaningful climate assessments for polar regions as well as providing essential data for validating satellite retrievals of aerosol properties and their effects.

Even more problematic than these experiments is determining the indirect effects of aerosols in the polar atmosphere. Aerosol interactions with clouds and their influence on cloud physical and microphysical properties are largely unknown. Clouds have a much more profound effect on the surface-atmosphere radiative balance at high latitudes than do aerosols [*Stone and Kahl*, 1991; *Stone*, 1993, 1997]. It is very clear that directly, and more likely indirectly, aerosols play a key role in the energy budget of polar regions that needs to be understood and quantified. In turn, these processes have global implications through feedbacks, particularly those related to observed changes in albedo caused by melting sea ice [*Curry et al.*, 1995] and reduced snow cover [*Stone, et al.,* 2002].

Mobile Observing System (MOS) for Polar Surface Characterizations and Remote Sensing Validations

Historical perspective. Historically, there have been problems associated with measuring snow albedo at the GMCC/CMDL polar observatories at SPO and BRW. This was first documented in the work of *Dutton et al.* [1989] which revealed non-physical, oscillating values of albedo derived as the ratio of upwelling to downwelling solar irradiance at SPO. In addition to the leveling issues addressed in that report, the behavior stems from the surface not being flat but rather has prominent linear or sometimes cross-hatched features called sastrugi. When illuminated by the sun, these sastrugi appear relatively bright or dark depending on the solar geometry relative to their orientation. While the effect tends to average out over a daily cycle, instantaneous values are suspect even after the "removal of erroneous diurnal cycles," especially for the validation of satellite-derived albedo. While the literature has many references to the visible properties of snow as pertaining to surface roughness [*Warren et al*., 1998; *Brandt and Warren*, 1996], the thermal structure was not carefully examined nor were the effects of differential heating considered for remote sensing applications. It was speculated that the thermal structure of a sastrugi field would affect the complicated geometry of view-angle, solar zenith, and sastrugi orientation such that any point/spot measurement of snow "skin" temperature would be prone to error. Again, this is problematic when validating satellite retrievals [*Key et al.,* 1997b]. While satellites have great potential for monitoring albedo and surface temperature on the global scale needed for climate studies, there remains a reliance on "groundtruth" measurements for validation. The Antarctic Plateau is a particularly attractive target; an experiment was launched in January 1995 to characterize the surface reflectivity and temperature variations at SPO.

Need to go mobile. Making repeated point measurements of snow temperature and reflectivity rapidly over suitable spatial scales was not possible; therefore, a mobile platform was designed and fabricated. An infrared thermometer (IRT) became the backbone of the system. It mounts on a boom and points directly at the surface to measure thermal (8-14 microns) radiation from a spot approximately 25 cm in diameter. If the surface emissivity is known, the actual skin temperature can be accurately determined from the upwelling radiance at whatever time step is desired. While there is some debate over the true emissivity of snow, and of course it varies slightly, 0.99 was used because snow is nearly "black" in the infrared. To map the surface in good detail, 1-second data are sufficient. Other components of the system include upward and downward viewing LiCor silicon pyranometers from which albedo in the 0.4-1.1 micon range can be derived, an aspirated temperature probe to measure ambient air temperature at boom height (1.5 m), and a Global Positioning System (GPS) device to determine position and elevation along the track and to synchronize timing of the data acquisition system (DAS). The datalogger is onboard and the entire system is powered by rechargeable batteries, generated by the snowmobile used to haul it, or by line power when operated in a stationary mode. IRT calibrations are extremely important and are made both in the laboratory and in the field using a set of blackbody targets that are well characterized. While no details will be given here, the results were consistent and show the IRT to be stable with <0.1°C accuracy under ideal conditions. Accounting for ambient influences, field measurements should be accurate to within 0.3°C. The instruments mount on a boom supported by a box containing the battery pack and DAS. This is secured to a specially designed sled and then hitched to a snowmobile, or in some cases manually hauled. The components are also detachable for more portable applications such as making observations from towers. All components except the snowmobile can be broken down and shipped virtually anywhere. The total weight is <200 kg including shipping materials. The system is pictured in Figure 3.36 prior to deployment in Antarctica for a 2002/2003 campaign described in a later section.

In Figure 3.36 the labels identify key components of the system. The IRT (KT19) and two downward-facing LiCor pyranometers are mounted on the right-hand side (if one is facing forward), and the Temperature probe (T amb), and GPS are mounted on the left-hand side. A LiCor is also mounted on top of a pedestal facing upward. Inside the box are the batteries and DAS. The "boom LiCor" is customized to view a spot that coincides and is slightly larger than the KT19 field of view and is designed for cross-correlations that are discussed next.

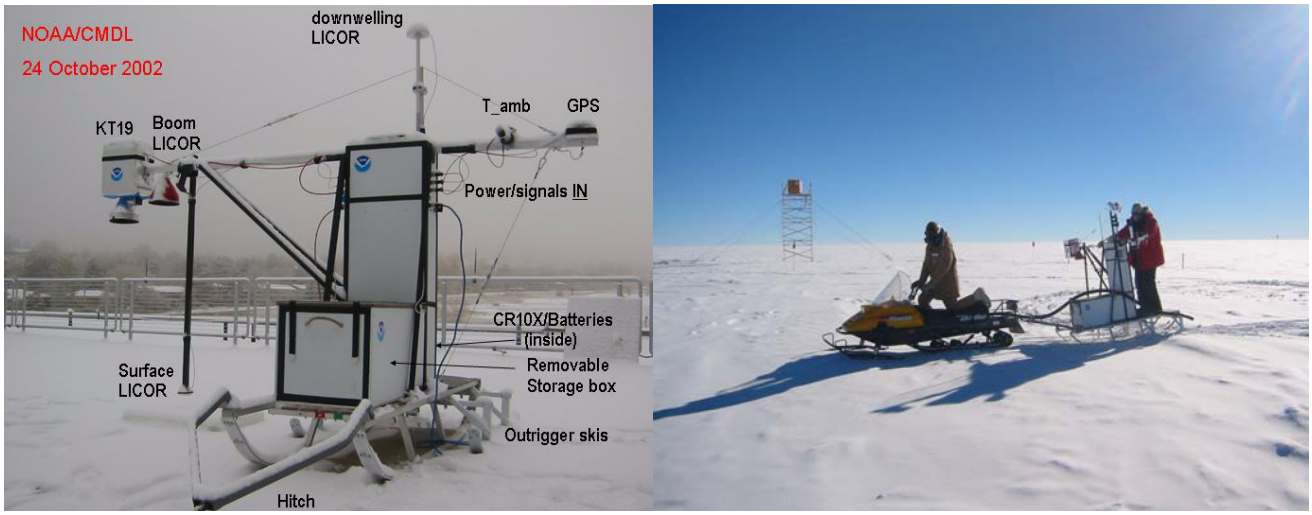

Figure 3.36. Left, the CMDL Mobile Observing System and its components as configured in 2002. Right, the system in operation during austral summer 2002/2003 at Dome Concordia, Antarctica.

Field campaigns. The MOS prototype, developed in 1994, was first used at SPO during a brief campaign to evaluate performance and collect transect data to validate the Advanced Very High Resolution Radiometer (AVHRR)-derived snow temperatures. Operating in the clean air sector there required manual hauling so the track was limited to 1500 m, an equilateral triangle 500 m on a side. At nadir the AVHRR footprint is 1 km, so if geographically located at a coincident location (geolocated) with the track, there was a good match in scale. Unfortunately, no satellite overpasses were available to exactly coincide with transects, but the limited analysis at least provided proof of concept. Figure 3.37 shows the results for 24 January 1995.

Although the timing and the geographical location was not exact, overall the agreement between AVHRR and "groundtruth" is good. The increase in AVHRR temperatures after 0430 in Figure 3.37 is captured by the transect data reasonably well, and the retrieval at 0615 (between the first and second transects) is within the uncertainty of the averaged IRT data spanning this overpass. This suggests that the retrieval algorithm [*Key et al.,* 1997a] at the time produced very good results under the pristine and very cold, dry conditions over the plateau. Note also that the surface-based temperature inversion was extreme on this day (a record cold day) and the air temperature at about 1.5 m was >3°C warmer than the surface.

More importantly, the first detailed thermal scans of a sastrugi fields with corresponding reflectivity data were obtained. These revealed distinct thermal structure in the snow pack and significant variability that correlated nicely with the linear features that MOS traversed. The data corroborated the hypothesis that significant differential heating occurs under conditions of varying solar illumination. In the case shown in Figure 3.37 the skin temperature varied by > ±1°C as evidenced by the lower time series.

In 1998 MOS was used during the spring at the Surface Heat Budget of the Arctic (SHEBA) encampment drifting in the Chukchi Sea north of Alaska [*Uttal et al.,* 2002]. There it was

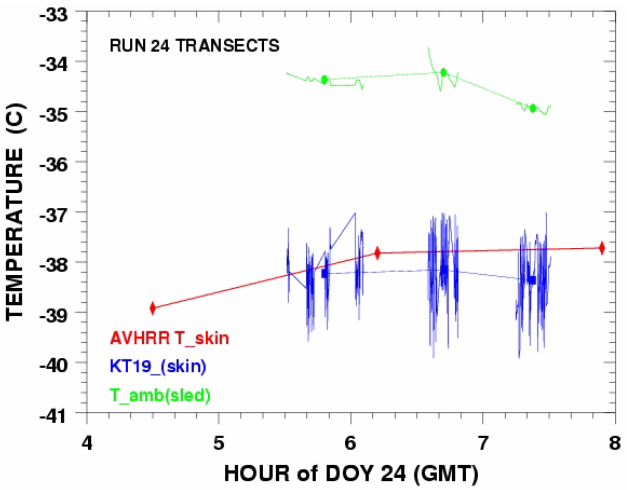

Figure 3.37. An example of how the NOAA CMDL Mobile Observing System (MOS) can be used to validate satellite-derived snow temperatures over the Antarctic Plateau. As indicated, the diamonds are the AVHRR retrievals. MOS skin temperatures (lower) and air temperatures (upper) are shown as time series of 1-second values measured over three transects around a 1500-m triangular track in the clean air sector at SPO. The AVHRR retrievals were provided by NOAA NESDIS, Madison, Wisconsin.

towed behind a snowmobile around a 2.6 km triangular track adjacent to one of the flux stations. Details of the setup are described in the work of *Maslanik et al*. [1999], which also gives an overview of the kind of analyses that were made. *Pinto et al.* [1999, 2003] exploited the stationary mode of operation to investigate the energy budget of refreezing leads which further demonstrated the versatility and convenience of the rapid deployment of the system. The SHEBA data have not yet been fully exploited for satellite validations.

Because of success achieved during these early campaigns, CMDL was asked to participate in the validation of the

Atmospheric Infrared Sounder (AIRS) onboard the Aqua satellite launched by NASA in May 2002. Aqua is in polar orbit and its objective is climate studies, including retrievals of surface and atmospheric temperatures, and humidity. AIRS monitors these variables on a global scale, but had to be validated first. Dome Concordia on the Antarctic Plateau was chosen as an excellent target because intervening atmospheric effects are minimal. Nearly unobstructed views of the flat, uniform surface are possible, and water vapor and aerosol contents are extremely low. Concordia summit (3280 m, 75ºS) is a station operated under the Italian and French Antarctic programs that provided the necessary logistical support. Aqua passes nearly overhead at Concordia at least once a day, making it an ideal validation site. The first campaign took place from December 2002 to January 2003.

The experiment involved making precise surface temperature measurements using a Polar Atmospheric Emitted Radiance Interferometer (PAERI) operated by the University of Idaho. MOS was used primarily to quantify variations in snow temperature on a spatial scale that approximated the AIRS footprint at nadir (about 13 km). The system became known as the AIRS Mobile Observing System (AMOS) (Figure. 3.36). Again, transects were run around triangular tracks several kilometers in length at times coincident with overpasses of the satellite. At a 1-second sampling rate, AMOS was able to map the detailed thermal and reflective properties of the snow surface and with the appropriate calibration integrated the data to produce accurate pixel-scale temperatures for comparisons with AIRS and PAERI retrievals. The preliminary results demonstrated the validity of this approach and corroborated the earlier findings from the 1995 SPO campaign.

One fascinating result illustrated in Figure 3.38 shows how dramatically snow temperatures can vary over short distances. As mentioned earlier, this is due to heating and/or cooling effects that result when the sun differentially illuminates snow features called sastrugi. Uncertainties in AIRS retrievals which resulted, and that may be due to these effects, were further investigated during the 2003-2004 campaign at Dome Concordia. The validation results should be completed and published in 2005.

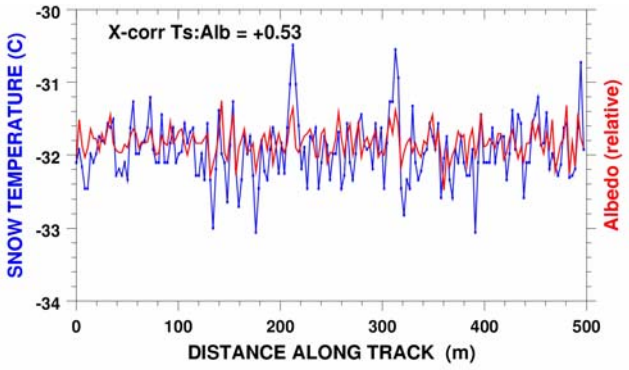

Figure 3.38. The 1-second snow temperatures taken by AMOS (left scale) measured along a 500-m section of a 3-km track run on 29 January 2003 and corresponding albedo (right scale, relative units). The two time series are correlated, confirming the close relationship between intensity of illumination and differential heating of the sastrugi. Data were collected during the AIRS validation campaign - Concordia Station, Antarctica.

Conclusions. CMDL developed a mobile system that was a valuable tool for a myriad of applications related to surface energy budget studies in polar regions. Utilizing an IRT in conjunction with solar radiometers and an ambient temperature probe, the thermal and reflective properties of both snow and sea ice surfaces were determined with unprecedented detail. Also, continuous surface scans along transects map the skin temperature and albedo with an accuracy suitable for validating satellite-derived values, an essential step in global scale climate monitoring. In a static mode, the system was used to evaluate the thermal processes associated with refreezing leads in the Central Arctic. In the future the system will to be available for further campaigns, possibly at BRW and on the Greenland Summit, another ideal validation site with considerable value for climate studies.

Western Arctic Meltdown Continues

Trend towards an earlier date of snowmelt. In the work of *Stone et al*. [2002] documentation and an explanation of a trend towards an earlier spring melt season at BRW was given. The following updates that analysis and places it in perspective with broader scale climatic change in the western Arctic. Although 1999, 2000, and 2001 were consecutive years of moderately late snow melt at BRW [*Waple et al*., 2002], the disappearance of snow at the observatory set a record in 2002 for being the earliest in the 62-year record [*Waple and Lawrimore*, 2003]. The 2003 melt date was again early, and as of this writing, the long-term trend reported by *Stone et al*. [2002] is further substantiated. Figure 3.39 shows the updated time series of BRW melt dates following the definitions and procedures described in the aforementioned paper. It is worth reexamining the time series analysis now that the record has been extended by a few years.

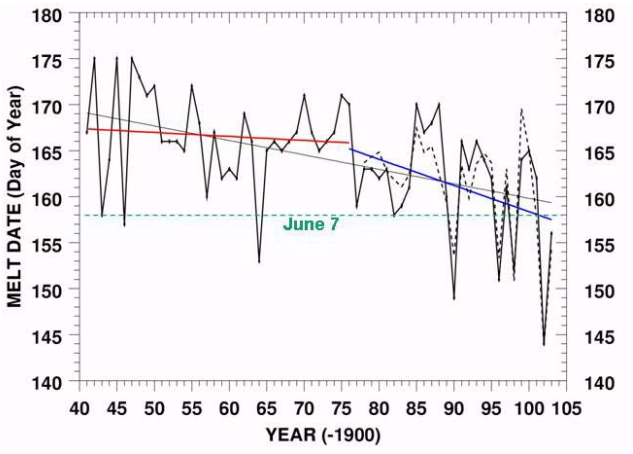

Figure 3.39. Time series of snow melt dates constructed for BRW shows the continuing advance in the snow-free season there. Three linear regressions are plotted: an overall trend from 1941 through 2003 (thin black line), one for all years prior to 1977 (red), and a third beginning in 1977 (blue). Results of a predictive model are also shown (dashed). The time series was compiled from direct snow depth observations, proxy estimates using daily temperature records, and beginning in 1986, from determinations of snow disappearance on the basis of albedo measurements (updated from *Stone et al*. [2002]).

Since the record began in 1941 the overall advance in the date of snow disappearance at BRW is about 10 days (±4.8 days at the 95% confidence level). It is apparent, however, that most of this advance has occurred since the mid-1970s. This is highlighted in the figure by showing regressions before and after 1976. While neither of the regressions show statistical significance because of the large interannual variability that is characteristic, it is very obvious that the recent period shows a marked downturn. Rather than showing a monotonic advance as might be suggested by the 63-year fit (Figure 3.39, solid line), the data suggest a regime change around 1976-1977 with subsequent years having more frequent early melt seasons. In the last 28 years there were five instances of melt occurring before June 7, whereas during the previous 36 years there was only a single event. This shift coincides with regime changes observed in many other indicators of environmental change [*Hare and Mantua*, 2000]. The North Pacific region, including the Aleutian Low pressure center, was prominently affected by this shift. The Aleutian Low became more intense at that time. Much of the variance in the melt season in northern Alaska is attributed to large scale changes in circulation patterns as explained in the work of *Stone et al*. [2002]. For instance, the record early melt of 2002 resulted from abnormal regional weather conditions associated with synoptic patterns and characterized by diminished snow accumulation during winter. This was followed by a warm spring and culminated in a near-record warm May. Weather for 2000 was the opposite, with moderate snowfall, a cool March and April, and one of the coldest May's on record [*Waple et al*., 2002]. These factors are well enough understood that some skill has been achieved in forecasting the date when snow will disappear at BRW. An empirical model, initialized for a set of basic climate variables, was developed at CMDL to predict the melt date at the observatory several weeks prior to the actual event. The dashed curve in Figure 3.39 shows the results to date. The model forecasts the melt date to within ±3.2 days with 90% confidence. The cross correlation of observed and modeled melt dates is 0.89 for the 26-year overlap and improves to 0.92 for the past 15 years. Our understanding of the processes that determine the annual cycle of snow at BRW is corroborated by the success of this model.

Why the flux of heat and moisture into the western Arctic has varied so dramatically in recent decades along with a trend favoring an earlier advent of spring is the topic of much interest. Many broad-scale correlated changes in the Arctic climate system are occurring [*Serreze et al*., 2000]. On a basin-wide scale these appear to be related to a phenomenon referred to as the Arctic Oscillation [*Thompson and Wallace*, 1998].

Diminishing sea ice in the western Arctic Ocean. What appears to determine the climatic state of much of the western Arctic, including the North Slope of Alaska, northeastern Siberia, and the adjacent seas are responses to particular synoptic patterns. The intensities and relative positions of the Aleutian Low and the Beaufort Sea anticyclone that span large regions of the Chuckchi and Beaufort Seas respectively, determine the transport pathways of heat and moisture into the Arctic from the north Pacific.

Profound changes in sea ice extent and concentration have also been documented in the literature [*Maslanik et al*., 1999; *Parkinson et al*., 1999; *Serreze et al*., 2000]. Not only is ice cover on the decline, but the remaining pack appears to be thinning [*Rothrock et al*., 1999]. Utilizing passive microwave data from polar orbiting satellites reveals greater details of the spatial and temporal variations in sea ice. Trends in the western Arctic are especially dramatic. *Belchansky et al*. [2004, Figure 6] present analyses of Arctic sea ice melt onset, freeze onset, and melt season duration, contrasting the pre-1989 and post-1988 periods. The principal feature that emerges is a large region of the eastern Siberian and western Chukchi Seas that is experiencing earlier melt onset and later freeze-up with a resultant increase in the duration of the melt season. This trend is well correlated with the positive phase of the AO since 1989. Following high-index AO winters, melt tends to begin early and persist longer.

Drobot and Anderson (2001) have successfully used microwave radiometry to estimate the onset of snowmelt over sea ice. Using their algorithm, correlations between snowmelt onset in the regions northwest of Alaska and the melt date time series from BRW (Figure 3.39) were computed. The onset of snowmelt over a rather large region shows significant correlation with the timing of snow disappearance at BRW. This result is shown in Figure 3.40.

Figure 3.40 clearly reveals a region of high correlation between snowmelt onset over sea ice and the final disappearance of snow over the North Slope (as represented by BRW melt dates). This suggests that the processes that determine the annual snow cycle

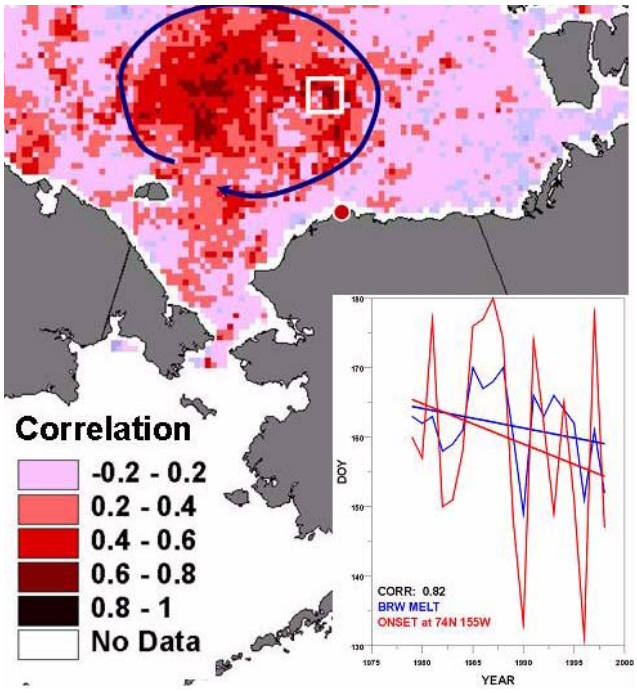

Figure 3.40. Map showing how the onset date of snowmelt over sea ice in the western Arctic correlates with the date of snowmelt at BRW. Onset time series of individual (25 km^2) pixels were cross-correlated with the BRW snowmelt record (Figure 1), and color-coded according to derived coefficients (analysis provided by The National Academies, Washington, D.C.). The inset shows an example of one analysis for a single pixel located due north of BRW (centered within the white square).

over land affect the timing of melt within the region encircled in the figure and possibly that the actual timing of the melt over subarctic land areas can moderate the cycle of sea ice melt. This region is well aligned with that shown in the work of *Belchansky et al*. [2004, Figure 6] to have experienced the greatest increase in duration of the melt season over the last 15 years. It happens to coincide with the position of the BSA as well, which dynamically drives the Beaufort Gyre (ice motion). Previous analyses show that early melt dates at BRW tend to occur during years when the BSA is weak or virtually absent during the spring [*Stone et al*. 2002, Figure 6]. A breakdown of this Arctic high permits the advection of warm air from the north Pacific, driven by the Aleutian low. This moist air increases cloudiness, which enhances the net radiation reaching the surface through thermal emissions [*Stone*, 1997]. Thus the snow is preconditioned early in the season and melt can occur earlier and at an accelerated rate once initiated, typically during the peak of the solar cycle. Further acceleration of snowmelt is likely as air flowing over the vast areas of warmed tundra to the south advects over the sea ice.

Consequences and future studies. The independent records indicate a long-term advance in spring snowmelt over northern Alaska with a correlated advance in the date of melt onset at sea. From the microwave analyses it appears that changes in this region of the Arctic may influence the distribution of ice over the entire basin. If the Beaufort Sea anticyclone weakens, so does the Beaufort Gyre. Ice advection along the Transpolar Drift Stream is then enhanced [*Drobot and Maslanik*, 2003] and ice is exported out of the basin through the Fram Strait (east of Greenland). Also, during early spring the ice may be preconditioned thermodynamically leading to an early melt that apparently prolongs the melt season as a consequence of a positive temperature-albedo feedback. This can thin the ice pack and result is a net loss over time if the cycle repeats itself in subsequent years. This feedback, and the dynamical and thermodynamical processes that underlie it, will be the focus of future investigations. The Study for Environmental Arctic Change (SEARCH) Program under the NOAA Arctic Research Office is taking the lead in this and related investigations of the Arctic climate system.

Acknowledgments. The RAOS project was supported by the U.S. Department of Energy Atmospheric Radiation Measurement (ARM) Program and the NOAA Aerosol-Climate Interactions Program. We also gratefully acknowledge the hard work and scientific input of the other RAOS participants.

3.2.7. REFERENCES

Anderson, G.P., A. Berk, P.K. Acharya, M.W. Matthew, L.S. Bernstein, J.H. Chetwynd, H. Dothe, S.M. Adler-Golden, A.J. Ratkowski, G.W. Felde, J.A. Gardner, M.L. Hoke, S.C. Richtsmeier, B. Pukall, J. Mello and L.S. Jeong (2000), MODTRAN4: Radiative transfer modeling for remote sensing in algorithms for multispectral, hyperspectral, and ultraspectral imagery VI, edited by S. Chen and M. R. Descour, *Proceedings of SPIE 4049-16*, pp. 176-183, Int. Soc. Opt. Eng., Orlando, FL, 24 April 2000, .

Barrie, L.A. (1996), Occurrence and trends of pollution in the Arctic troposphere, in *Chemical Exchange Between the Atmosphere and Snow*, edited by E.W. Wolff and R.C. Bales, *NATO ASI Series I, 43,* pp. 93-129, Springer-Verlag, Berlin.

Barrie L.A., R.M. Hoff, and S.M Daggupaty (1981), The influence of midlatitudinal pollution sources on haze in the Canadian Arctic, *Atmos. Environ.*, *15*, 1407-1419.

Belchansky, G.I., D.C. Douglas, and N.G. Platonov (2004), Duration of the Arctic sea ice melt season: Regional and interannual variability, 1979-2001, *J. Clim*., *17*, 67-80.

Bergin, M.H., E. Meyerson, J.E. Dibb, and P. Mayewski (1998), Comparison of continuous aerosol measurements and ice core chemistry over a 10-year period at the South Pole, *Geophys. Res. Lett., 25*, 1189-1192.

Bergin, M.H., R.S. Halthorne, S.E. Schwartz, J.A. Ogren, and S. Nemesure (2000), Comparison of aerosol column properties based on nephelometer and radiometer measurements at the SGP ARM site, *J. Geophys. Res., 105*, 6807-6818.

Bird, R.E., and C. Riordan (1986), Simple solar spectral model for direct and diffuse irradiance on horizontal and tilted planes at the Earth's surface for cloudless atmospheres, *J. Appl. Meteorol., 25*(1), 87-97.

Blanchet, J.P. (1989), Toward an estimation of climatic effects due to Arctic aersosols, *Atmos*. *Env*., *23*, 2609-2625.

Bodhaine, B.A. (1989), Barrow surface aerosol: 1976-1987, *Atmos. Environ., 23*(11), 2357-2369.

Bodhaine, B.A. (1995), Aerosol absorption measurements at Barrow, Mauna Loa and South Pole, *J. Geophys. Res., 100*, 8967-8975.

Bodhaine, B.A., and J.J. DeLuisi (1985), An aerosol climatology of Samoa, *J. Atmos. Chem., 3*, 107-122.

Bodhaine, B.A., and E.G. Dutton (1993), A long-term decrease in Arctic Haze at Barrow, Alaska, *Geophys. Res. Lett., 20*, 947-950.

Bodhaine, B.A., B.G. Mendonca, J.M. Harris, and J.M. Miller (1981), Seasonal variation in aerosols and atmospheric transmission at Mauna Loa Observatory, *J. Geophys. Res., 88,* 6769-6772.

Bodhaine, B.A., J.J. DeLuisi, J.M. Harris, P. Houmere, and S. Bauman (1986), Aerosol measurements at the South Pole, *Tellus, 38B*, 223-235.

Bodhaine, B.A., J.J. De Luisi, J. M. Harris, P. Houmere, and S. Bauman (1987), PIXE analysis of South Pole aerosol*,* in *Nuclear Instruments and Methods in Physics Research*, *B22*, 241-247, Elsevier, Amsterdam.

Bodhaine, B.A., J.M. Harris, and J.A. Ogren (1992), Aerosol optical properties at Mauna Loa Observatory: Long-range transport from Kuwait?, *Geophys. Res. Lett., 19*, 581-584.

Bory, A.J.M., P.E. Biscaye, and F.E. Grousset (2003), Two distinct seasonal Asian source regions for mineral dust deposited in Greenland (NorthGRIP), *Geophys*. *Res*. *Lett*., *30*(4), 1167.

Brandt, R.E., and S.G. Warren (1996), Effect of sastrugi on the bidirectional reflectance of snow, in *IRS '96*: *Current Problems in Atmospheric Radiation*, *Procceedings of the International Radiation Symposium*, Fairbanks, AK, 19-24 August 1996, Deepak, p. 45.

Cacciari, A., A. Lupi, C. Tomasi, V. Viatale, and S. Marani (2000), Calculation of the radiative forcing caused by aerosol particles in Antarctic regions (Terra Nova Bay), *Procceedings of 8th Workshop Italian Research on Antarctic Atmosphere,* Bologna, Italy, Oct. 20-22, 1999, edited by M. Colacino and G. Giovanelli, pp. 455-467, Ital. Phys. Soc., Bologna, Italy.

Carrico, C.M., M.J. Rood, and J.A. Ogren (1998), Aerosol light scattering properties at Cape Grim, Tasmania, during the First Aerosol Characterization Experiment (ACE 1), *J. Geophys. Res*., *103*(D13), 16,565-16,574, doi:10.1029/98JD00685.

Charlson, R.J., S.E. Schwartz, J.M. Hales, R.D. Cess, J.A. Coakley, Jr., J.E. Hansen, and D.J. Hofmann (1992), Climate forcing by anthropogenic aerosols, *Science, 255*, 423-430.

Curry, J.A., J.L. Schramm, and E.E. Ebert (1995), Sea ice-albedo climate feedback mechanism, *J. Clim., 8*, 240-247.

Delene, D.J., and J.A. Ogren (2002), Variability of aerosol optical properties at four North American surface monitoring sites, *J. Atmos. Sci.*, *59*, 1135-1150.

Della Monache, L., K.D. Perry, R. Cederwall, and J.A. Ogren (2004), In situ aerosol profiles over the Southern Great Plains CART site, Part II: Effects of mixing height on aerosol properties, in revision, *J. Geophys. Res*.

Drobot, S.D., and J.A. Maslanik (2003), Interannual variability in summer Beaufort sea ice conditions: Relationship to spring and summer surface and atmospheric variability. *J.Geophys. Res.*, *108*(C7), 3233, doi:10.1029/2002JC001537.

Drobot, S.D., and M.R. Anderson (2001), An improved method for determining snowmelt onset dates over Arctic sea ice using scanning multichannel microwave radiometer and Special Sensor Microwave/ Imager data, *J. Geophys. Res*. *106*(D20), 24,033-24,049.

Dutton, E.G., and B.A. Bodhaine (2001), Solar irradiance anomalies caused by clear-sky transmission variations above Mauna Loa: 1958-99, *J. Clim., 14,* 3255-3262.

Dutton, E.G., and D.J. Endres (1991), Date of snow melt at Barrow, Alaska, USA, *Arctic Alpine Res., 23*, 115-119, 1991.

Dutton, E.G., J.J. DeLuisi, and B. Bodhaine (1984), Features of aerosol optical depth observed at Barrow, March 10-20, 1983, *Geophys, Res. Lett., 11*(5), 385-388.

Dutton, E.G., J.J. DeLuisi, and A.P. Austring (1985), Interpretation of Mauna Loa atmospheric transmission relative to aerosols, using photometric precipitable water amounts, *J. Atmos. Chem., 3*, 53-68.

Dutton, E.G., J.J. DeLuisi, and G.A. Herbert (1989), Shortwave aerosol optical depth of Arctic haze measured on board the NOAA WP-3D during AGASP-II, April 1986, *J. Atmos. Chem., 9*, 71-79.

Dutton, E.G., R.S. Stone, and J.J. DeLuisi (1989), South Pole radiation balance measurements April 1986 to February 1988, *NOAA Data Report ERL ARL-17*, 49 pp., National Oceanic and Atmos. Admin., Boulder, CO.

Dutton, E.G., J.J. Michalsky, T. Stoffel, B.W. Forgan, J. Hickey, D.W. Nelson, T.L. Alberta, and I. Reda (2001), Measurement of broadband diffuse solar irradiance using current commercial instrumentation with a correction for thermal offset errors, *J. Atmos. Oceanic Technol., 18,* 297-314.

Dutton, E.G., A. Farhadi, R.S. Stone, C. Long, and D.W. Nelson (2004), Long-term variations in the occurrence and effective solar transmission of clouds determined from surface irradiance observations. *J. Geopyhs. Res*, in press.

Ellis, H.T., and R.F. Pueschel (1971), Solar radiation: Absence of air pollution trends at Mauna Loa, *Science, 172,* 845-846.

Ferrare, R.A., D.D. Turner, T.P. Tooman, L.A. Heilman, O. Dubovik, W.F. Feltz, and R.N. Halthore (2000), Characterization of the atmospheric state above SGP using Raman lidar and AERI/GOES measurements, *Procceedings of the Tenth ARM Science Team Meeting*, San Antonio, TX, 13-17 March 2000.

Griffin, D.W., C.A. Kellogg, V.H. Garrison, and E.A. Shinn (2002), The global transport of dust, *Am. Sci. 90*, 228-235.

Hare, S.R,. and N.J. Mantua (2000), Empirical evidence for North Pacific regime shifts in 1977 and 1989, *Prog. Oceanogr.*, *47*, 103-145.

Harris, J.M., and J. D. W. Kahl (1994), Analysis of 10-day isentropic flow patterns for Barrow, Alaska: 1985-1992. *J. Geophys. Res.*, *99*, 25,845-25,855.

Hegg, D.A., P.V. Hobbs, S. Gasso, J.D. Nance, and A.L. Rangno (1996), Aerosol measurements in the Arctic relevant to direct and indirect radiative forcing, *J. Geophys. Res., 101*(D18), 23,349-23,363.

Holben, B.N., D. Tanré, A. Smirnov, T.F. Eck, I. Slutsker, N. Abuhassan, W.W. Newcomb, J.S. Schafer, B. Chatenet, F. Lavenu, Y.J. Kaufman, J.V. Castle, A. Setzer, B. Markham, D. Clark, R. Frouin, R. Halthore, A. Karneli, N.T. O'Neill, C. Pietras, R.T. Pinker, K. Voss, and G. Zibordi (2001), An emerging ground-based aerosol climatology: Aerosol optical depth from AERONET, *J. Geophys. Res.*, *106*(D11), 12,067-12,097, doi:10.1029/2001JD900014.

IPCC 2001: *Climate Change 2001: The Scientific Basis. Contribution of Working Group I to the Third Assessment Report of the Intergovermental Panel on Climate Change*, edited by J. T. Houghton, et al., Cambridge Univ. Press, New York.

Key, J., J. Collins, C. Fowler, and R. Stone (1997a), High-latitude surface temperature estimates from thermal satellite data, *Remote Sensing Environ*., *1*, 302-309.

Key, J.R., A.J. Schweiger, and R.S. Stone (1997b), Expected uncertainty in satellite-derived estimates of surface radiation budget at high latitudes*, J. Geophys. Res., 102*, 15,837-15,847.

King, D.B. (2002), *Climate Monitoring and Diagnostics Laboratory CMDL No. 26 Summary Report 2000,* edited by R.C. Schnell, R.M. Rosson, and C. Sweet (Eds.), 184 pp., National Oceanic and Atmos. Admin., Boulder, CO.

King, M.D., D.M. Byrne, B.M. Herman, and J.A. Reagan (1978), Aerosol size distributions obtained by inversion of spectral optical depth measurements, *J. Atmos. Sci., 35,* 2153-2167.

Maslanik, J., M. Serreze, and T. Agnew (1999), On the record reduction in 1998 Western Arctic sea-ice cover, *Geophys. Res. Lett.*, *26*(13), 1905–1908.

Maslanik, J.A., R. Stone, J. Pinto, J. Wendell, and C. Fowler (1999), Mobile-platform observations of surface energy budget parameters at the SHEBA site, *Procceedings of 5th Conf. on Polar Met. and Oceanogr.*, Dallas, TX, 10-15 January 1999, pp. 128-131, Am. Met. Soc., Boston.

Marty, C., R. Philipona, J. Delamere, E. G. Dutton, J. Michalsky, K. Stamnes, R. Storvold, T. Stoffel, S.A. Clough, and E.J. Mlawer (2003), Longwave irradiance uncertainty under Arctic atmospheres: Comparisons between measured and modeled downward longwave fluxes, *J. Geophys. Res., 108* (D12), 4358, doi:10.1029/2002JD002937.

McInnes, L.M., M.H. Bergin, J.A. Ogren, and S.E. Schwartz (1998), Differences in hygroscopic growth between marine and anthropogenic aerosols, *Geophys. Res. Lett., 25*, 513-516.

Michalsky, J., E.G. Dutton, M. Rubes, D. Nelson, T. Stoffel, M. Wesley, M. Splitt, and J. Deluisi (1999), Optimal measurement of surface shortwave irradiance using current instrumentation, *J. Atmos. Oceanic Technol., 16,* 55-69.

Michalsky, J.J., R. Dolce, E.G. Dutton, M. Haeffelin, G. Major, J.A. Schlemmer, D.W. Slater, J.R. Hickey, W.Q. Jeffries, A. Los, D. Mathias, L.J.B. McArthur, R. Philipona, I. Reda, and T. Stoffel (2003), Results from the first ARM diffuse horizontal shortwave irradiance comparison, *J. Geophys. Res. 108*(D3), 4108, doi:10.1029/ 2002JD002825.

NRC (National Research Council) (1996), *Aerosol Radiative Forcing and Climatic Change*, 161 pp., National Academy Press, Washington, D.C.

Ogren, J.A. (1995), A systematic approach to in situ observations of aerosol properties, in *Aerosol Forcing of Climate*, edited by R.J. Charlson and J. Heintzenberg, pp. 215-226, John Wiley, New York.

Ogren, J.A., J. Heintzenberg, and R. J. Charlson (1985), In situ sampling of clouds with a droplet to aerosol converter, *Geophys. Res. Lett., 12*, 121-124.

Ohmura, A., H. Gilgen, H. Hegner, G. Müller, M. Wild, E.G. Dutton, B. Forgan, C. Fröhlich, R. Philipona, A. Heimo, G. Konig-Langlo, B. McArthur, R. Pinker, C.H. Whitlock, and K. Dehne (1998), Baseline Surface Radiation Network (BSRN)/WCRP: New precision radiometry for climate research, *Bull. Am. Meteorol. Soc., 79*(10), 2115- 2136.

Parkinson, C.L., D.J. Cavalieri,, H.J. Zwally, and J.C. Comiso (1999), Arctic sea ice extents, areas, and trends, 1978-1996, *J. Geophys. Res*., *104*(C9), 20,837-20,856, doi:10.1029/1999JC900082.

Philipona, R., C. Fröhlich, K. Dehne, J. DeLuisi, J. Augustine, E. Dutton, D. Nelson, B. Forgan, P. Novotny, J. Hickey, S.P. Love, S. Bender, B. McArthur, A. Ohmura, J.H. Seymour, J.S. Foot, M. Shiobara, F.P.J. Valero, and A.W. Strawa (1998), The BSRN pyrgeometer round-robin calibration experiment, *J. Atmos. Oceanic Technol., 15,* 687-696.

Philipona, R.C., E.G. Dutton, T. Stoffel, J. Michalsky, I. Reda, A. Stifter, P. Wendling, N. Wood, S.A. Clough, E.J. Mlawer, G. Anderson, H.E. Revercomb, and T.R. Shippert (2001), Atmospheric longwave irradiance uncertainty: Pyrgeometers compared to an absolute sky-scanning radiometer, AERI, and radiative transfer model calculations,

J. Geophys. Res., 106(D22), 28,129-28,142, doi: 10.1029/2000JD000196.

Pinto, J.O., J.A. Curry, J.A. Maslanik, C.W. Fairall, and R.S. Stone (1999), Horizontal variability in surface radiative fluxes surrounding SHEBA from airborne and ground-based sensors (11.1), *Procceedings of the 5th Conference on Polar Meteorology and Oceanography*, Am. Meteorol. Soc., Dallas, TX, January 1999.

Pinto, James O., A. Alam, J.A. Maslanik, J.A. Curry, and R.S. Stone (2003), Surface characteristics and atmospheric footprint of springtime Arctic leads at SHEBA, *J. Geophys. Res., 108*(C4), doi:10.1029/2000JC000473.

Quakenbush, T.K., and B.A. Bodhaine (1986), Surface aerosols at the Barrow GMCC observatory: Data from 1976 through 1985, *NOAA Data Rep. ERL-ARL-10*, 230 pp., NOAA Air Resources Lab., Silver Spring, MD.

Quinn, P.K., T.L. Miller, T.S. Bates, J.A. Ogren, E. Andrews, and G.E. Shaw (2002), A 3-year record of simultaneously measured aerosol chemical and optical properties at Barrow, Alaska, *J. Geophys. Res.*, *107*, doi:10.1029/2001JD001248.

Rothrock, D.A., Y. Yu, and G.A. Maykut (1999), Thinning of Arctic sea-ice cover, *Geophys. Res. Lett.*, *26*, 3469-3472.

Serreze, M.C., J.E. Walsh, F.S. Chapin III, T. Osterkamp, M. Dyurgerov, V. Romanovsky, W.C. Oechel, J. Morison, T. Zhang, and R.G. Barry (2000), Observational evidence of recent change in the northern high-lattitude environment, *Clim. Change*, *46*, 159-207.

Shaw, G.E. (1983), Evidence for a central Eurasian source area of Arctic haze in Alaska, *Nature*, *299*, 815-818.

Sheridan, P.J., D.J. Delene, and J.A. Ogren (2001), Four years of continuous surface aerosol measurements from the DOE/ARM Southern Great Plains CART site, *J. Geophys. Res*., *106*, 20,735-20,747.

Sokilik, I., A. Andronova, and T.C. Johnson (1993), Complex refractive index of atmospheric dust aerosols, *Atmos. Environ*., *27A*(16), 2495-2502.

Stamnes, K., J. Slusser, and M. Bowen (1991), Derivation of total ozone abundance and cloud effects from spectral irradiance measurements, *Appl. Opt*., *30*(30).

Stone, R.S. (1993), Properties of austral winter clouds derived from radiometric profiles at South Pole, *J. Geophys. Res*., *98*(D7), 12,961-12,971.

Stone, R.S. (1997), Variations in Western Arctic temperatures in response to cloud radiative and synoptic-scale influences, *J. Geophys. Res*., *102*, 21,769-21,776.

Stone, R.S. (2002) Monitoring aerosol optical depth at Barrow, Alaska and South Pole; Historical overview, recent results, and future goals, *Procceedings of the 9th Workshop Italian Research on Antarctic Atmosphere*, Rome, Italy, 22-24 October 2001, edited by M. Colacino, pp. 123-144, Ital. Phys. Soc., Bologna, Italy.

Stone, R.S., and J.D. Kahl (1991), Variations in boundary layer properties associated with clouds and transient weather disturbances at the South Pole during winter, *J. Geophys. Res.*, *87*(D3), 5137-5144.

Stone, R.S., J. Key, and E. Dutton (1993), Properties and decay of stratospheric aerosols in the Arctic following the 1991 eruptions of Mount Pinatubo, *Geophys. Res. Lett.*, *20*(21), 2359-2362.

Stone, R.S., E.G. Dutton, J.M. Harris, and D. Longenecker (2002), Earlier spring snowmelt in northern Alaska as an indicator of climate change, *J. Geophys. Res*., *107*(D10), doi:10.1029/2000JD000286.

Thompson, D.W.J., and J.M. Wallace (1998), The Arctic oscillation signature in the wintertime geopotential height and temperature fields, *Geophys. Res. Lett*., *25*(9), 1297-1300.

Uttal, T., J.A. Curry, M.G. McPhee, D.K. Perovich, R.E. Moritz, J.A. Maslanik, P.S. Guest, H.L. Stern, J.A. Moore, R. Turenne, A. Heiberg, M.C. Serreze, D.P. Wylie, O.G. Persson, C.A. Paulson, C. Halle, J.H. Morison, P.A. Wheeler, A. Makshtas, H. Welch, M.D. Shupe, J.M. Intrieri, K. Stamnes, R.W. Lindsey, R. Pinkel, W.S. Pegau, T.P. Stanton, and T.C. Grenfeld (2002), Surface heat budget of the Arctic Ocean, *Bull. Amer. Meteor. Soc*., *83*, 255-276.

VanCuren, R., and T. Cahill (2002), Asian aerosols in North America: Frequency and concentration of fine dust, *J. Geophys. Res*., *107*(D24), 4804, doi:10.1029/2002JD002204.

Waple, A.M., and J.H. Lawrimore (Eds.) (2003), State of the climate in 2002, *Bull. Am. Meteorol. Soc.*, *84*(6), S1-S68.

Waple, A.M., J.H. Lawrimore, M.S. Halpert, G.D. Bell, W. Higgins, B. Lyon, M.J. Menne, K.L. Gleason, R.C. Schnell, J.R. Christy, W. Thiaw, W.J. Wright, M.J. Salinger, L. Alexander, R.S. Stone, and S.J. Camargo (2002), Climate assessment for 2001, *Bull. Am. Meteorol. Soc.*, *83*(6), S1-S62.

Warren, S.G., R.E. Brandt, and P.O. Hinton (1998) Effect of surface roughness on bidirectional reflectance of Antarctic snow, *J. Geophys. Res.*, *103*, 25,789-25,807.